Design and Implementation of High-Performance, Compact Frequency Diplexers for High Data Rate Wireless mm-W Communication Links

by Wenyao Zhai B.Eng

A thesis
presented to the Department of Electronics
in fulfillment of the
thesis requirement for the degree of
Masters of Applied Science in Electrical Engineering

Ottawa-Carleton Institute for Electrical Engineering
Department of Electronics
Carleton University
Ottawa, Ontario

Canada

The undersigned recommend to
the Faculty of Graduate and Postdoctoral Affairs
acceptance of the thesis

Design and Implementation of High-Performance, Compact Frequency Diplexers for High Data Rate Wireless mm-W Communication Links

Submitted by

Wenyao Zhai, B.Eng.

In partial fulfillment of the requirements for the degree of

Master's of Applied Science

in Electrical and Computer Engineering

Professor Langis Roy, Co-Supervisor

Professor Barry Syrett, Co-Supervisor

Professor Calvin Plett
Chair, Department of Electronics

Ottawa-Carleton Institute for Electrical and Computer Engineering
Carleton University
Department of Electronics
2011

Abstract

Diplexer and band pass filter (BPF) designs based on print-circuit components and three-dimensional low temperature co-fired ceramic (LTCC) substrate integrated waveguide (SIW) are presented. The diplexer specifications are proposed for a multi-gigabit per second (Gb/s) full duplex point-to-point V-band (56 – 64 GHz) radio having BER of 1×10^{-6}. Firstly, a BPF based on printed-circuit open-loop resonators is designed for local oscillator spurious rejections at Ku-band. However, due to low Q, its performances cannot be extended to V-band. An alternative LTCC-SIW BPF with unloaded Q of 677 and loaded Q of 64 is designed for V-band. A five-pole SIW BPF has a 1.4 % fractional bandwidth, return loss ≥ 20 dB, insertion loss ≤ 2.5 dB and ≥ 40 dB rejection at 2 GHz offset from the passband frequency.

Broadband and low loss microstrip to WR15 waveguide launcher designs are also designed with both planar-circuit and LTCC substrates. Together with the designed BPFs, a compact diplexer is designed to satisfy the specifications of the proposed radio system.

Acknowledgements

诚实 上进 知书达理

父母于我一生之奋斗目标

Table of Contents

List of Figures

List of Abbreviations and Symbols

BPF	Bandpass Filter
FBW	Fractional Passband Width
SIW	Substrate Integrated Waveguide
RF	Radio Frequency
LTCC	Low Temperature Co-fired Ceramic
COM	Common Port
HD	High Definition
Gb/s	Gigabit-per-second
CS	Channel Spacing
FDD	Full-duplex
TX	Transmit
RX	Receive
Q	Quality Factor
IL	Insertion Loss
SNR	Signal to Noise Ratio
BER	Bit Error Rate
ETSI	European Telecommunication Standards Institute
PN	Phase Noise
Ms/s	Mega-symbol per second

QAM	Quadrature Amplitude Modulation
EVM	Error Vector Magnitude
PA	Power Amplifier
NF	Noise Figure
IF	Intermediate Frequency
P1dB	1 dB compression point
PAPR	Peak-to-average Power Radio
ISI	Inter-symbol Interference
VCO	Voltage Controlled Oscillator
PLL	Phase Lock Loop
RRC	Root Raise Cosine
IRR	Image Rejection Ratio
LNA	Low Noise Amplifier
IP2	2nd order compression point
CL	Conversion loss
VSWR	Voltage standing wave ratio
RL	Return loss
A	Stopband attenuation
A_m	Passband ripple
BW	Bandwidth

Z_0 Characteristic impedance

K   Propagation constant

$\tan \delta$ Loss tangent

MCM   Multi-chips module

Chapter 1   Introduction

1.1   Overview

In response to increasing consumer demand for very data intensive mobile applications such as video streaming, internet surfing, video conference calls and the distribution of high definition (HD) video signals wirelessly in the home, more spectrum bandwidth must be made available to wireless users. Metropolitan area networks provide broadband services and use fiber-optic links because of the multi-gigabit-per-second (Gb/s) data rate they offer. Meanwhile, a wireless link is very attractive for densely populated areas or in an area whose terrain limitations render fiber-optic links difficult to implement. One popular solution for bringing broadband service over the "last mile" is to install a wireless link to the home between the fiber-optic backbones.

In order to optimize bandwidth usage, the "last mile" wireless links operate at high microwave and millimeter wave frequencies, i.e. at commercial Ku band (12–18 GHz) and Ka band (26.5–40 GHz), free licensed V band (56–64 GHz) and lightly licensed experimental E band (71–76 GHz, 81–86 GHz and 92–95 GHz). Transceiver design at these frequencies is challenging, especially for the realization of the frequency selection components whose specifications are usually critical. In general, they must reject spurious frequencies by more than 45 dB [1] [2]. Very often, to make valuable spectrum more efficient, channels are narrow-band and channel spacing (CS) is small compared to the channel frequencies. This means the frequency selection components have to have an extremely small fractional bandwidth (FBW). At the same time they must provide approximate 45 dB rejection of the emissions from very close neighboring channels [1] [2]. Also, a full-duplex (FDD) radio requires the frequency selection component to isolate the transmitter (TX) signal from receiver (RX) signal, making sure the power leakage from the TX does not saturate the sensitive RX.

Frequency selection components use several inter-coupled high-Q resonators to achieve the filter function. They suffer a finite amount of insertion loss which is

proportional to frequency selectivity and the slope of rejection in the stopband. In order to achieve small FBW, coupling between resonators is weak, and to have a better rejection slope, higher-order filtering (i.e., more resonators) is required. In both cases insertion loss will increase. As well, material losses (both substrate and conductor) are directly proportional to frequency.

In this thesis, microstrip transmission lines are used in most designs. The physical size of a microstrip circuit is inversely proportional to both the frequency and the dielectric constant, since the microstrip wavelength is given by

$$\lambda_g = \frac{c}{\sqrt{\varepsilon_{eff}} \cdot f}$$

(1.1)

where ε_{eff} is the effective dielectric constant, f is the frequency and c is the speed of light in free space. High frequency operation leads to small circuit dimensions that are difficult to etch. They are also vulnerable to fabrication tolerances and changes in ambient temperature.

Considering all aforementioned design difficulties, waveguide seems to be a better candidate for filter design because waveguide has the least loss and the highest unloaded quality factor. However, waveguides are bulky, difficult to integrate with other parts of the RF circuit and expensive to machine. Further, waveguide BPFs need to be tuned manually to obtain an accurate response, and they are vulnerable to different thermal conditions.

1.2 Motivations and Objectives

An FDD communication link allows two parties to communicate with one another in both directions simultaneously. This is obviously more desirable for commercial telecommunication applications compared to half-duplex links. Instead of using a switch

for TX or RX control in half-duplex operation, a diplexer is required for FDD operation. A diplexer is a three port device, in which the high and low frequency ports each consist of a BPF to select the TX frequency and RX frequency, respectively. The third port is the output of the two BPFs joined as the common (COM) port and is connected to the antenna.

Traditionally, diplexers at millimeter-wave frequencies are realized with waveguides, because of their sharp rejection at stop-band and low insertion loss at passband. However, waveguides are difficult and expensive to build and tune. It is very attractive to develop other inexpensive, more repeatable, and simply constructed diplexers that don't require tuning and that don't lead to significant degradation in performance. The overall goal of this work is to develop alternative mm-wave diplexer realizations for high data rate point-to-point wireless links that exhibit compactness and ease of integration with the rest of the circuitry at the transceiver I/O port. Specifically, the following thesis objectives will be pursued:

1. Detailed system design of a proposed V-band multi-Gb/s point-to-point wireless link. System performance and trade-off is discussed in order to determine the diplexer specification.

2. Design of BPFs using coupled open-loop resonators printed on Duroid or alumina substrate for both TX and RX ports, together with a microstrip to waveguide transition launcher for connection to the antenna.

3. Design of BPFs using substrate integrated waveguide (SIW) resonators with a novel loading design in a low-temperature co-fired ceramic (LTCC) process for both TX and RX ports. The COM port is a microstrip to waveguide transition designed LTCC.

1.3   Thesis Organization

Chapter 2 begins with a hypothetical wireless communication link system design. The outcome of the design is the determination of the BPF specifications for both TX and RX ports. Section 2.1 also discusses the importance of the frequency selection component and how its performance affects the overall system performance. Sensitivity studies are made based on the system's specifications to determine how system specifications are traded off to loosen the BPF specifications. Section 2.2 covers basic filter theory and different types of filters together with their advantages and disadvantages. Filter realization techniques are also presented. In Section 2.3 different types of millimeter-wave substrate technologies are discussed, followed by resonator structures and designs. Lastly input and output coupling techniques as well as internal coupling techniques between resonators are discussed.

In Chapter 3 the design of planar printed BPFs is presented, and Chapter 4 follows a similar outline for the design of SIW BPF in LTCC technology. In each chapter, resonator structures are designed first at centre the frequency. Simulations are performed using Ansoft HFSS CAD tool. Different feeding methods with respective loaded Qs are simulated. Coupling mechanisms are presented followed by final tuning procedures.

In Chapter 5, a microstrip line to waveguide transition launcher in each technology is designed, tuned and optimized. Each launcher is used at the common port as the output of the TX BPF to antenna and the input of RX BPF from antenna.

In Chapter 6, conclusions are given as well as recommendations for future work.

Chapter 2   System Study and Filter Concepts

In accordance with the first thesis objective, this chapter presents a hypothetical, yet commercially relevant, V-band (56 – 59 GHz) wireless communication link system design. The results of this design will lead to the specification of the band-pass filters pursued in subsequent chapters. In addition, basic resonator and filter design concepts will be reviewed.

2.1   System Design and Diplexer Specifications

Filters and diplexers are critical components in a wireless communication link because they can limit the overall system performance. For any FDD radio architectures, the diplexer is the most significant filtering component since it is the first RF component after the antenna at both the input and output of a transceiver. Its insertion loss (IL) will degrade the signal to noise ratio (SNR) of the receiver and its filter response will determine the spurious signal leaking between the TX and RX signal paths. The following sections the detailed design of a hypothetical FDD V-band wireless link will allow typical specifications to be set for the transceiver's diplexer.

2.1.1 Target radio performance and regulation

Table 1 summarizes the target system specifications of a radio transceiver intended for the unlicensed V-band spectrum.

Table 1: Target radio system specifications

Data Rate	≥ 1 Gb/s
Mode of operation	FDD
Bit error rate (BER)	$\leq 1 \times 10^{-6}$
System SNR	≥ 26 dB
Minimum and maximum range of transmission	100 / 800 metres
Frequency of operation	unlicensed V band (56 – 59GHz)

This full duplex radio is designed for point to point communication purposes. In order to meet increasingly high data flows demanded by end users, the targeted data rate is set to at least 1Gb/s with BER of $\leq 1 \times 10^{-6}$. The line of sight range of the link is between 100 and 800 metres, since the radio is intended to be the last link from the optical network backbone to the home. The short transmission range could actually have some advantages, i.e. the communication is more secure and the frequency spectrum use is more efficient. Another reason for such short range is due to the high atmospheric attenuation in V band as shown in Figure 2.1. It peaks at 20dB/km at 60GHz. This is actually why this band is unlicensed in most parts of the world. Figure 2.3 shows the available spectrum in the V-band in several countries and continents. Lastly, the maximum TX power is set by spectrum regulations and this limits the maximum range of the radio. In this design, the European Telecommunication Standards Institute (ETSI) standard is followed. Table 2 summarizes the ETSI regulations; maximum TX power is set at 10dBm.
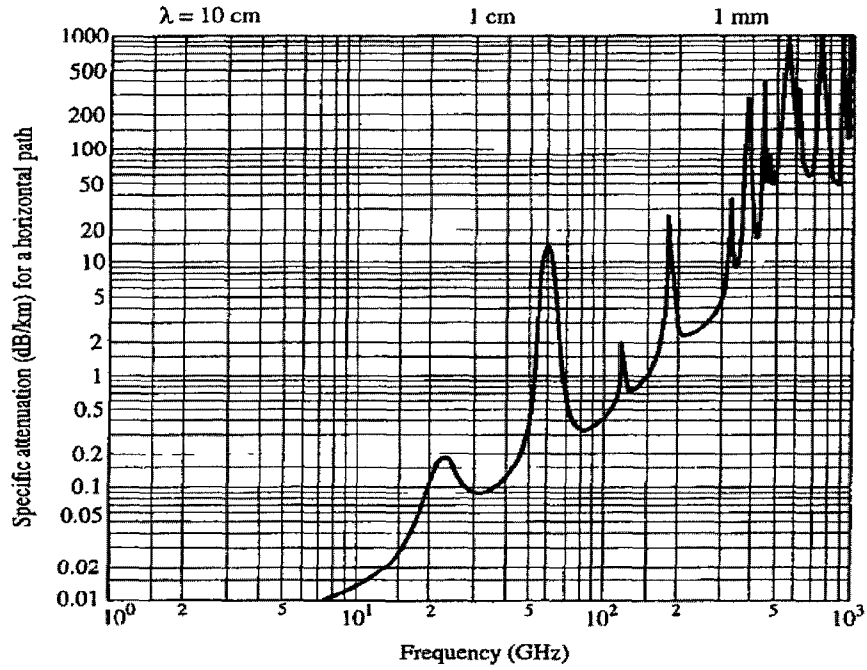
Figure 2-1 Specific attenuation due to gaseous constituents for transmissions through a

standard atmosphere $(20^\circ C$, 1 atm, water vapour content $= 7.5 \left[\frac{g}{m^3} \right]$) [24][25]

The lower edge of the V-band spectrum in this design is used because of relatively lower loss and lower phase noise (PN) there. PN will increase according to the multiplication factor for the reference frequency. It is also easy to place the local oscillator (LO) tone out of band, and only one LO line-up is needed since the tuning range is reasonable.

Worldwide Unlicensed V Band
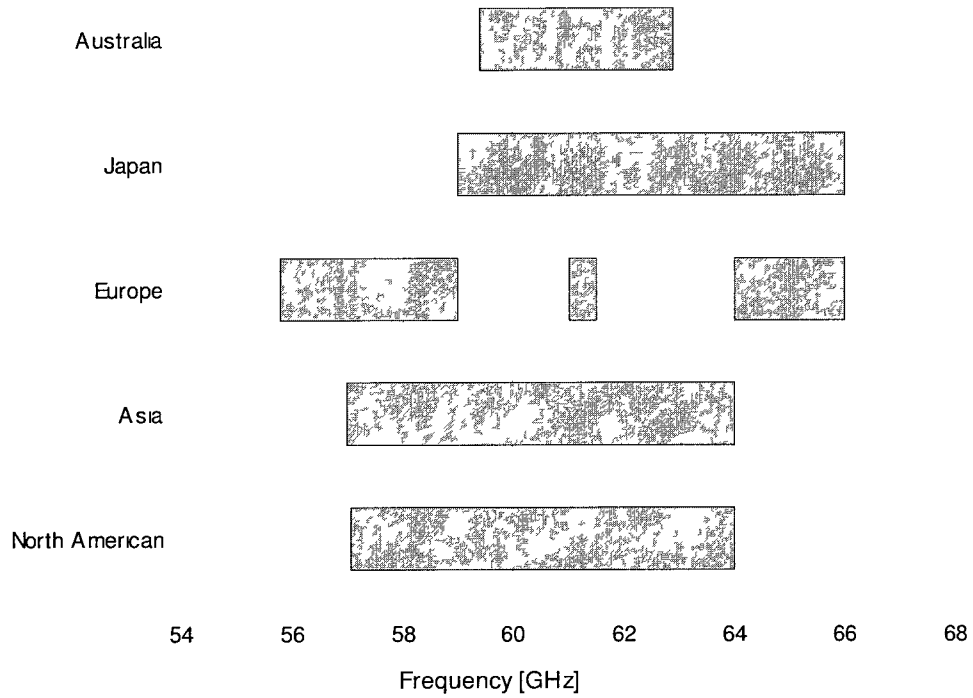
Figure 2-2 World-wide unlicensed spectrum around V band [1] [3] [4]

The following table summarizes the ETSI regulations for point to point digital radio operating at unlicensed V band.

Table 2: The European ETSI regulations [3] [4]

Frequency range	56 – 66 GHz
Maximum peak EIPR	55 dBm
Maximum transmitter power	10 dBm
Maximum out of band spurious EIRP	-10 dBm
Maximum in-band spurious at adjacent channel	-30 dBm

8

2.1.2 Frequency plans

The goal of the frequency plan is to achieve the target multi-Gb/s data rate within the 56-59 GHz spectrum of operation. Only 2 GHz spectrum is actually used for data with a 1 GHz guard band between the TX and RX channels. The TX and RX bands are each 900 MHz wide divided equally into 4 channels 225 MHz wide. The remaining 200MHz is used to provide a 100MHz guard band below the TX channels and above the RX channels. Figure 2.3 shows the detailed frequency plan of the proposed radio.
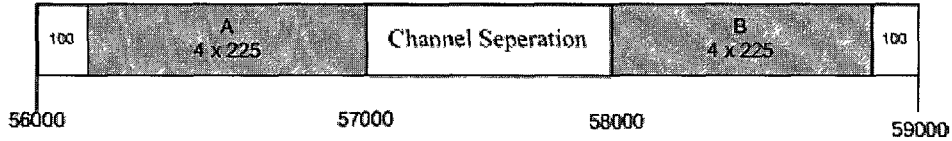
Figure 2-3 FDD frequency planning, A is TX spectrum, B is RX spectrum, in MHz.

The 1GHz channel separation (CS) is not a waste of spectrum as it can be used for a different radio band. The value of CS is an important factor for the diplexer specification, since the amount of TX output power leakage into the RX input has to be below the sensitivity of the receiver. In this plan the RX frequency band has four channels, from 58 GHz to 58.9 GHz.

2.1.3 Data rate and modulation

The radio design uses a symbol rate of 225 Mega-symbol per second (Ms/s) equal to the channel bandwidth 225 MHz. Without any coding redundancy, in order to achieve greater than 1 Gb/s, 6 bits per symbol must be used, as given by the following formula [24]

$$\text{bit rate} = symbol\ rate \times N \times code\ rate$$
$$1.35\,Gb/s = 225\,Ms/s \times 6 \times 1$$
(2.1)

9

where N is number of bits per symbol, and *code rate* is the ratio of redundancy of coded date. For the cases where multi-path and/or tough weather conditions may degrade the performance, coding can be introduced to achieve the target BER. Without any coding, the code rate equals 1.

Since N is determined to be 6, a 64 symbol quadrature amplitude modulation (QAM) is used. The choice of the modulation is also important to diplexer design since it sets the system's SNR requirement. In addition, it also sets the amount of back-off from saturation for the peak output power out of the transmitter. These have direct effects on the insertion loss specification of the diplexer.

2.1.4 SNR and error vector magnitude (EVM)

SNR is a key design parameter for any radio system design especially for the receiver. Since the probability of BER is directly related to modulation format and bit energy to noise ratio (E_b/N_o) as shown in the following "waterfall" curve plot for 64 QAM created using *BER* function from © Matlab signal processing toolset.
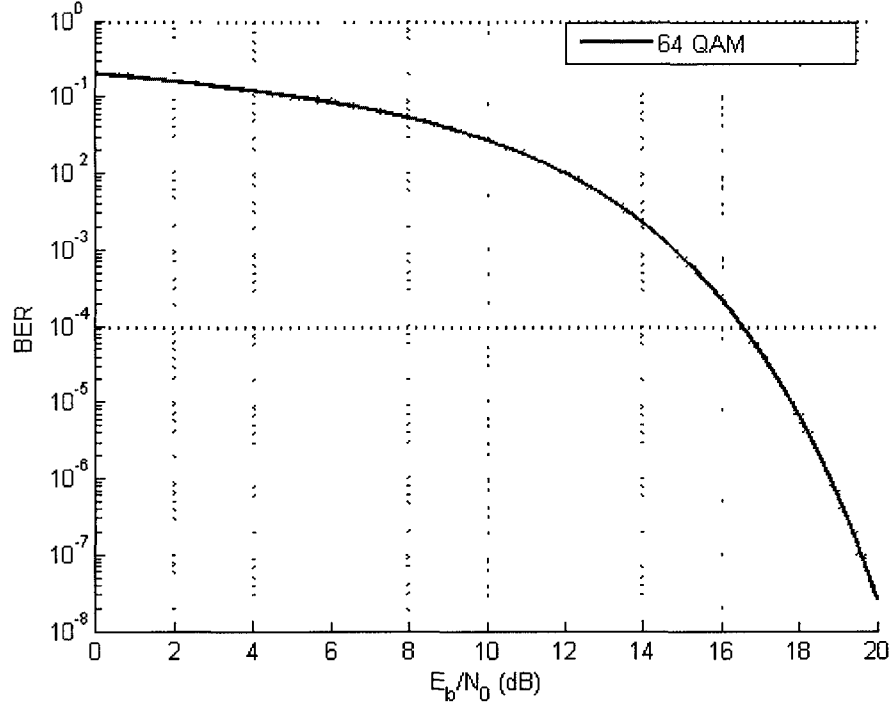
Figure 2-4 BER v.s. $\dfrac{E_b}{N_0}$ for 64 QAM

Since the radio is designed for the last link to the home as compared to the telco backbone, the target BER for the receiver can be set relatively high at 10^{-6}. From Fig. 2.4, the corresponding E_b/N_0 is 18.5 dB. The SNR is a function of E_b/N_0, sampling frequency, f_s bandwidth BW, type of modulation and code gain as given by: [26]

$$SNR_{dB} = \frac{E_b}{N_0} + 10 \cdot \log\left(\frac{\text{Symbol rate}}{BW}\right) + 10 \cdot \log(N) - \text{code gain}_{dB} \qquad (2.2)$$
$$26.6dB = \quad 18.8 + 0 + 7.8 + 0$$

In this design the sampling frequency is equal to the BW (= 225 MHz) and code gain equal to 0 dB since no redundancy is introduced. Therefore the receiver requires a SNR of 26.6 dB.

For the transmitter, the figure of merit is error vector magnitude (EVM) normally expressed in percentage. It is the deviation from a reference input modulated signal, and EVM can be related to SNR through the following formula: [26]

$$EVM = -10^{-SNR/20}$$
$$4.7\% = 10^{-26.6/20}$$

(2.3)

Thus for a SNR of 26.6 dB, the required EVM is 4.7%.

The insertion loss of the diplexer has a direct dB for dB degradation on the receiver SNR since it reduces the received signal. On the transmitter side, the diplexer insertion loss reduces the output power and consequently increases dB for dB the linear output power specification for the transmitter power amplifier (PA).

2.1.5 Link budget, dynamic range, system gain and antenna gain.

The allowable path loss of this wireless communication link can be estimated based on the operating frequency and range. For a minimum and maximum range of 100 and 800 metres, respectively, and operation between 56 and 59 GHz, the losses can be calculated as follows:

$$\text{Path Loss}_{dB} = 20 \times \log \left(\frac{4 \times \pi \times \text{range[m]}}{c[m/s] \Big/ f[1/s]} \right)$$

$$-107.41 \text{dB} = 20 \times \log \left(\frac{4 \times \pi \times 100}{3 \times 10^8 / 56 \times 10^9} \right)$$

$$-125.47 \text{dB} = 20 \times \log \left(\frac{4 \times \pi \times 800}{3 \times 10^8 / 56 \times 10^9} \right)$$ (2.4)

$$-107.86 \text{dB} = 20 \times \log \left(\frac{4 \times \pi \times 100}{3 \times 10^8 / 59 \times 10^9} \right)$$

$$-125.92 \text{dB} = 20 \times \log \left(\frac{4 \times \pi \times 800}{3 \times 10^8 / 59 \times 10^9} \right)$$

From Fig.2.1 the oxygen absorption in 59 GHz is around 20 dB/km. Therefore, the dynamic range of the receiver has to be $-107.41 - (-125.92) + 0.7 \times 20 = 32.52 dB$

The approximate transmitter gain at millimeter-wave frequency (this gain does not include gain at base-band and intermediate frequency (IF) stages) can be designed and set as the difference between the receiver threshold level and saturation level of the transmitter. Before calculating these two power levels some assumptions must be made. Assume the output power of the transmitter PA is 10 dBm at 1 dB compression. This will be the maximum power before the diplexer. Also assume the noise figure (NF) of the transmitter is 10 dB. This is an iterative process for one can always assume a different value if the system gain specification is too difficult to realize. Then the threshold level of the transmitter can be estimated as follows:

$$\text{Threshold Level}_{dBm} = \text{Noise Floor}_{dBm} + \text{Noise Figure}_{dB} + 10 \times \log(\text{symbol rate}) + \text{SNR}_{dB}$$
$$-31\text{dBm} = \text{-}90.48 + 10 + 10 \times \log(255) + 26.6$$

$$(2.5)$$

where noise floor can be calculated as:

$$\text{Noise Floor}_{dBm} = -174 + 10 \times \log(\text{BW}_{Hz})$$
$$-90.48\,\text{dB} = \text{-}174 + 10 \times \log(255 \times 10^6) \qquad (2.6)$$

The maximum output power before saturation depends on the modulation format; higher-order modulation requires more TX power back-off before the PA saturates. This power back-off is also called peak-to-average power radio (PAPR). It also depends on the type of filtering used for the modulated signal [5]. Table 3 shows the power back-off required for different modulated signals [5].

Table 3: PAPR of the constellations for different modulation schemes [5]

Modulation	PAPR [dB]
N-PSK	0
16-QAM	2.6
32-QAM	2.3
64-QAM	3.7 *
128-QAM	4.3

Root raised-cosine filtering (RRC) is used in the modulator at baseband. The roll-off of the RRC filter contributes some inter-symbol interference (ISI) since it is not an ideal brick-wall response. There should also be power back-off associated with the RRC filter's response truncation factor α. The relationship of PAPR vs. α is given in Table 4 [4].

14

Table 4: PAPR of the RRC filter for different α

α	PAPR [dB]
0.15	6.3
0.2	5.6
0.3	4.5
0.4	3.5
0.5	2.8

In order to have greater design freedom, data from Table 4 are curve fitted with a third order polynomial, as follows:

$$\text{PAPR}_{\text{RRC filter}} = 8.5226 - 16.188 \times \alpha + 8.1022 \times \alpha^2 + 2.7322 \times \alpha^3 \quad (2.7)$$

Using Table.3. and equation (2.7) together with the P1dB point chosen previously and setting α of RRC filter equals to 0.7, the maximum TX power can be calculated as follow:

$$\text{Max.TX}_{\text{dBm}} = \text{P1dB} - \text{PAPR}_{\text{QAM 64}} - \left(8.5226 - 16.188 \times \alpha + 8.1022 \times \alpha^2 + 2.7322 \times \alpha^3\right) \quad (2.8)$$
$$4.2\text{dBm} = 10 - 3.7 - \left(8.5226 - 16.188 \times 0.7 + 8.1022 \times 0.7^2 + 2.7322 \times 0.7^3\right)$$

Therefore, system gain can be designed or estimated as: $4.2 - -31 = 35.2 dB$

The system gain is another important parameter of diplexer design, since the desired signal, unwanted emissions and spurious signals are all amplified by the same amount. As a result, the diplexer has to overcome this gain to attenuate unwanted emissions and spurious to the specified out of band levels.

After the maximum transmitted power is set, the maximum antenna gain of the transceiver can be calculated. From Table 2, the maximum equivalent isotropic radiated power (EIRP) is 55 dBm. The difference between the EIRP and the maximum transmitter power is the required antenna gain.

$$\text{EIRP}_{\text{max}} - \text{MAX.TX power} = 55\,\text{dBm} - 4.2\,\text{dBm} = 50.8\,\text{dBi}.$$

This antenna gain is a very liberal value. Since this radio is designed for point-to-point applications, the antenna needs to be very directive, i.e. have narrow beam-width and high gain. Typically, a two feet dish antenna at V band has directivity approximate to 45 dBi [27] which is less than 50.4 dBi. Assuming both TX and RX have identical antennas with 100% efficiency (so that antenna directivity equals antenna gain), thus the maximum and minimum RX power is:

$$\text{Max. RX Power}_{dBm} = \text{TX Power}_{dBm} + G_{TX} + \text{Min. Path Loss}_{dB} + G_{RX} + \text{Oxygen Obsorption}$$
$$-15.21\,dBm = 4.2\,dBm + 45\,dBi - 107.41\,dB + 45\,dBi - 2$$

$$\text{Min. RX Power}_{dBm} = \text{TX Power}_{dBm} + G_{TX} + \text{Max. Path Loss}_{dB} + G_{RX} + \text{Oxygen Obsorption}$$
$$-47.72\,dBm = 4.2\,dBm + 45\,dBi - 125.92\,dB + 45\,dBi - 16$$

$$(2.9)$$

The diplexer must ensure that any TX leakage, unwanted emissions and spurious signals other than the desired RX signal are attenuated (i.e. are no higher than the sensitivity of the receiver).The diplexer also needs to prevent any incoming signals from exceeding the limits which will saturate the receiver. The final system specifications are summarized in Table 5

Table 5: Final designed system specifications

System specifications	
Data rate	1.35 Gb/s
BER	1×10^{-6}
Modulation	64-QAM
System SNR	26.6 dB
System NF	10 dB
Max TX power	4.2 dBm
Max. EIRP	44.2 dB
System Gain	35.2 dB
Dynamic range	32.52 dB
Max./Min. RX power	-15.21/-47.72 dBm

2.1.6 Radio architecture

A single LO transceiver architecture is used as shown in Fig. 2.5. The single LO
frequency is placed at CS away from the TX frequencies and twice CS away from the RX
frequencies. Effectively, the IF of the TX signal is at twice CS or 2 GHz, and the IF of
the RX is at 3.9GHz or four times CS minus the guard bandwidth. Notice that there can
be another down-converting stage at the RX to bring both the TX and RX IF to the same
frequency. The main advantage of the single LO design is its simplicity and lower cost.
At V band, an LO line-up needs to have at least 10 dBm power to drive a mixer. It is
difficult and expensive to build such a high power LO line-up as it needs power output
higher than the whole transmitter. The main drawback of this topology is that the LO
frequency is in-band, so extra filtering or LO-rejection to keep LO leakage within
specification is required. In addition, since the IF is in the sub-GHz range, the spurious
frequencies at $\text{spurious frequencies} = m \times \text{LO frequencies} \pm n \times \text{IF frequencies}$ (2.11)are also
close to the band requiring difficult rejection specifications for the diplexer.

Figure 2.5 shows the millimeter-wave blocks of the transceiver. There are only
seven active components: (a) a voltage controlled oscillator (VCO) tunable over 13.5
GHz or an equivalent phase lock loop (PLL) system for more stable frequencies; (b) two
image reject 2nd harmonic mixers; (c) a frequency multiplier; (d) a driver amplifier; (e)
the PA; (f) the LNA; and (g) the I/Q modulator /demodulators. The features of each
component will be discussed in turn.

17

System Diagram and Frequencies of
Tx Band 'A' and Rx Band ' B' [MHz]

Sub Harmonic
Image Rej
Mixer

90° hybrid

Tx Modulator

90°

Q

2000 + 4 x 225

Driver   PA

13525-13750

56100-57000

27050-27500

Microwave
VCO   LO Filter   Freq
X2   Power splitter

Tuning Range =225

90° hybrid /
Sideband select

Rx Demodulator

90°

Q

3900 + 4 x 225   Sub Harmonic
Image Rej
Mixer

Diplexer

LNA

58000-58900

58000-58900
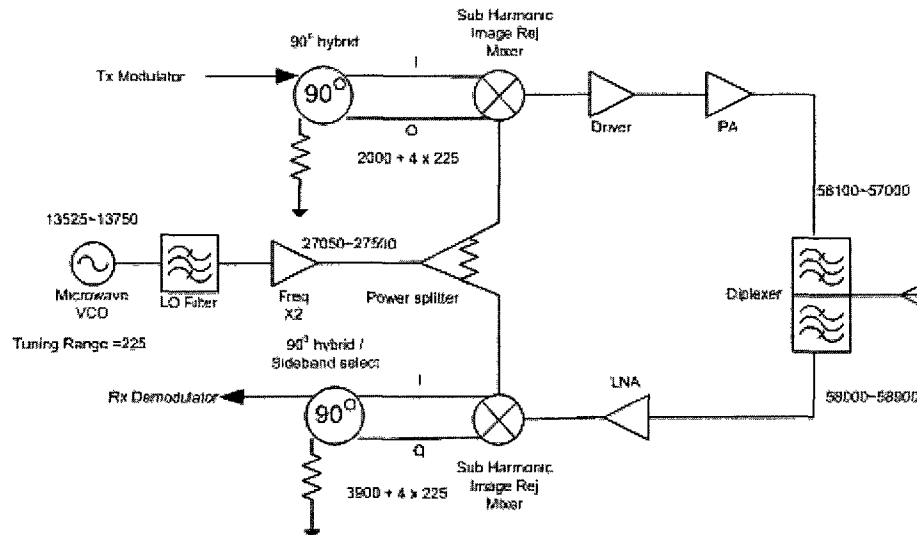
Figure 2-5 Single LO transceiver architecture with signal frequency at various points.

(a) The VCO has to have a tuning range from 13.525–13.750 GHz to cover the entire TX
and RX channels. Since the frequency multiplier normally has a driver built in, and
using a 2nd harmonic mixer, the diplexers need to attenuate 4th order of VCO signals
at the PA output. They must also attenuate any fifth harmonic from the VCO that will
get amplified by the gain blocks of the transmitter. An LO filter must be used after
the VCO to block any spurious or harmonics produced by the VCO since, if allowed
to pass, they would produce severe intermodulation products in the frequency
multiplier. A LO filter will be designed in Section 3.2.3.

(b) Two identical 2nd harmonic image reject mixers are used. On the transmitter side this
component mixes the input IF message signal with the 2nd harmonic of the LO
frequency to produce the upconverted RF signal. On the receiver side it mixes the
incoming modulated RF signal with the 2nd harmonic of the LO frequency to produce
the downconverted IF signal. At the same time, each mixer provides some LO
rejection and some image rejection. The image rejection ratio (IRR) is given by the
following formula:

$$IRR_{dB} = 20 \cdot \log\left(\frac{1 - \alpha \cdot (1+\varepsilon) \cdot \cos\theta + (1+\varepsilon)^2}{1 + \alpha \cdot (1+\varepsilon) \cdot \cos\theta + (1+\varepsilon)^2}\right)$$

Where:

ε = voltage mismatch

α = voltage amplitude and

θ = phase imbalance

(2.12)

For this radio system design, a mixer with 12 dB image rejection and 30 dB LO suppression is chosen.

(c) Frequency multipliers are used after the VCO to output the desired LO frequency and also correct level. The main reason of using them is that the microwave oscillators have poorer phase noise at higher frequency. Even though a multiplier introduces 6 dB more phase noise to double VCO carrier frequency, it may be still better off than using a VCO fundamental at double frequency. A power splitter divides the LO power after the frequency multiplier into the LO ports of both the TX and RX mixer. The frequency multiplier usually has its own buffer amplifier on chip. Since the sub-harmonic mixers need high LO drive power in order to achieve good linearity, if this LO line-up does not have enough output power level to drive two mixers at same time, two frequency multipliers may be needed after the power splitter.

(d) The driver amplifier provides enough gain to overcome conversion loss from the mixer and also to satisfy the designed system gain.

(e) The PA will also have some gain and a sufficient P1dB level to provide the required power output and power back-off for modulation.

(f) The LNA boosts the received RF signal before down-conversion and demodulation.

(g) Two 90° hybrids each provides in phase (I) and quadrature (Q) input for the image reject mixer at IF. The amount of image rejection is a function of the voltage amplitude mismatches and phase imbalance of I and Q as shown in Eqn. (2.1.11).

There are two hybrids needed for image reject operation: an IF frequency one (3~5 GHz in Fig.2-5), which separates the IF signal; and a RF hybrid which combines mixed signals after the mixers. [16] The IF hybrid is physically large since it operates at much lower frequencies than the RF components. These IF hybrids can be realized as printed circuits on the microwave frequency substrate. The hybrid at millimeter wave frequencies is built on the mixer ICs.

2.1.7 Effect of unwanted emissions spurious signals on diplexer's specifications

In order to design the diplexer for the radio architecture described in the previous section, it is necessary to determine possible sources and levels of unwanted emissions and spurious signals. Once these are known, the filter response for the diplexer can be specified. The signals of concern are TX leakage to the RX channel, LO leakage, and spurious signals.

The TX power output is normally high. Without proper isolation, its leakage will saturate the receiver. In Section 2.1.5, the minimum RX power or the receiver's sensitivity is chosen to be -47.72 dBm and maximum TX power is 4.2 dBm. Assume that the shortest link is 100 metres. Therefore the rejection for TX will be:

$-15.21dBm - (-47.72dBm) + 2.5dB(\text{margin}) = 35dB$ (2.13) rejection is needed to make any TX leakage below the RX detectable range.

The LO power is usually very strong, about 10dBm, to drive the 2nd harmonics image reject mixer. It is always better to place the LO signal out of band, since the out of band emission requirement is much looser than the in-band emission. However, in some cases due to the VCO or PLL limitations, the LO has to be placed in band. In these cases, the diplexer needs to offer higher rejection for in-band LO leakage. The amount of LO rejection can be estimated using the following equation:

$$\text{LO Rejection} = \text{LO power} - \text{Mixer LO rejection} + \text{TX gain} - \text{IL} - \text{ESTI regulation}$$
$$41.7\,\text{dB} = 10\,\text{dB} - 30\,\text{dB} + 35.2\,\text{dB} - 3.5\,\text{dB} - (-30\,\text{dB}) \tag{2.14}$$

Thus 41.7dB rejection is required for LO leakage.

The main spurious signals of this radio are TX images, LO plus 2nd and 3rd harmonics of the TX signals. In reality, there are other sources of spurious signals such as higher harmonics of the TX mixing with LO, and signals from neighboring channels. However these are not considered in the diplexer specification, since higher harmonics are usually small, and for point-to-point radio applications, antennas are very directional and hence signals from neighboring channels can be ignored. For the worse scenario, consider the image signal power to be equal to P_{1dB} of the transmitter. Then the amount of image rejection can be estimated as follows:

$$\text{Image rejection} = \text{P1dB}_{output} - \text{TX power backoff} - \text{IL}$$
$$- \text{Mixer image rejection} - \text{ETSI regulation} + \text{margin} \tag{2.15}$$
$$23.7\,\text{dB} = 10\,\text{dBm} - 5.8\,\text{dB} - 3.5\,\text{dB} - 12\,\text{dB} - (-30\,\text{dB}) + 5\,\text{dB}$$

Assume that the second and third harmonics of the TX has level -10 dBc, and there is no IF filter, the diplexers rejection requirements for 2nd and 3rd harmonics can be estimated as follow:

$$\text{Harmonic rejection} = \text{P1dB}_{output} - \text{TX power backoff} - \text{IL}$$
$$- \text{level relative to carrier} - \text{ETSI regulation} + \text{margin} \tag{2.16}$$
$$25.7\,\text{dB} = 10\,\text{dBm} - 5.8\,\text{dB} - 3.5\,\text{dB} - 10\,\text{dBc} - (-30\,\text{dB}) + 5\,\text{dB}$$

The following table and plots summarize the specification of the diplexers.

Table 6: Diplexer specifications

Diplexer specifications		
	Rejections [dB]	Frequency offset [GHz]
TX-RX isolation	35	2
LO leakage isolation	41.7	2
TX image rejection	23.7	4
RX image rejections	23.7	8
IF 2nd harmonics rejections	25.7	2
IF 3nd harmonics rejections	25.7	4
IL	3.5	N.A
Passband flatness	0.5	N.A
Group delay	5 nsec average	Across passband

TX BPF Requirements
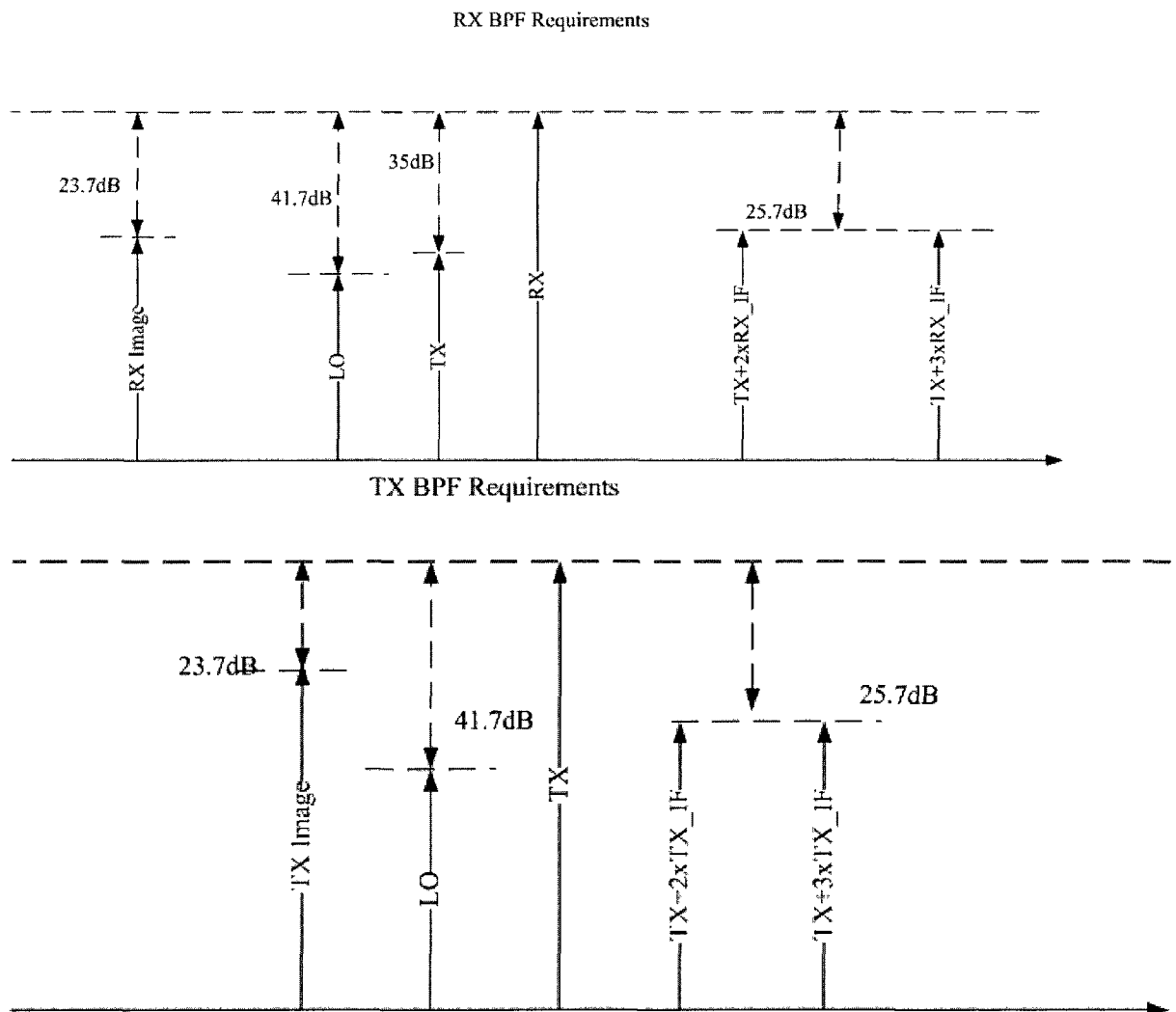
Figure 2-6   Diplexer specifications plots.

Even though the TX and RX filter requirements are different, for design simplicity, a similar and tougher rejection specification BPF is designed for both TX and RX. Noticing that the LO rejection is the toughest specification, it limits the TX filter more than the RX filter since the TX IF is closer and the RX IF being far away from the LO, however the RX filter also need to reject the LO from TX path.

2.1.8 Other considerations for diplexer specification

Several other considerations are important for setting the specifications for the duplexer. These are: (a) the TX noise suppression at the RX; (b) the 2nd order compression point; and (c) group delay.

(a) TX noise suppression at RX:

Due to the finite isolation of the diplexer between the TX and RX, some noise from the TX will leak into the RX. The following calculation estimates the TX noise suppression at RX for the chosen radio design. The thermal noise floor is 174 dBm/Hz at 290K:

$$\text{Thermal Noise Floor} \left[\text{dBm/Hz}\right] = 10 \times \log(k \cdot T)$$
$$-174\left[\text{dBm/Hz}\right] = 10 \times \log\left(1.38066 \times 10^{-23} \cdot 290\right) \quad (2.17)$$

where k is Boltzmann constant and T is temperature in Kelvin. The TX noise output is -148.78 dBm/Hz:

$$\text{TX noise temperature} \left[\text{dBm/Hz}\right] = \text{Noise floor} + \text{NF}_{\text{TX}} + \text{TX gain}$$
$$-148.78\left[\text{dBm/Hz}\right] = -173.98\left[\text{dBm/Hz}\right] + 10\,\text{dB} + 15.2\,\text{dB} \quad (2.18)$$

The corresponding TX noise temperature is 96028.03K:

$$\text{TX noise temperature} = 10^{\frac{\text{TX noise output -30}}{10}} \Big/ k$$
$$96028.03\,k^{0} = \frac{10^{\frac{-148.78-30}{10}}}{1.38066 \times 10^{-23}} \quad (2.19)$$

The RX equivalent noise temperature with 8 dB receiver NF in degree Kelvin is 1539.78K

$$\text{RX noise temperature} \left[k^0\right] = T \times \left(10^{\frac{NF_{RX}}{10}} - 1 \right)$$
$$1539.78 \left[k^0\right] = 290 \times \left(10^{\frac{8}{10}} - 1 \right) \quad (2.20)$$

From the previous section, for TX-RX minimum isolation of 25.7 dB, the TX noise temperature at the RX is $-148.78\,\text{dBm}/\text{Hz} - 25.7\,\text{dB} = -174.48\,\text{dBm}/\text{Hz}$.

The corresponding TX noise temperature at the RX is 258.46K:

$$258.46 \left[k^0\right] = \frac{10^{\frac{-174.48-30}{10}}}{1.38066 \times 10^{-23}} \cdot \quad (2.21)$$

Therefore the equivalent RX noise temperature is $1539.78 + 258.46 = 1798.24\,k^0$. Lastly the effective NF at RX can be calculated to be 8.57 dB as follow:

$$\text{Effective RX NF} \left[dB\right] = 10 \times \log\left(1 + \frac{\text{EffectRX noise temperature}}{T}\right)$$
$$8.57\,dB = 10 \times \log\left(1 + \frac{1798.24}{290}\right) \quad (2.22)$$

Therefore the RX noise degradation due to the TX NF and finite diplexers TX – RX isolation is 0.57 dB.

(b) 2nd order compression point (IP2):

Intermodulation products are created if there is more than one signal appearing at the RX. This is particular important for the receiver's mixer design. Firstly, consider that the TX leakage to be the most severe (in term of amplitude) source at receiver's input. The TX leakage at receivers mixer input is estimated as follows. Assuming that LNA has 20 dB small signal gain the TX leakage at the receiver's mixer input is estimated to be – 15.7 dBm:

$$\text{TX leakage at RX mixer input} = \text{P1dB}_{\text{output}} - \text{Diplexers IL - TX - RX isolation} + \text{LNA gain}$$
$$- 15.7\,\text{dBm} = 4.2\,\text{dBm} - 3.5\,\text{dB} - 35\text{dB} + 20\,\text{dB}$$
$$(2.23)$$

Assuming the down-convert mixer has 12 dB conversion loss (CL) and has input IP2 of 20 dBm, the intermodulation ratio (IMR) is 25dBc:

$$\text{IMR} \left[\text{dBc} \right] \approx \text{Mixer IP2 - spurious at mixer input} = 25 \text{ dBc} \quad (2.24)$$

Then, the maximum spurious power at the mixer input can be calculated as –30dBm:

$$P_{\text{Spurious}} \left[\text{dBm} \right] = \text{input IP2 - 2} \times \text{IMR} \\ -30 \text{ dBm} = 20 \text{ dBm - 2} \times 25 \text{ dBc} \quad (2.25)$$

The maximum spurious power at the LNA input is –50dBm:

$$P_{\text{Spurious}} \text{ at LNA input} \left[\text{dB} \right] = P_{\text{Spurious}} \text{ at mixer input - Gain}_{\text{LNA}} \\ -50 \text{ dBm} = -30 \text{ dBm - 20 dB} \quad (2.26)$$

The maximum spurious level at the LNA is approximately -50 dBm which is within the regulation as well as below the minimum received signal level. This implies that, with the assumed mixer linearity performance and LNA and diplexer specifications, the ETSI spurious regulation is met.

(c) Group delay

Group delay is the delay of the modulated signal passing through the diplexer. Group delay is not constant across the frequency band. Such variation in group delay will cause poor signal fidelity and hence introduce ISI. In this diplexer design, an average 5nsec group delay specification is chosen.

Considering all of these requirements as well as the requirements from the previous section, it can be seen that the most difficult specification for the diplexer is the amount of LO rejection. However, some LO nulling techniques can be used to alleviate this specification. One technique is to control or adjust the amount of DC bias of the quadrature IF input signals into the image reject mixer. This technique can suppress the LO by more than 10 dB. [8]

2.1.9 TX and RX line-up measurements

Both TX and RX modules for the specified radio design were built using commercial off-the-shelf MMIC chips on 5 *mil* thick ©Rogers RT/Duroid soft board. The experimental modules are blocks of the transceiver system shown in Fig 2.7. The TX module consists of a © Mini Circuit IF 90° hybrid, a ©United Monolithic Semiconductor (UMS) image rejection sub-harmonic mixer [16], a ©Hittite V-band small power driver [17] plus a medium power PA [18] and lastly a 50Ω microstrip to WR15 waveguide launch. The RX line up consists of a WR15 waveguide to 50Ω microstrip transition, an ©UMS LNA [19], another identical image rejection sub-harmonic mixer followed by another IF 90° hybrid. A DC bias network with surface mount components was built around the active components on the module.

Table 7: Some key specifications of MMIC used

Subharmonic Image Reject Mixer	Conversion loss 12 dB	Output P1dB 0 dBm	Image Reject 8 dB
Driver	Gain 13 dB	Output P1dB 16 dBm	OIP3 25 dBm
PA	Gain 24 dB	Output P1dB 17 dBm	OIP3 25 dBm
LNA	Gain 20 dB	NF 4 dB	Input P1dB -6 dBm
VCO	Oscillation tuning range 12 5 ~ 14 GHz	Tuning range 5 ~ 11V	SSB PN -110 dBc @ 100 kHz offset
Frequency multiplier	Output frequency range 24 ~ 33 GHz	Output power 17 dBm	Fundamental isolation >25 dBc
IF hybrid	Isolation 30 dB	Phase unbalance 1°	Amplitude unbalance 0 5 dB

Figure 2.7 shows the test setup for experimental characterization of the transceiver

:
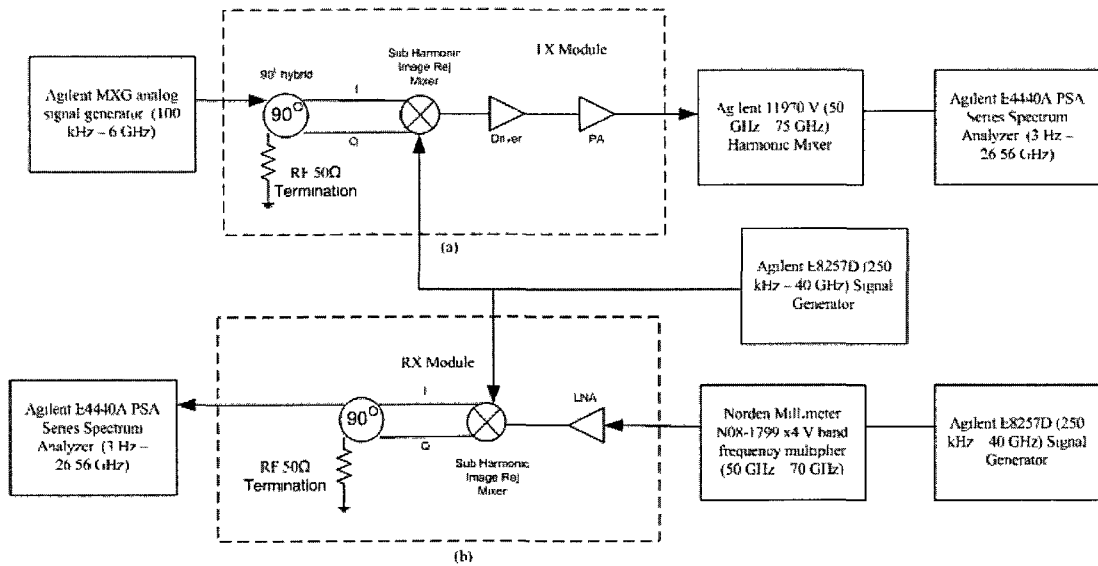
Figure 2-7   (a) TX and (b) RX test setup.

Experimental data for system gain, LO rejection and image rejection are shown in Figure 2.8 as a function of channel frequency. Measurements show that the TX has more than 15 dB gain, 12 dB image rejection and approximately 40 dB LO rejection. These gain, image and LO rejections numbers are used to calculate and validate the performances of the diplexer in Table 5 and Eqn. (2.14). The LO rejection can be improved by the introducing DC bias imbalance into the IF/I and IF/Q channels of the image reject mixer thus providing extra LO nulling. This is normally done by baseband signal processing circuits. The experimental LO rejection curve has a big notch in the 54-60 GHz range. This may be due to the poor matching in between the components dies. The dies are placed very close to each other, and are connected with double 1mil diameter gold bond wires. No matching was used since many of these V band MMICs are designed to achieve a reasonable match when the parasitic inductances of the bond wires are added.
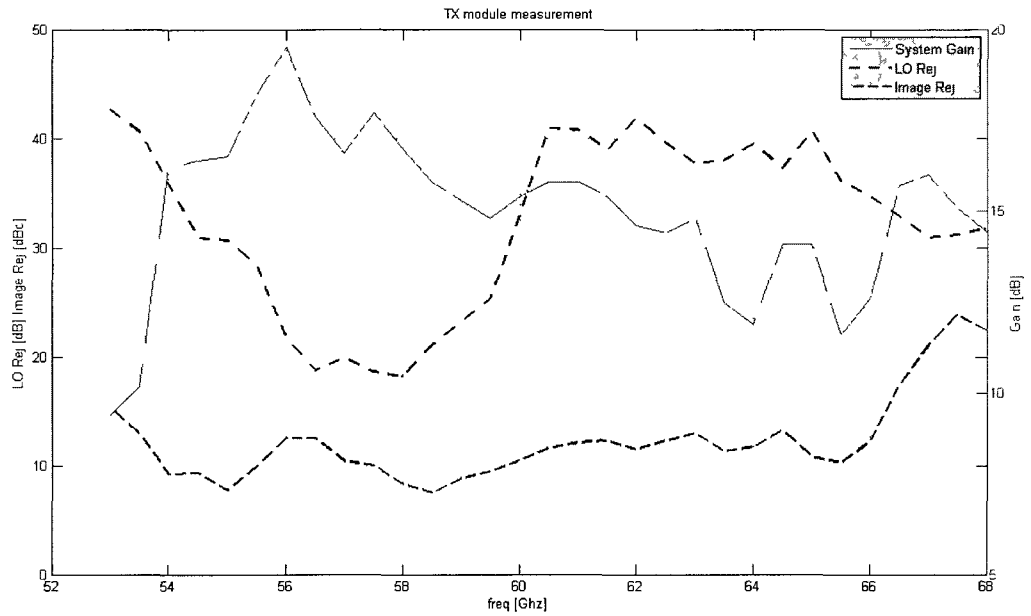
Figure 2-8 TX module measurements

The RX gain and P1dB measurements are given in Figure 2.9 .The RX line-up has a measured input P1dB of approximately –13 dBm (maximum input power to state linear) and minimum RX detectable power of ≤45 dBm. The specifications discussed in Section 2.1.5 and given in Table 5 can be achieved based on datasheet information and validated with prototype module measurements shown above.
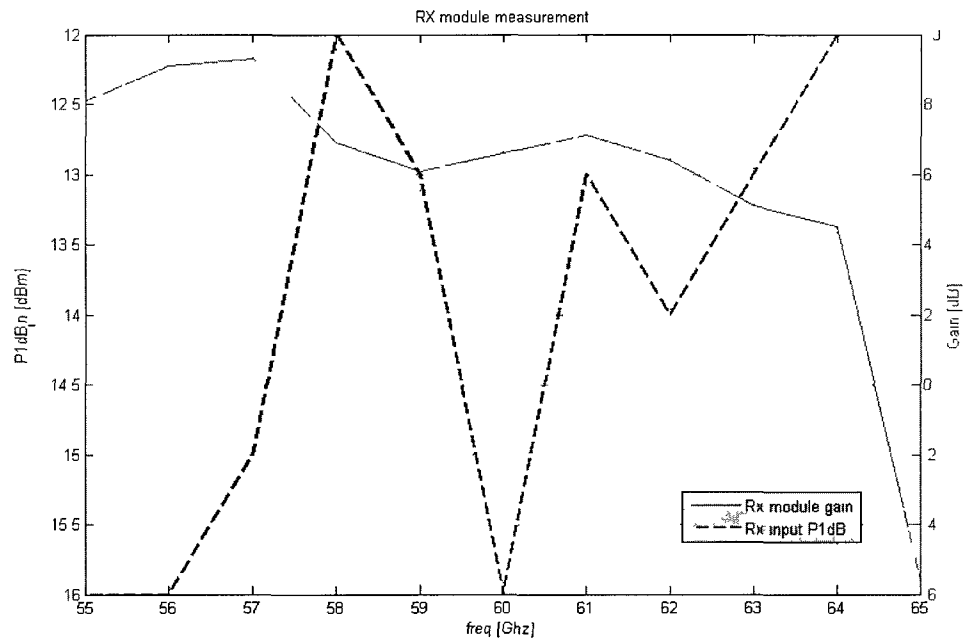
Figure 2-9 RX module measurements

2.2 Filter Theory and Background [6]

2.2.1 Filter characteristics

A filter is a two-port device in which desired signal frequencies are allowed to pass with minimum attenuation, while undesired signal frequencies are attenuated. Here we will consider only passive filters. In the design of a filter, important specifications are frequency range, fractional pass bandwidth (BPF), insertion loss, input return loss (RL), stopband attenuation, and group delay. Figure 2.10 illustrates a two-port filter network with incident power P_{IN}, absorbed power P_A, power delivered to the load P_L, and reflected power P_R.
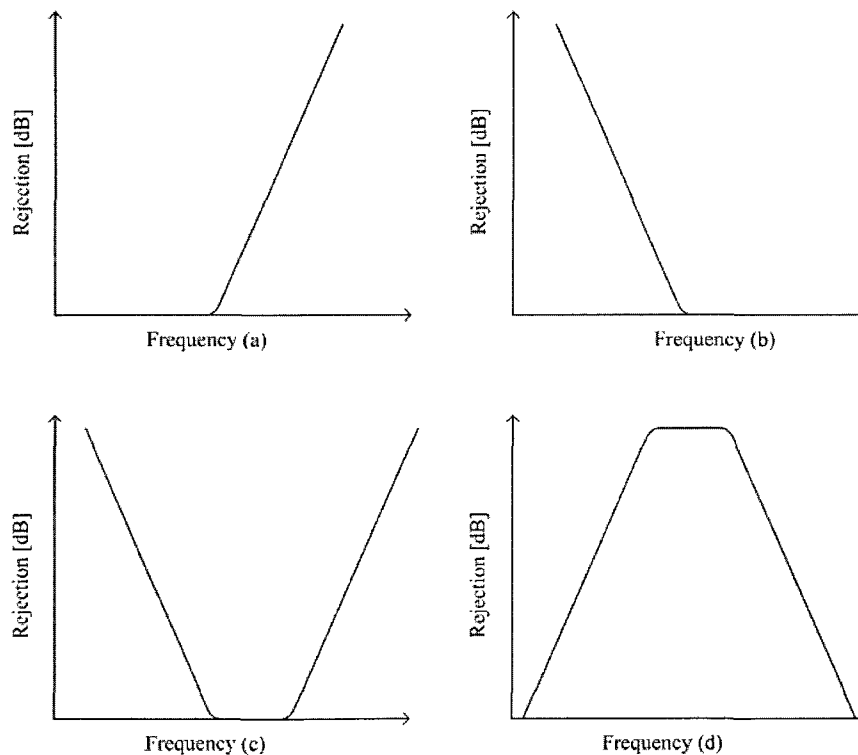
Figure 2-10   Types of filters: (a) low-pass; (b) high-pass; (c) bandpass and (d) bandstop
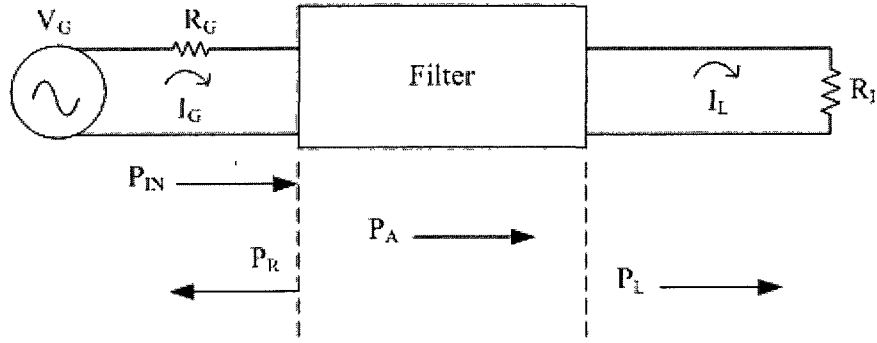
Figure 2-11   Filter network

$$P_{IN} = \frac{V_G^2}{4 \cdot R_G}$$

$$P_L = \left| I_L^2 \right| \times R_L$$

$$P_A = \Re \left| I_G \times (V_G - I_G \times R_G) \right|$$
(2.27)

$$P_R = \frac{V_G^2}{4 \cdot R_G} - \Re \left| I_G \times (V_G - I_G \times R_G) \right| - \left| I_L^2 \right| \times R_L$$

Insertion loss in dB of a filter is defined as the ratio of power delivered to the load and the power into the filter network:

$$IL = -10 \cdot \log \frac{P_L}{P_{IN}}$$
(2.28)

Return loss (RL) in dB of a filter is defined as the ratio of reflected power and the power delivered into the filter network, it can also be implemented with VSWR.

$$RL = -10 \cdot \log \frac{P_R}{P_{IN}} = -10 \cdot \log \left(\frac{VSWR - 1}{VSWR + 1} \right)^2$$
(2.29)

The group delay in seconds, is defined as the negative rate of transmission phase angle with respective to angular frequency, where the transmission phase angle   is the angle of the S21 scattering parameter.

$$\tau_D = -\frac{d\phi}{d\omega} = -\frac{1}{2 \cdot \pi} \cdot \frac{d\phi}{df}$$
(2.30)

32

In general, there are four different types of filters. Low-pass, high-pass, bandpass and bandstop. Their responses are shown in the following figure.

Within the passband or band reject regions, the filter can have different types of response, as discussed next

2.2.2 Filter prototypes and synthesis

The most popular method of filter synthesis is to initially use a low-pass filter prototype with required cutoff frequency, in-band response, and out of band attenuation and then transform this ideal low-pass filter to the desired bandpass response with specific centre frequency and FBW.

The low-pass prototype design procedure begins with specifying the desired filter in-band insertion loss or return loss frequency response, cutoff frequency, and out of band rejection. Three different low-pass filter prototypes are discussed here. These are filters having (a) Butterworth (or maximally flat) response; (b) Chebyshev (or equal ripple) response; or (c) pseudo-elliptic response. Figure 2.12 shows the typical responses of these three prototypes.
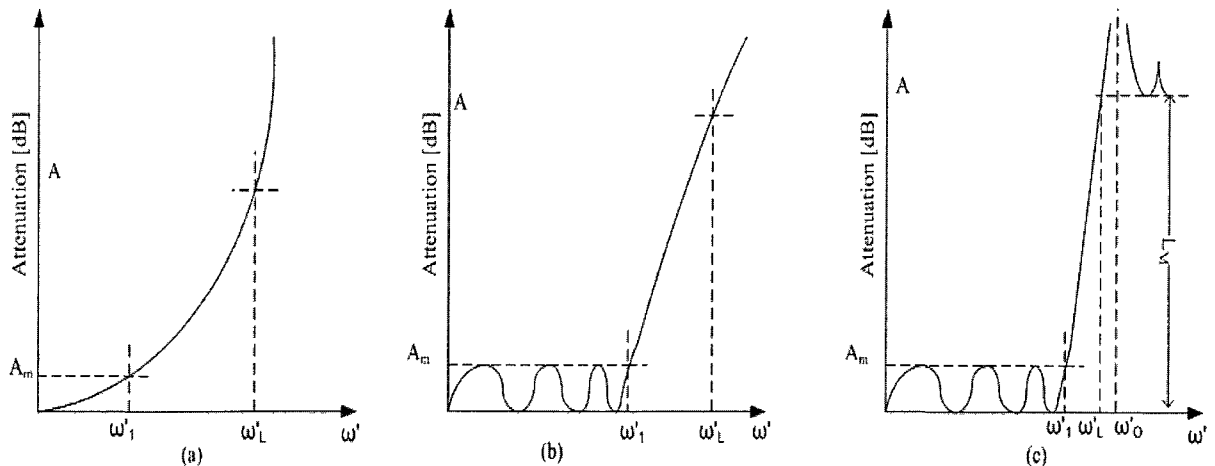
Figure 2-12   Typical low-pass prototype attenuation responses: (a) Butterworth; (b) Chebyshev and (c) pseudo-elliptical responses

(a) Butterworth response:

The attenuation or insertion loss of Butterworth response is follow:

$$\left| \text{Attenuation}^2_{\text{Butterworth}} \right| = \frac{1}{1 + \varepsilon^2 \left(\dfrac{\omega'}{\omega'_1} \right)^{2n}} \quad (2.31)$$

where n is the order of the filter. ε defines IL at cut-off frequency, ω'_1. It is common normalize and to set $\omega'_1 = 1$. The filter has IL of 3 dB at ω'_1. The following formula can be used to determine the minimum order to achieve certain stopband attenuation (A) at frequency f_S:

$$n \geq \frac{\log\left(10^{0.1 \cdot A} - 1\right)}{2 \cdot \log(f_s)} \quad (2.32)$$
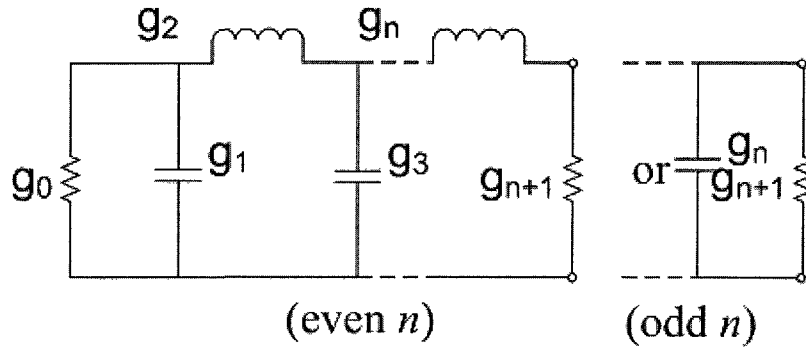
Figure 2-13   Low-pass prototype ladder network structure

The elements of the prototype ladder networks may be computed by:

$$g_0 = g_{n+1} = 1$$
$$g_k = 2 \cdot \sin \frac{(2 \cdot k - 1) \cdot \pi}{2 \cdot n} \text{ for } k = 1,2 \cdots n \quad (2.33)$$

(b) Chebyshev response

The Chebyshev low-pass prototype has better attenuation at stopband. However, it also exhibits passband ripple which is a function of input matching, i.e.

34

$$A_m = -10 \cdot \log\left(1 - 10^{0.1 \, RL_{MIN}}\right) \quad (2.34)$$

$$\left|\text{Attenuation}_{\text{Chebyshev}}^2\right| = \frac{1}{1 + \varepsilon^2 \cdot T_n^2\left(\dfrac{\omega'}{\omega'_1}\right)}$$

$$T_n^2\left(\frac{\omega'}{\omega'_1}\right) = \begin{cases} \cos\left(n \cdot \cos^{-1}\left(\dfrac{\omega'}{\omega'_1}\right)\right) & \left|\left(\dfrac{\omega'}{\omega'_1}\right)\right| \le 1 \\ \cosh\left(n \cdot \cosh^{-1}\left(\dfrac{\omega'}{\omega'_1}\right)\right) & \left|\left(\dfrac{\omega'}{\omega'_1}\right)\right| \le 1 \end{cases} \quad (2.35)$$

where ε is the ripple constant is a function of passband ripple (A_m) of the filter given by:

$$\varepsilon = \sqrt{10^{\frac{A_m}{10}} - 1} \quad (2.36)$$

The order of the require Chebyshev filter to achieve certain A at frequency f_S with certain A_m can be calculated as:

$$n \ge \frac{\cosh^{-1}\sqrt{\dfrac{10^{\frac{A}{10}} - 1}{10^{\frac{A_m}{10}} - 1}}}{\cosh^{-1}(f_s)} \quad (2.37)$$

The elements of the prototype ladder networks as shown in Fig.2-13 may be computed by:

$$g_0 = 1.0$$

$$g_1 = \frac{2}{\gamma} \cdot \sin\left(\frac{\pi}{2 \cdot n}\right)$$

$$g_i = \frac{1}{g_{i-1}} \cdot \frac{4 \cdot \sin\left[\dfrac{(2 \cdot i - 1) \cdot \pi}{2 \cdot \pi}\right] \cdot \sin\left[\dfrac{(2 \cdot i - 3) \cdot \pi}{2 \cdot \pi}\right]}{\gamma^2 + \sin^2\left[\dfrac{(i-1) \cdot \pi}{n}\right]} \quad , \text{for } i = 2,3 \cdots n$$

$$g_{n+1} = \begin{cases} 1.0 & , \text{for odd } n \\ \coth^2\left(\dfrac{\beta}{4}\right), & \text{for even } n \end{cases}$$

$$\beta = \ln\left[\coth\left(\frac{A_m}{17.37}\right)\right] \qquad\qquad\qquad (2.38) \text{ where:}$$

$$\gamma = \sinh\left(\frac{\beta}{2 \cdot n}\right)$$

(c) Pseudoelliptic response:

The main advantage of this low-pass prototype is that it offers steeper roll-off at stop band with the same n compared to the Chebyshev prototype. It is also called generalized Chebyshev since the response is between the Chebyshev and elliptical responses. A pseudoelliptic response has equal-ripple at pass-band; it also has steep response until the transmission zero frequencies, unlike the elliptical response which also exhibits equal-ripple stop-band response. The attenuation is described as follow:

$$\left|\text{Attenuation}_{\text{Pseudoelliptic}}^{2}\right| = \frac{1}{1 + \varepsilon^2 + F_n^2\left(\dfrac{\omega'}{\omega'_1}\right)}$$

$$F_n(\omega') = \cosh\left\{(n-3) \cdot \cosh^{-1}\left[\omega' \cdot \sqrt{\frac{\omega_0'^2 - 1}{\omega_0'^2 - \omega'^2}}\right] + 3 \cdot \cosh^{-1}(\omega')\right\} \quad (2.39)$$

where n is the order of the filter, and   is the ripple constant as shown in Eqn. (2.33). It should be noted that the transmission zeros are located at

frequencies $\omega' = \pm\omega'_0 , (\omega' \geq 1)$, and when $\omega'_0 \to \infty$ the response converts to an ordinary Chebyshev filter. The low-pass prototypes network is shown in Fig. 2.14.

The elements can be synthesized approximately from the following equations:

$$g_0 = 1.0$$

$$g_1 = \frac{2}{\gamma} \cdot \sin\left(\frac{\pi}{2 \cdot n}\right)$$

$$g_i = \frac{1}{g_{i-1}} \cdot \frac{4 \cdot \sin\left[\frac{(2 \cdot i - 1) \cdot \pi}{2 \cdot \pi}\right] \cdot \sin\left[\frac{(2 \cdot i - 3) \cdot \pi}{2 \cdot \pi}\right]}{\gamma^2 + \sin^2\left[\frac{(i-1) \cdot \pi}{n}\right]} \; , \text{for } i = 2,3 \cdots m , m = n/2$$

$$\gamma = \sinh\left(\frac{1}{n} \cdot \sinh^{-1}\frac{1}{\varepsilon}\right)$$

(2.40)

$$S = \left(\sqrt{1+\varepsilon} + \varepsilon\right)^2 \quad (\text{passband VSWR})$$

$$J_m = \begin{cases} \sqrt{S} & , \text{odd } m \\ 1/\sqrt{S} & , \text{even } m \end{cases}$$

$$J_{m-1} = 0 \quad (\text{Chebyshev filter})$$
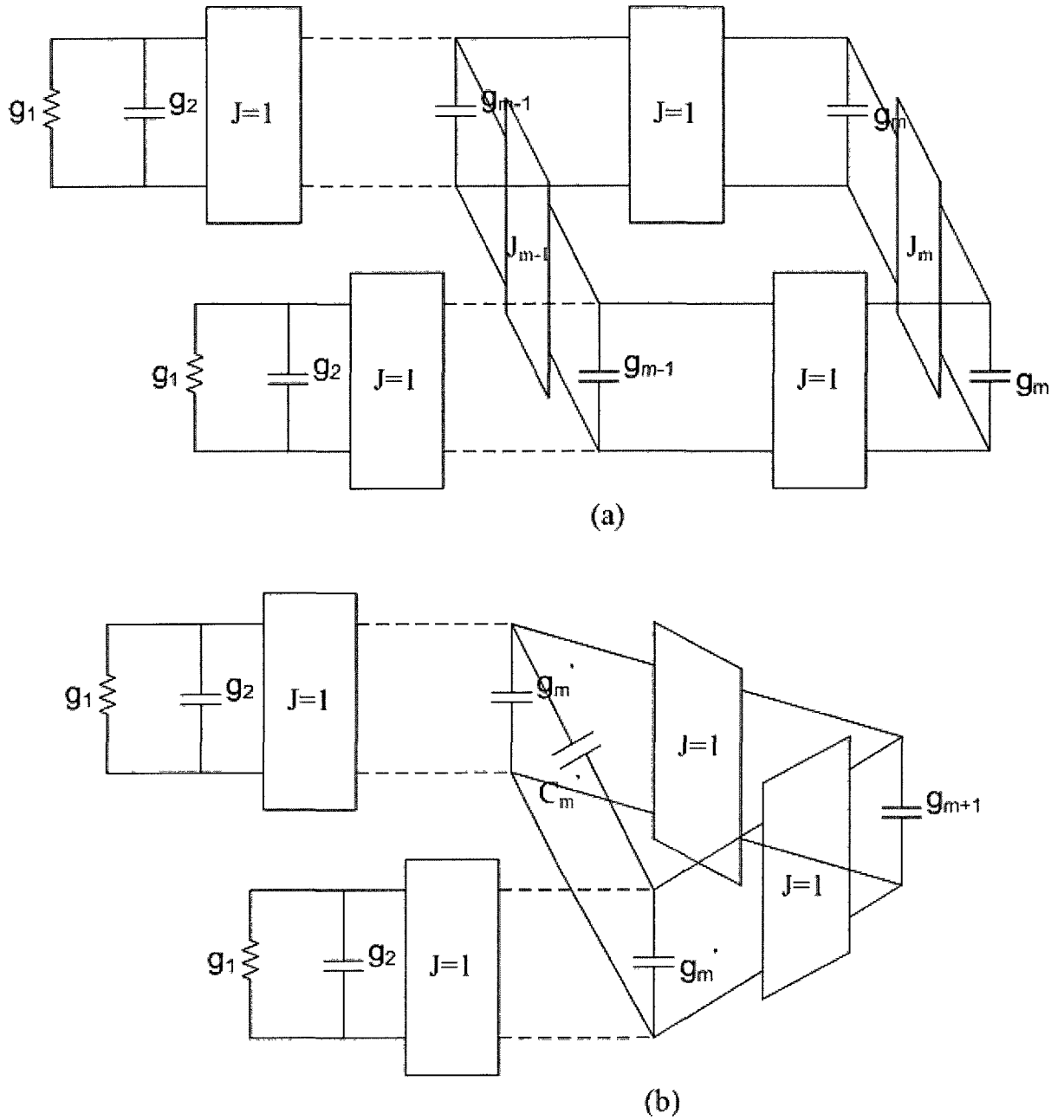
Figure 2-14 Pseudoelliptic Low-pass prototype ladder network structure, (a) even n

$(m = n / 2)$. (b) odd n $(m = (n-1) / 2)$

In order to introduce transmission zeros at $\omega' = \pm\omega'_0$, $(\omega' > 1)$ the required

value for J_{m-1} is given as:

$$J_{m-1} = \frac{-J'_m}{\left(\omega'_0 \cdot g_m\right)^2 - J'^2_m} \quad (2.41)$$

By introducing zero J_{m-1} the filter is slightly mismatched. In order to maintain matching at certain pass band ripple, it is necessary to change the value of J_{m-1} by:

$$J'_m = \frac{J_m}{1 + J_m \cdot J_{m-1}} \quad (2.42)$$

It is unusual to build a filter with odd value for n since it is difficult to realize. Many even n designs are based on two $\frac{n}{2}$ order designs cascaded together with additional coupling tunings. However two alternate realizations for odd n are possible as shown in Fig. 2.15. [7].The asymmetrical form shown in Fig. 2.15(b) adds an additional inverter stage compared to the prototype for even n shown in Fig. 2.14(a). In the symmetrical form, shown in Fig. 2.15(a), the cross coupling is done by a frequency dependent cross-coupling susceptance C'_m that transforms into a resonant element with g_{m+1} [7]
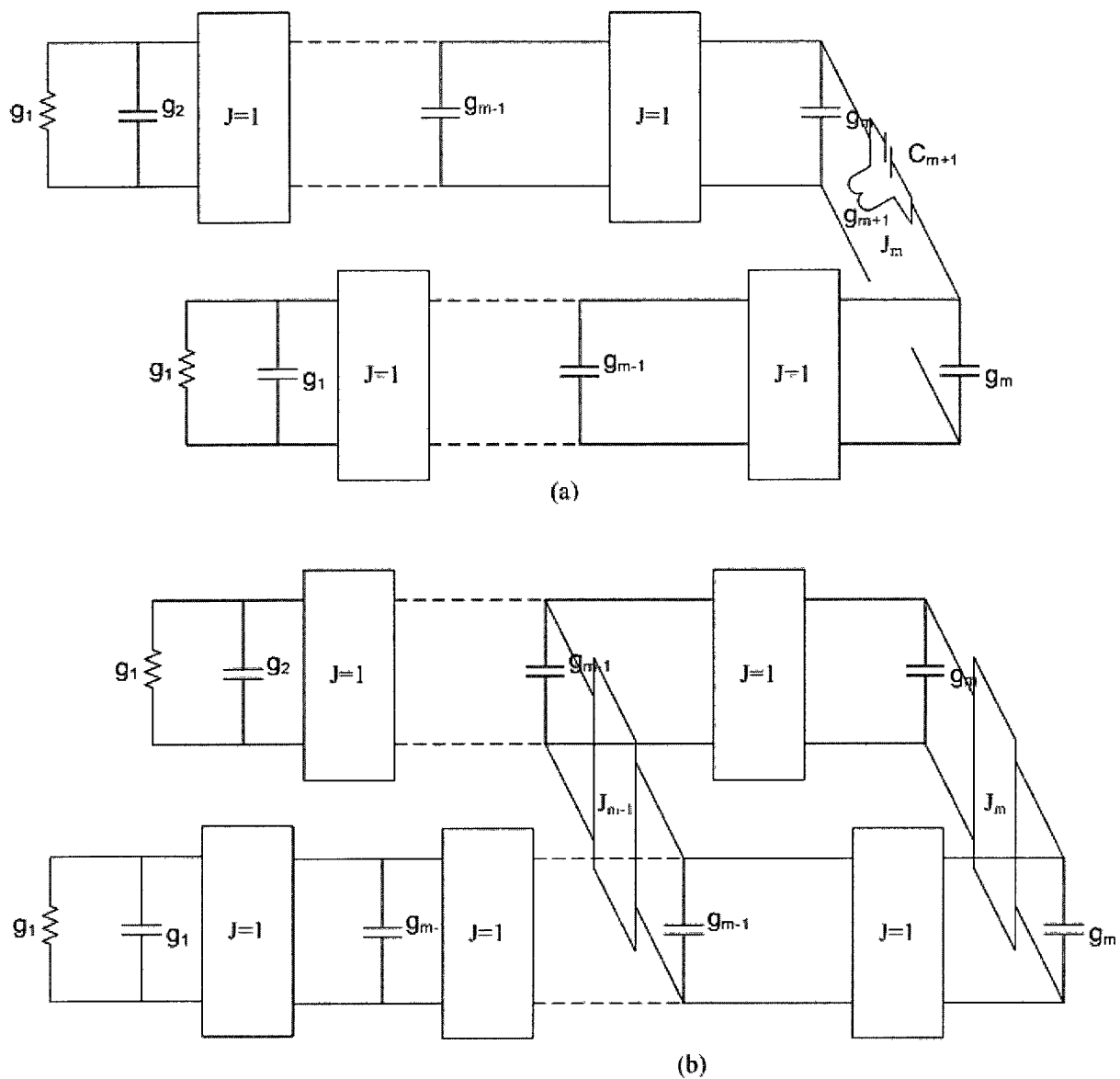
Figure 2-15   Equivalent for odd n , (a) alternative symmetrical realization . (b)

asymmetrical realization

The filter elements shown in Fig. 2.15 are given by

$$J_{m-1} = \frac{C'_m}{g'_m + C'_m} = \frac{C'_m}{g_{m1}}$$

$$J_m = \frac{1}{1 + J_{m-1}}$$

$$g_{m1} = g'_m + C'_m \qquad\qquad (2.43)$$

$$g_{m2} = g'_m \cdot (1 + J_{m-1}) = \frac{g'_m}{J_m}$$

$$g_{m+1} = \frac{g'_{m+1}}{(J_{m-1} + 1)^2} = J_m^2 \cdot g'_{m+1}$$

To design the location of the transmission zeros, the following equations are used:

$$\omega_0^2 = \frac{-1}{g'_{m+1} \cdot C'_m} \quad (2.44)$$

Substituting g'_{m+1} and C'_m from (2.40) yields:

$$J_{m-1} = \frac{-J_m^2}{\omega_0'^2 \cdot g_1 \cdot g_{m+1}} \text{ with } (2.40)$$

$$\qquad\qquad\qquad\qquad\qquad (2.45)$$

$$J_{m-1} = \frac{-J_m}{\omega_0'^2 \cdot g_1 \cdot g_{m+1} - J_m^2}$$

41

2.2.3 Low-pass prototype to bandpass transformation [6]

Assume that a low-pass prototype response is to be transformed to a bandpass response, having a passband $\omega_2 - \omega_1$ where ω_1 and ω_2 are the lower and upper passband edges. The required frequency transformation is given by the following equations [6]:

$$\Omega = \frac{\Omega_0}{FBW} \cdot \left(\frac{\omega}{\omega_0} - \frac{\omega_0}{\omega} \right)$$

$$\omega_0 = \sqrt{\omega_1 \cdot \omega_2} \qquad (2.46)$$

$$FBW = \frac{\omega_2 - \omega_1}{\omega_0}$$

where $\omega_2 - \omega_1$ is the pass BW of the filter. In this transformation, the inductive or capacitive elements g in the low-pass prototypes of Section 2.2 will transform to either parallel or series LC resonant circuits in the BPF as shown in Fig. 2.16. The reference impedance is also scaled from the nominal value 1Ω to Z_0:
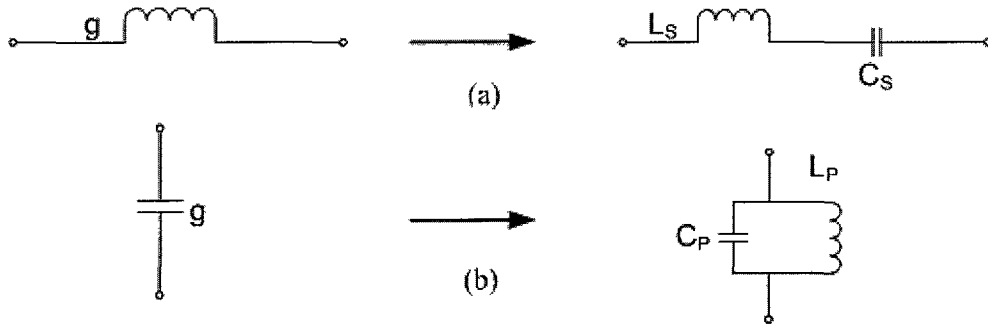
Figure 2-16 Element transformation (a) series LC resonant . (b) parallel LC resonant

The resonant LC elements are given by [6]:

$$C_P = \left(\frac{1}{\text{FBW} \cdot \omega_0 \cdot \Omega_C} \right) \cdot \frac{1}{\gamma_0 \cdot g}$$

$$L_P = \left(\frac{\Omega_C \cdot \text{FBW}}{\omega_0} \right) \cdot \gamma_0 \cdot g$$

$$C_S = \left(\frac{\Omega_C \cdot \text{FBW}}{\omega_0} \right) \cdot \frac{g}{\gamma_0}$$

(2.47)

$$L_S = \left(\frac{1}{\text{FBW} \cdot \omega_0 \cdot \Omega_C} \right) \cdot \frac{\gamma_0}{g}$$

where γ_0 is impedance scaling factor defined as:

$$\gamma_0 = \begin{cases} \dfrac{Z_0}{g_0}, \text{ for } g_0 \text{ being resistance} \\[2mm] \dfrac{g_0}{\gamma_0}, \text{ for } g_0 \text{ being conductance} \end{cases}$$

(2.48)

For the pseudoelliptic prototype low-pass filter, the transformation of the transmission zero frequencies can be calculated as follows [6]:

$$\omega_{a1} = \omega_0 \cdot \frac{-\Omega_a \cdot \text{FBW} + \sqrt{\left(\Omega_a \cdot \text{FBW} \right)^2 + 4}}{2}$$

$$\omega_{a2} = \omega_0 \cdot \frac{\Omega_a \cdot \text{FBW} + \sqrt{\left(\Omega_a \cdot \text{FBW} \right)^2 + 4}}{2}$$

(2.49)

43

2.3 Resonator Theory and Background [6]

2.3.1 Resonator basics

A resonator is a device that can store electrical and magnetic energy. One of its main applications is the realization of BPFs. The basic parallel resonator circuit with coupling is shown in Fig. 2.17:
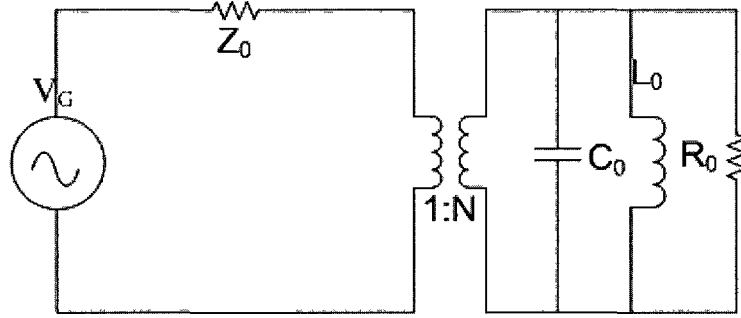
Figure 2-17 Parallel RLC resonant circuit.

The resonator is represented by a parallel *RLC* network resonating at frequency, $\omega_0 = 1/\sqrt{C_0 \cdot L_0}$. Energy is coupled from the generator by the *1:N* transformer. The resistor R_0 represents power loss in the resonator. If the transformer ratio N is unity, the time averaged electrical energy and magnetic energy stored in the capacitor and inductor, respectively, and power dissipated by the network are [6]:

$$W_e = \frac{V_g^2}{4} \cdot \left(\frac{\omega_0^2}{C_0} \right)$$

$$W_m = \frac{V_g^2}{4} \cdot \left(\frac{1}{\omega_0^2 \cdot L_0} \right) \quad (2.50)$$

$$P_{dissipated} = \frac{V_g^2}{2 \cdot R_0}$$

An important parameter of resonator is the quality factor, Q, which specifies the frequency selectivity and performance. It is defined as [6]:

$$Q = \omega \cdot \left(\frac{\text{energy stored per cycle}}{\text{power dissipated}} \right) = \omega \cdot \frac{W}{P} \quad (2.51)$$

When R_0 represents the loss of the resonator only, the Q of (2.48) is called the unloaded quality factor, Q_0. If the resonator is coupled to an external load, this loading will change the total resistance seen by the resonator and the quality factor of the resonant circuit will be reduced. This Q is called the loaded quality factor denoted as Q_L. The external quality factor Q_{ext} is defined as the Q that would result if the resonant circuit was lossless with external loading present. The relationship between the different Q values is [6]:

$$\frac{1}{Q_L} = \frac{1}{Q_{ext}} + \frac{1}{Q_0} \quad (2.52)$$
$$= \frac{Q_0}{1+k}$$

where k is the coupling factor to the resonator.

2.3.2 Half wavelength microstrip resonators

A microstrip transmission line is a conducting line of width w on top of an insulating substrate of thickness h with ground plane. The substrate has a relative dielectric constant of ε_r. The characteristic impedance Z_0 of the microstrip line is given by [6]:

$$Z_0 = \begin{cases} \dfrac{\eta_0}{2 \cdot \pi} \cdot \ln\left(\dfrac{8 \cdot h}{W'} + \dfrac{W'}{4 \cdot h}\right) & , \dfrac{W}{h} \leq 1 \\[4mm] \dfrac{\eta_0}{\sqrt{\varepsilon_{eff}}} \left[\dfrac{W'}{h} + 1.393 + 0.667 \times \ln\left(\dfrac{W'}{h} + 1.44\right)\right]^{-1} & , \dfrac{W}{h} \geq 1; \end{cases}$$

where:

$$\eta_0 = 120 \cdot \pi \; \Omega \qquad\qquad (2.53)$$

$$\frac{W'}{h} = \begin{cases} \dfrac{W}{h} + \dfrac{1.25}{\pi} \cdot \dfrac{t}{h}\left(1 + \ln\dfrac{4 \cdot \pi \cdot W}{t}\right), & \dfrac{W}{h} \leq 1 \\[4mm] \dfrac{W}{h} + \dfrac{1.25}{\pi} \cdot \dfrac{t}{h}\left(1 + \ln\dfrac{2 \cdot h}{t}\right) & , \dfrac{W}{h} \geq 1 \end{cases}$$

The wavelength λ_g in the microstrip line at frequency f_o is given by

$$\lambda_g = \frac{\lambda_o}{\sqrt{\varepsilon_{eff}}} = \frac{c}{f_0\sqrt{\varepsilon_{eff}}} \qquad (2.54)$$

where c is the speed of light in free space and λ_o is the wavelength in free space. Instead of using ε_r in Eqn. (2.55) the effective relative dielectric constant of the substrate for the microstrip line, ε_{eff}, is used. It takes into account the mixed air/substrate dielectric system. It is given by [6]

$$\varepsilon_{eff} = \begin{cases} \dfrac{1}{2} \cdot (\varepsilon_r + 1) + \dfrac{1}{2} \cdot (\varepsilon_r - 1) \cdot \left[\sqrt{1 + 12 \cdot \dfrac{h}{w}} + 0.04 \cdot \left(1 - \dfrac{w}{h}\right)^2\right], & \text{for } \dfrac{w}{h} \leq 1 \\[4mm] \dfrac{1}{2} \cdot (\varepsilon_r + 1) + \dfrac{1}{2} \cdot (\varepsilon_r - 1) \cdot \sqrt{1 + 12 \cdot \dfrac{h}{w}} & , \text{for } \dfrac{w}{h} \leq 1 \end{cases} \qquad (2.55)$$

Material losses of microstrip transmission line are as follows [6]

$$\alpha_d = \frac{\left(\dfrac{2\pi \cdot f_c}{C}\right) \cdot \varepsilon_r \cdot \left(\varepsilon_{eff} - 1\right)\tan\delta}{2 \cdot \sqrt{\varepsilon_{eff}} \cdot \left(\varepsilon_r - 1\right)} \quad \left[Np/m\right] \quad (2.56)$$

and $\quad \alpha_c = \dfrac{\sqrt{2 \cdot \pi \cdot f_c \cdot \mu_0 / 2 \cdot \sigma}}{W \cdot Z_0} \quad \left[Np/m\right] \quad (2.57)$

A half wavelength resonator is an open circuited microstrip line of nominal length $\lambda_g/2$. Due to the electrical field extending beyond the ends of the microstrip line, there is some parasitic fringing capacitance C_f at both ends of the resonator line. The equivalent circuit of a planar half wavelength resonator is shown in Fig. 2.18:
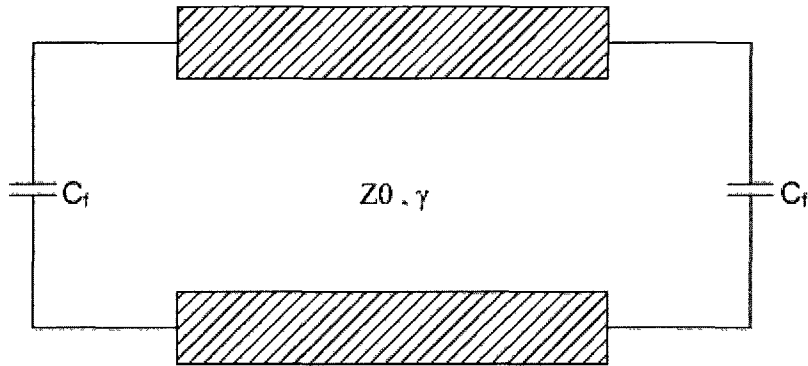
Figure 2-18 Equivalents circuit of half wavelength resonator

The fringing capacitance makes the structure appear electrically smaller by length Δd given by [6]:

$$\Delta d = 0.412 \cdot h \cdot \left(\frac{\varepsilon_{eff} + 0.3}{\varepsilon_{eff} - 0.258}\right) \cdot \left(\frac{w/h + 0.262}{w/h + 0.813}\right) \quad (2.58)$$

The microstrip line will then resonate in the fundamental mode when:

$$d + 2 \cdot \Delta d = \lambda_g / 2 \quad (2.59)$$

47

Generally, there are three methods to couple a microstrip line to a microstrip resonator. These are end-coupling, parallel line coupling, and direct tap coupling. The latter two are of interest here and are shown in Fig. 2.19.
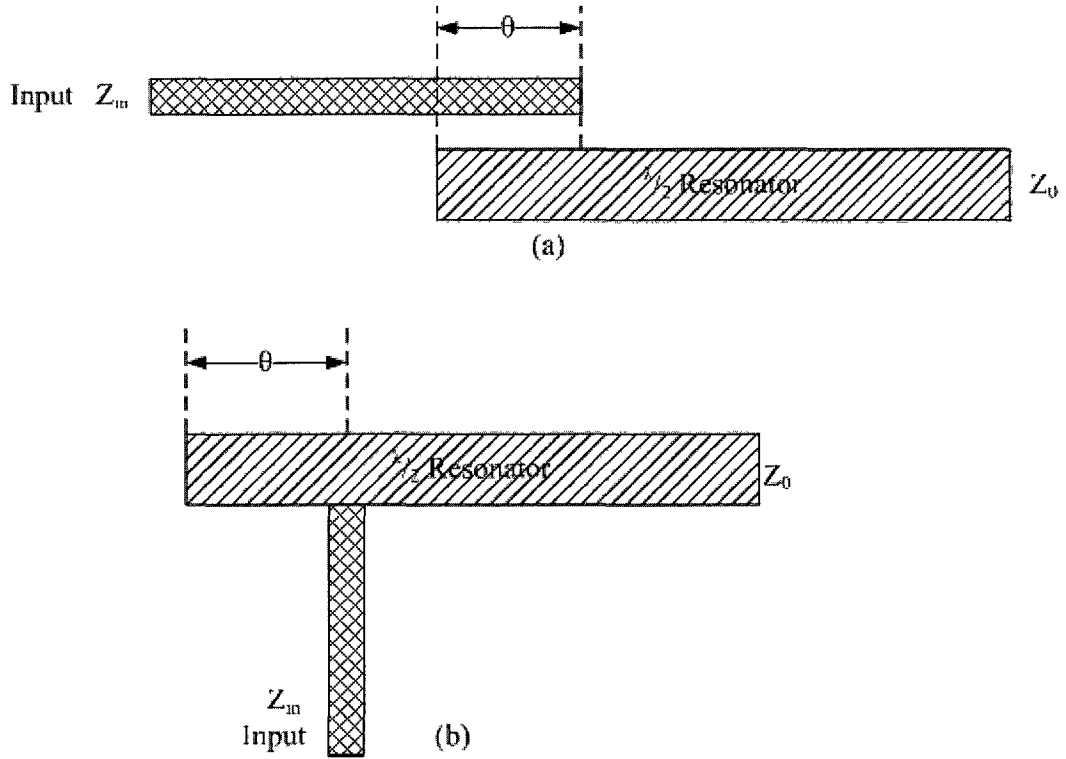
Figure 2-19   Coupling mechanisms. (a) coupled-line and (b) direct tap coupled

The coupling coefficient β, is defined as [6]

$$\beta = \begin{cases} \dfrac{k^2}{\sinh\left(\pi/_2 \cdot Q_0\right)} \cdot \dfrac{2 \cdot \theta}{\pi}, k \propto \text{spacing, Parallel coupled line mechanism} \\[4mm] \dfrac{Z_0}{Z} \cdot \dfrac{2 \cdot Q_0}{\pi} \cdot \cos^2 \theta, \text{Tap coupled mechanism} \end{cases} \qquad (2.60)$$

The formulas for these coupling mechanisms are:

parallel coupled line $\qquad \sinh\left(\dfrac{\pi}{2 \cdot Q_0}\right) = \dfrac{k^2}{\beta \cdot \dfrac{\pi}{2 \cdot \theta}}$

$$\text{direct tape} \qquad \frac{Q_0}{\pi} = \frac{\dfrac{\beta}{2} \cdot \left(\dfrac{Z_{in}}{Z_0}\right)}{\cos^2 \theta} \qquad (2.61)$$

where Z_{in} is the input impedance seen by the coupling line.

2.3.3 Rectangular cavity resonators (air filled)

A rectangular cavity with height H, width W and length L can be considered as a portion of a rectangular waveguide as shown in Fig. 2.20. The waveguide can propagate in the TE_{mn} mode or TM_{mn} mode, where the subscripts m and n refer to the number of half-sinusoid variations along the x and y directions, respectively. To make a resonant cavity, the waveguide is terminated by short circuits at $z=0$ and $z=L$. If the length of the rectangular waveguide equals a multiple of half of the guided wavelength for a particular mode TE_{mnp} or TM_{mnp} at frequency, f_r, the resultant standing-wave pattern is such that the x and y components of electric field are zero at $z = 0$ and $z=L$. The third subscript p refers to the number of half- cycles along the z direction:
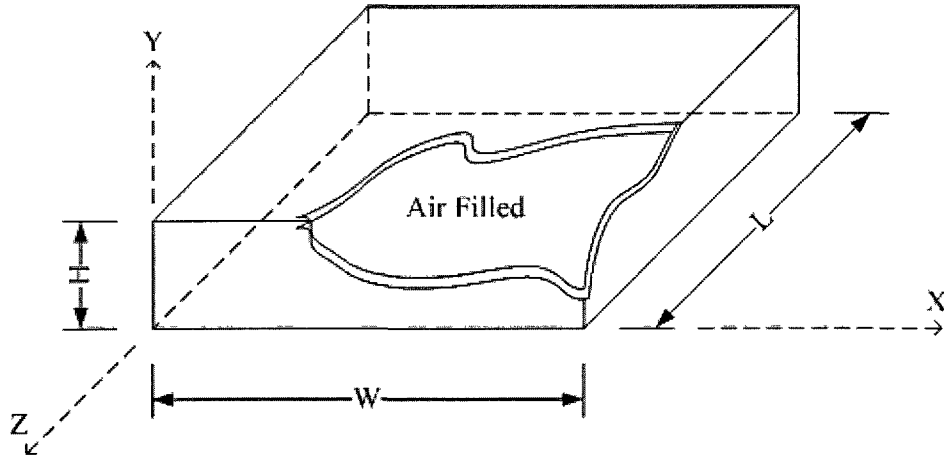
Figure 2-20 Rectangular cavity resonator

The general resonant frequency for the TE_{nmp} mode is given by:

$$f_{TE,nmp} = \frac{c}{2} \cdot \sqrt{\left(\frac{m}{W}\right)^2 + \left(\frac{n}{H}\right)^2 + \left(\frac{p}{L}\right)^2} \quad (2.62)$$

The resonant frequency for the TE_{101} mode is given by

$$f_{r,101} = \frac{c}{2} \cdot \sqrt{\left(\frac{1}{W}\right)^2 + \left(\frac{1}{L}\right)^2} \quad (2.63)$$

The cutoff wavelength and guide wavelength for the TE_{10} mode are

$$\lambda_c = 2W$$

$$\lambda_g = \frac{\lambda_0}{\sqrt{1-\left(\dfrac{\lambda_0}{2W}\right)^2}} \qquad (2.64)$$

For an arbitrary mode, the cavity is resonant when:

$$L = \frac{\lambda_g}{2} \cdot p$$

where: $\lambda_g = \dfrac{\lambda_0}{\sqrt{1-\left(\dfrac{\lambda_0}{\lambda_{c,mn}}\right)^2}}$ \qquad (2.65)

$$\lambda_{c,mn} = \frac{2}{\sqrt{\left(\dfrac{m}{W}\right)^2 + \left(\dfrac{n}{H}\right)^2}}$$

λ_0 is free space wavelength, λ_g is the guided wavelength, and $\lambda_{c,mn}$ is the cut-off

wavelength of certain mode of operation. And the mode mnp pertain to the number of

half-sinusoid variations in the standing-wave pattern along the x, y and z axis respectively.

Base on [9] Q_0 can be calculated as follow:

$$Q_{0,TE_{mnp}} = \frac{A}{B+C+D} \qquad (2.66)$$

where: $A = \dfrac{\pi \cdot Z_W}{R_S} \cdot \dfrac{L \cdot W \cdot H}{4} \left[\left(\dfrac{m}{W}\right)^2 + \left(\dfrac{n}{H}\right)^2 \right] \cdot \left[\left(\dfrac{m}{W}\right)^2 + \left(\dfrac{n}{H}\right)^2 + \left(\dfrac{p}{L}\right)^2 \right]^{\frac{3}{2}}$

$$B = \zeta \cdot W \cdot H \cdot \left[\left(\dfrac{m}{W} \cdot \dfrac{p}{L}\right)^2 + \left(\left(\dfrac{m}{W}\right)^2 + \left(\dfrac{n}{H}\right)^2\right)^2 \right]$$

$$C = \eta\ L\ H\ \left[\left(\frac{n}{H}\ \frac{p}{L} \right)^2 + \left(\left(\frac{m}{W} \right)^2 + \left(\frac{n}{H} \right)^2 \right)^2 \right]$$

$$D = W\ H\ \left(\frac{p}{L} \right)^2 \left[\left(\frac{m}{W} \right)^2 + \left(\frac{n}{H} \right)^2 \right] \qquad \text{and}$$

$$\xi = \begin{cases} 1, \text{if } n \neq 0 \\ \dfrac{1}{2}, \text{if } n = 0 \end{cases}, \quad \eta = \begin{cases} 1, \text{if } m \neq 0 \\ \dfrac{1}{2}, \text{if } m = 0 \end{cases} \quad \text{and } Z_w = \sqrt{\frac{\mu}{\varepsilon}} = 377.7\Omega \text{ is the free space impedance.}$$

Also:

$$Q_{0,TM_{nmp}} = \frac{\dfrac{\pi\ Z_w}{R_S}\ \dfrac{L\ W\ H}{4} \left[\left(\frac{m}{W} \right)^2 + \left(\frac{n}{H} \right)^2 \right] \left[\left(\frac{m}{W} \right)^2 + \left(\frac{n}{H} \right)^2 + \left(\frac{p}{L} \right)^2 \right]^{\frac{3}{2}}}{H \left(\frac{m}{W} \right)^2 (\gamma\ W\ L) + W \left(\frac{n}{H} \right)^2 (\gamma\ H\ L)} \quad (2.67)$$

Where $\gamma = \begin{cases} 1, \text{if } p \neq 0 \\ \dfrac{1}{2}, \text{if } p = 0 \end{cases}$

For TE_{101} mode resonators, Equations (2.66~2.67) simplify to:

$$Q_0 = \frac{\pi \cdot Z_w}{R_s} \left[\frac{2H(W^2 + L^2)^{\frac{3}{2}}}{WL(W^2 + L^2) + 2H(W^3 + H^3)} \right] \quad (2.68)$$

where R_S is the surface resistance of the conducting walls

$$R_S = \sqrt{\frac{\pi f \mu_0}{\sigma}} \quad (2.69)$$

52

Chapter 3   Planar BPF Design with Open-Loop-Resonators

In pursuit of the second thesis objective, this chapter presents two cross-coupled planar microwave BPF designs based on half wavelength open loop resonators. These structures occupy a smaller area, since a $\frac{\lambda_g}{2}$ resonator is arranged to form an open-loop structure and both magnetic and electrical coupling and cross coupling can be realized. [12] The essential mixed mode coupling property is applied in the designs of pseudo-elliptic BPFs chosen here. Excellent stop-band rejection is achieved because of the pseudo-elliptic response. However, small FBW is expected due to weak coupling and limited resonator Q, and weak coupling is sensitive and hard to control. These BPFs are designed with RT/ Duroid © 5880 substrate and 99.6 % alumina (Al_2O_3) substrates which are very popular due to their low loss at microwave frequencies. Duroid 5880 has a loss tangent ($\tan \delta$) of 0.0009 [10] while the alumina substrate exhibits a $\tan \delta$ of around 0.0002 [11]. Both of these substrates are relatively inexpensive. However, the biggest drawback of these two materials is they are not capable of multilayer processing. Most Duroid substrates have large z-direction thermal expansion coefficient. As a result, multilayer substrates are difficult to laminate and any added metallization layers will suffer from surface roughness due to heating. Multilayer alumina substrates are also not possible since the 99.6% pure alumina is very hard and brittle, and as a result, it is not possible to drill or laser micro-vias through the substrate.

The following section will describe in detail the theory and design procedures for two open-loop resonator BPFs using four and six pole configurations implemented with alumina and Duroid 5880 substrates. Increasing the order of the BPFs will enable higher stop band rejection but degrade the filter's insertion loss, thus making them unsuitable for point-to-point microwave radio application (Section 2.1). With combination of MMIC active devices and phase shifters, the insertion loss of a higher order BPF could be

overcome [13]. This solution requires at least two more active gain components and precise phase offsets, which at microwave frequencies increases system costs.

3.1   Theory and Coupling Structure of Open-Loop Resonators [12]

Open-loop resonators are widely used in MMIC and MIC system. [28] The basic idea is to bend a linear $\dfrac{\lambda_g}{2}$ resonator into a square shape with an opening at one of its sides, as shown in Fig. 3.21. The square shape is smaller in size than the linear resonator and also allows for cross-coupling:

(a)   (b)
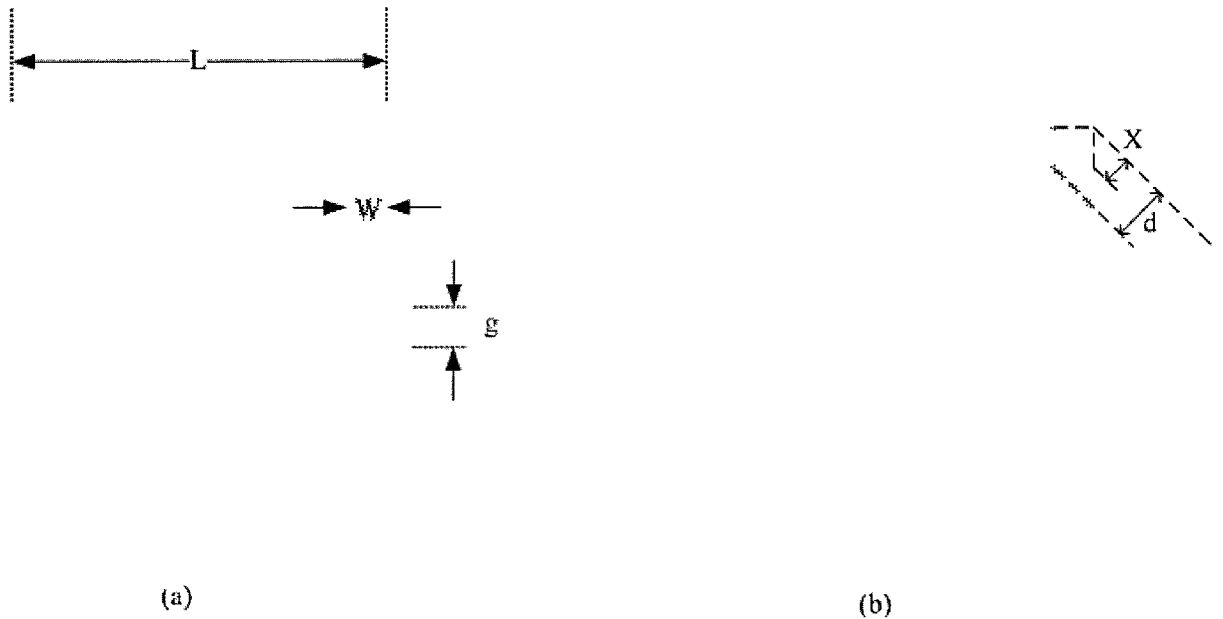
Figure 3-21 $\dfrac{\lambda_g}{2}$ open-loop resonator (a) regular chamfer (b) optimal mitered

Implementation issues occur if the width, W of a 50 . microstrip line is too wide relative to the circumference and side length, L, of the open-loop-resonator. A higher impedance resonator may be designed in order to reduce W but an additional impedance transformer will be required at the feed point as shown later in Fig.3-37.

Three different types of coupling can be realized with this open-loop-resonator structure. When the resonator is excited, there is a strong electrical field in the gap, *g,* of the resonator, where an open circuit condition exists. If two open-loop-resonators are oriented with their gaps in close proximity, coupling between the resonators is formed due to the strong electrical fringe fields. This type of coupling, illustrated in Fig. 3.22(a) is called electrical coupling. The strongest magnetic field density appears at the short circuit located directly opposite the gap if the gap is at the midpoint of the resonator. If two open-loop-resonators are oriented with the edges containing the short circuit in close proximity, coupling between the resonators is formed due to the strong magnetic fields. This type of coupling, illustrated in Fig. 3.22(b) is called magnetic coupling. The third and last possible placement of the resonators shown in Fig 3.22(c), produces so called mixed coupling, with both electrical and magnetic fringe fields at the closely aligned sides. Because both the electrical and magnetic fringe fields exhibit exponentially decaying amplitude away from the microstrip line, the amount of coupling between resonators (strong or weak) can be controlled by the displacement, *S* and offset *O*, of the resonators.

S
⟵⟶

⊥
o
⌐

(a)

S
⟵⟶

⊥
o
⌐

(b)

S
⟵⟶

⊥
o
⌐

(c)

Figure 3-22 Basic coupling structure of coupled open-loop resonators. (a) electrical coupling (b) magnetic coupling (c) mixed coupling

Based on [12] once the coupling between resonators is formed, or the corresponding coupling coefficient is larger than a critical value (the reciprocal of the resonator's loaded Q), there will be two resonant peaks associated with the mode splitting. Mode splitting can be identified with a full-wave electromagnetic simulator. These two peak frequencies are related by the coupling coefficient between the resonators. The following presents the formulation of such a relationship for the coupling structure in Fig.3-22.

(a) Electrical coupling: [12]

An equivalent lumped-element circuit model for the electrical coupling structure shown in Fig. 3.22(a) is given in Fig. 3.23(a) where L and C correspond to the self-inductance and self-capacitance, respectively, and C_m represents the mutual capacitance due to coupling. The electrical coupling can be represented by an admittance inverter $J = \omega \cdot C_m$ where   is angular resonant frequency of the uncoupled resonator:

$$\omega = \frac{1}{\sqrt{C \cdot L}} \quad (3.1)$$

If this circuit is symmetrical about an electrical wall, i.e. a short-circuit, the resonant frequency due to this is

$$f_e = \frac{1}{2 \cdot \pi \cdot \sqrt{L \cdot (C + C_m)}} \quad (3.2)$$

Similarly, if this circuit is symmetrical about a magnetic wall or an open circuit, the corresponding resonant frequency is:

$$f_m = \frac{1}{2 \cdot \pi \cdot \sqrt{L \cdot (C - C_m)}} \quad (3.3)$$

The overall electrical coupling factor k_E is:

$$k_E = \frac{f_m^2 - f_e^2}{f_m^2 + f_e^2} \quad (3.4)$$

This is also equal to $\dfrac{C_m}{C}$ identical to the definition of the ratio of the coupled electrical energy to the stored electrical energy stored in the uncoupled resonator.

(b) Magnetic coupling: [12]

57

An equivalent lumped-element circuit model for the magnetic coupling structure in Fig. 3.22(b) is shown in Fig. 3.23(b) where L and C correspond to the self-inductance and self-capacitance, respectively, and L_m represents the mutual inductance due to coupling. Based on the aforementioned analysis the circuit has resonant frequency due to electrical symmetric wall:

$$f_e = \frac{1}{2 \cdot \pi \cdot \sqrt{C \cdot (L - L_m)}} \quad (3.5)$$

and magnetic symmetrical wall:

$$f_m = \frac{1}{2 \cdot \pi \cdot \sqrt{C \cdot (L + L_m)}} \quad (3.6)$$

Similarly, the resultant magnetic coupling coefficient is:

$$k_E = \frac{f_e^2 - f_m^2}{f_e^2 + f_m^2} = \frac{L_m}{L} \quad (3.7)$$

(c) Mixed coupling: [12]

An equivalent lumped-element circuit model for coupling structure in Fig. 3.22(c) is shown in Fig. 3.23(c). In this structure both electrical and magnetic couplings are present. Therefore both mutual inductance L'_m and mutual capacitance C'_m are in the equivalent circuit model. By inserting an electrical and magnetic wall, or symmetry plane, the two mode frequencies can be obtained as:

$$f_e = \frac{1}{2 \cdot \pi \cdot \sqrt{(L - L'_m) \cdot (C - C'_m)}}$$

$$f_m = \frac{1}{2 \cdot \pi \cdot \sqrt{(L + L'_m) \cdot (C + C'_m)}} \quad (3.8)$$

and the coupling coefficient of mixed coupling is:

$$k_B = \frac{f_e^2 - f_m^2}{f_e^2 + f_m^2}$$

$$= \frac{C \cdot L'_m + L \cdot C'_m}{C \cdot L + L'_m \cdot C'_m} \quad (3.9)$$

Assuming mutual inductance and capacitance is smaller than their self-capacitance and inductance, then $L'_m \cdot C'_m << L \cdot C$ and (3.8) becomes:

$$k_B \approx \frac{L'_m}{L} + \frac{C'_m}{C} \quad (3.9)$$

$$= k'_M + k'_E$$

Full EM simulators such as ADS momentum or Ansoft HFSS are used to determine the mode frequencies f_e and f_m for each structure for different values of O and S. Then Eqns. (3.4), (3.7) and (3.9) can be used to calculate the corresponding coupling coefficient. Since more detailed information about the specific structures that were simulated must still be given, the results for the extracted coupling coefficient will be presented, along with the design of the two BPF, in Section 3.2 and Section 3.3. Some general observations from the results can be summarized here
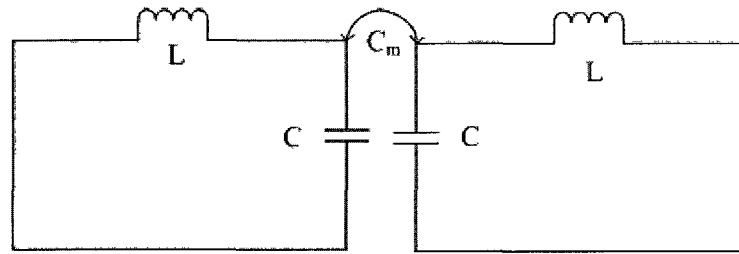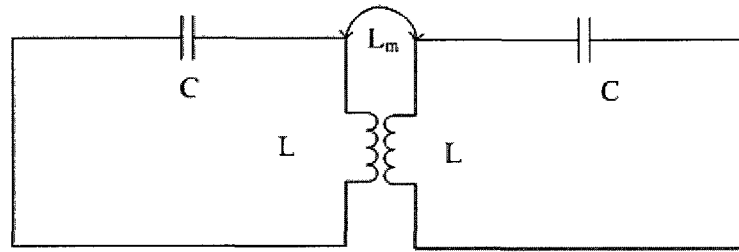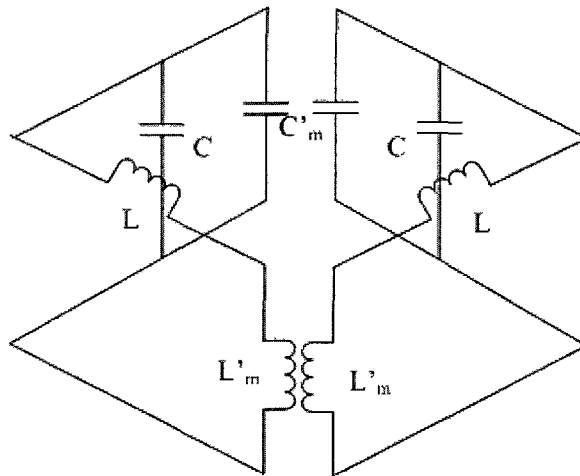
Figure 3-23 Equivalent circuit models for coupling structure of coupled open-loop

resonators. (a) electrical coupling (b) magnetic coupling (c) mixed coupling

Some general trends for the coupling coefficient that were observed here as well as in [12] are:

- The spacing S (shown in Fig.3-22.) decreases the resonate peak frequencies move towards each other, this implies stronger coupling between resonators.

- The electrical coupling, k_E and mix coupling k_B shows a dependence of dielectric constant. The lower the dielectric constant the stronger the k_E and k_B are.

- Magnetic coupling k_M is independence of dielectric constant.

- Width of the resonator's arm W,(shown in Fig.3-21.)is inverse proportional to the amount of coupling.

- Length of the resonator's arm L, (shown in Fig.3-21.)is proportional to the amount of coupling.

- Electrical coupling is more sensitive to the offset distance O, (shown in Fig.3-22.) than the magnetic and mix coupling.

3.2 Case Example: K-band BPF Design with 99.6% Alumina

With reference to the system block diagram of Chapter 2, a K-band (13.75 GHz) bandpass filter is required as part of the LO line-up in the radio transceiver. Such filtering in the LO chain will eliminate any spurious signal from entering the highly non-linear frequency multiplier and other active MMIC devices, thus reducing spurious levels at the LO port of the mixer.

In this section, a K band BPF is designed based on 99.6% alumina substrate ($\varepsilon_r = 9.9$, $\tan \delta = 0.0002$). Due to the high dielectric constant of alumina, the size of the circuit is small and the width associated with 50Ω microstrip feed line is relatively large

compared to the quarter guided wavelength. For example at 60 GHz, and using Eq. (2.57), the effective dielectric constant ε_{eff} of a 5 mil, 127 μm thickness substrate is 6.81. The width of a 50Ω microstrip line will be 4.7mil or 120 μm by Eq.(2.53). and from Eq. (2.54) the half guided wavelength $\lambda_g/2$ is 0.947 mm. The circumference of the square resonator would be about $\lambda_g/8\sim0.24$ mm which is only 2W. Because of geometrical limits, the open-loop structure cannot be made at V-band. However at lower frequency bands such as K-band, the BPF can be designed using this structure.

3.2.1 Specifications and calculations

In this design a K band (13.75 GHz) 4th orders BPF is designed. The pass bandwidth of this filter is 500 MHz with a fractional bandwidth (FBW) of $\dfrac{500\,\text{MHz}}{13.7\,\text{GHz}} = 3.65\%$. A pair of transmission zeros is placed 1 GHz away from centre frequency. The target passband ripple is 0.1 dB, corresponding to a return loss of better than -16 dB. Using equations (2.37 – 2.40) the following pseudo-elliptic low pass prototype parameters are calculated:

Table. 8: Pseudo-elliptic low pass prototype parameters

g_0	1
g_1	1.11
g_2	1.31
J_1	-0.03
J_2	0.88

According to [6] the frequency transformation, mutual coupling coefficients and both equivalent input and output quality factors Q_{ei}, Q_{eo} can be calculated as follows:

$$Q_{ei} = Q_{eo} = \frac{g_1}{\text{FBW}}$$

$$M_{1,1+1} = M_{n-i,n-i+1} = \frac{\text{FBW}}{\sqrt{g_i \cdot g_{i+1}}} \text{ , for } i = 1 \text{ to } m-1$$

Where n = filter order; $m = \frac{n}{2}$ $\qquad$ (3.12)

$$M_{m,m+1} = \frac{\text{FBW} \cdot J_m}{g_m}$$

$$M_{m-1,m+2} = \frac{\text{FBW} \cdot J_{m-1}}{g_{m-1}}$$

Rest indices $= 0$

where $M_{m,n}$ is the coupling matrix index between the resonators. From (3.12) the coupling matrix of the 4$^\text{th}$ order is as follows:

$$\vec{M} = \begin{bmatrix} 0 & 0.0297 & 0 & -0.001 \\ 0.0297 & 0 & 0.0241 & 0 \\ 0 & 0.0214 & 0 & 0.0297 \\ -0.001 & 0 & 0.0297 & 0 \end{bmatrix} (3.13)$$

Noticing that $M_{1,4} = M_{4,1}$ is negative, this is due to the fact that the electrical coupling defined as equivalent circuits in the previous section are in opposite phase. This negative coupling is essential to realize cross-coupled filters having a pseudo-elliptical response.

3.2.2 Design and calculations

The substrate properties are provided by Ultrasource [29]. The material properties and machine tolerances are summarized in the following table:

Table 9: Properties and tolerance of alumina substrate

ε_r	9.90
$\tan \delta$	0.0002
Substrate thickness, h	5 mil
Metalization, Gold	0.1 mil
Surface roughness	2μ inch
Track tolerance	$\pm \dfrac{1}{5}$ mil
Pull back	2 mil

From (3.10) the corresponding width of a 50Ω microstrip line using 2.54μm thick gold tracks is 4.71 mil or 120 μm. The width of the resonator, W is set to be same width of 50Ω microstrip line. Using (2.53) $\lambda_g/2$ can be calculated as 167.63 mil at 13.75 GHz. The side of the resonator, L is set to be 45 mil, resulting the gap, g of the open end of the resonator to be 12.37 mil, shown as Fig.3-21(a).

The 90^0 chamfer of the resonator is designed to be optimally mitered shown as Fig.3-24. This bend optimizes conductor loss and impedance transformation at this discontinuous. The following empirical formula is used to calculate the optimally mitered 90^0 chamfer [14].
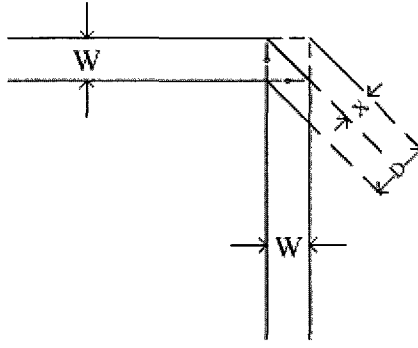
Figure 3-24 Optimal mitered 90^0 bend.

The usable ranges of this empirical formula are:

$$0.5 \leq \frac{W}{h} \leq 2.75$$

$$2.5 \leq \varepsilon_r \leq 25 \qquad (3.14)$$

$$\text{simulation frequency} \leq \frac{15}{h[mm]}$$

After verifying the above conditions with (3.14), this design uses a

$$\frac{W}{h} = \frac{4.71}{5} = 0.94, \varepsilon_r = 9.9 \text{ and simulation frequency} \leq \frac{15}{0.127\,mm} = 117.11\,GHz .$$
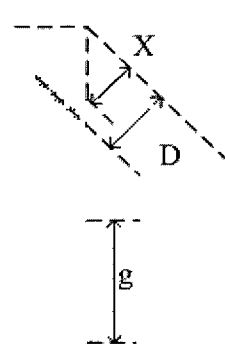
With the empirical formula, the optimal mitered dimensions can be calculated as:

$$\frac{X}{D} = 0.52 + 0.65 \times e^{-1.35 \times \frac{W}{h}} \quad (3.15)$$

The $\frac{W}{D}$ ratio is $\frac{W}{D} = 0.702$, D here can be set as $\sqrt{2 \times W^2} = 6.66$ mil and therefore X

corresponds to $X = 0.702 \times D = 0.702 \times 6.66 = 4.68$ mil .

To include the length of the chamfered corners, the length of each side of the resonator was adjusted from the initial value of 45 mils to 40 mils. After some tuning, the final dimensions of the single-loop resonator are shown in Fig. 3.25.

Table 10: Final dimensions of the resonator after optimization

L	40 mil
W	4.71 mil
X	5.0 mil
D	6.67 mil
g	16.77 mil
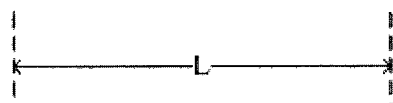
Figure 3-25 Optimal mitered resonator

OpenLoopResonatorResposes
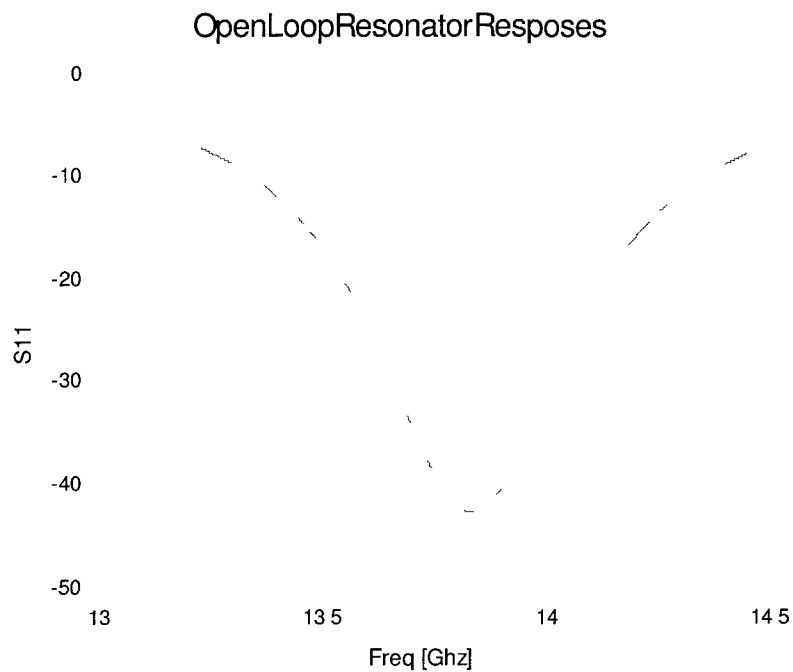
Figure 3-26 Responses of open-loop resonator

Initially, L is set to 45 mils based on the designed optimal mitered chamfer. However the 90^0 bends have finite electrical length, therefore the length of the resonators needs to be shortened. After EM optimization, the final dimensions are summarized in Table.10.

Figure 3-26 shows the reflection of a resonator loaded with a tapped microstrip line as shown in Fig.3-27. It indicates that the designed resonator resonates at 13.75 GHz.

3.2.3 Pseudo-elliptic K-band BPF design with 99.6 alumina

The design target here is to simulate and measure the coupling coefficients of the four resonators designed in Section 3.2.2. One pair of transmission zeros is realized with electrical coupling between the first and the fourth resonator as an alternative route to realizing cross coupling. The input and output is done by direct tapping with 50Ω microstrip line, as discussed in section 2.3.2. The amount of coupling can be extracted with equation (2.57). Note that, the four resonators in the BPF circuit are not identical. The gaps g of the resonators can be varied independently for fine tuning. In particular, the estimated length of the output and input resonators can be used to fine tune the position of the lower and higher resonating points. According to [15] the total length of the input/output resonators can be used to control the steep roll-off on both high and low sides of the BPF.

A feed offset was introduced at both the input and output port to control the FBW of the filter (Fig. 3-27), as discussed with (3.12). The following Figure shows the schematic of the 4 pole BPF including all design variables.

Feed offset | Input
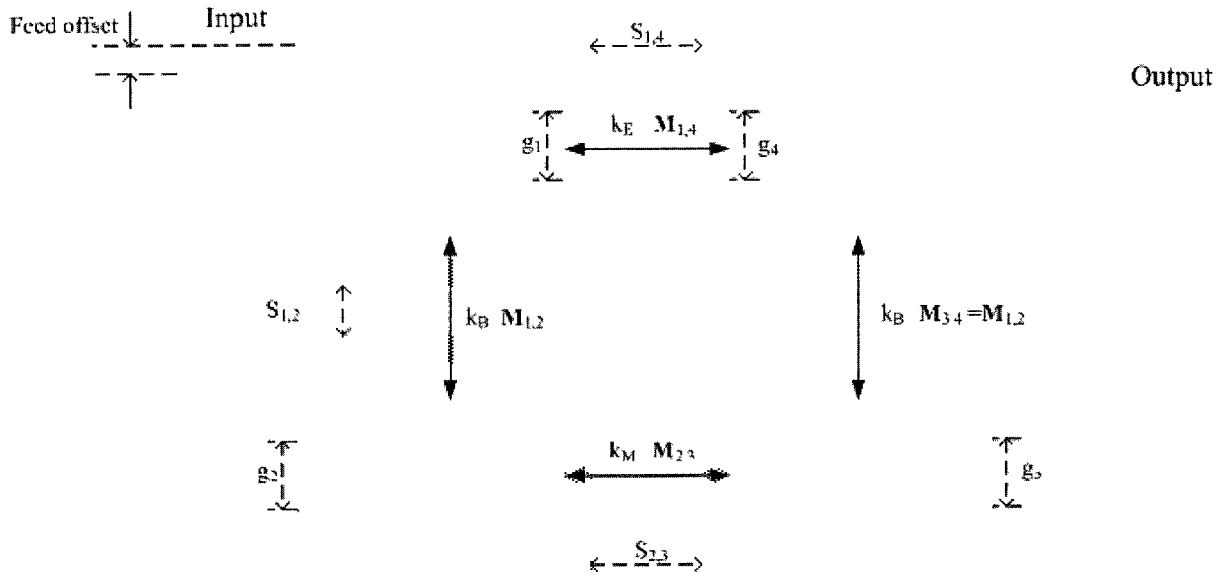
Figure 3-27 Schematics of the four poles BPF

Both couplings from 1st to 2nd resonators, and 3rd to last resonators, correspond to mixed coupling , e.g. values $M_{1,2} = M_{3,4}$ in the coupling matrix $\bar{M}$ (3.13). The amount of coupling is controlled by the spacing $S_{1,2}$ between them as discussed in Section 3.2 and shown in the above figure. The coupling between the input and output resonators corresponds to weak electrical coupling, providing an alternative signal path and the amount of electrical coupling controls the frequency of the transmission zero. Lastly there is magnetic coupling between the 2nd and 3rd resonators.

The resonant mode frequencies for mixed coupling of the coupled structure shown in Fig. 3.22(c) with different spacings S (with zero offset) are obtained from full wave simulation.   The simulation results are shown in Fig. 3.28 for three different $S=2, 5, 10\ mil$. Using Eqn. (3.9) the calculated mixed coupling coefficient k_B variation with the spacings S is presented in Fig. 3.29. From this Figure the required coupling $k_B = M_{1,2} = M_{3,4} = 0.0297$ can be realized with 7.5 mil spacing between 1st and 2nd resonators and also 3rd and 4th resonators as shown in Fig. 3.27.

Again, full wave simulation of the electrically coupled structure shown in Fig. 3.22(a) is used to obtain mode frequencies for various S (with zero offset). The simulation results are shown in Fig. 3.22 for three different spacings $S=2, 11, 17\ mil$. Using Eqn. (3.4) the calculated electrical coupling coefficient k_E variation with the spacings S is presented in Fig. 3.23
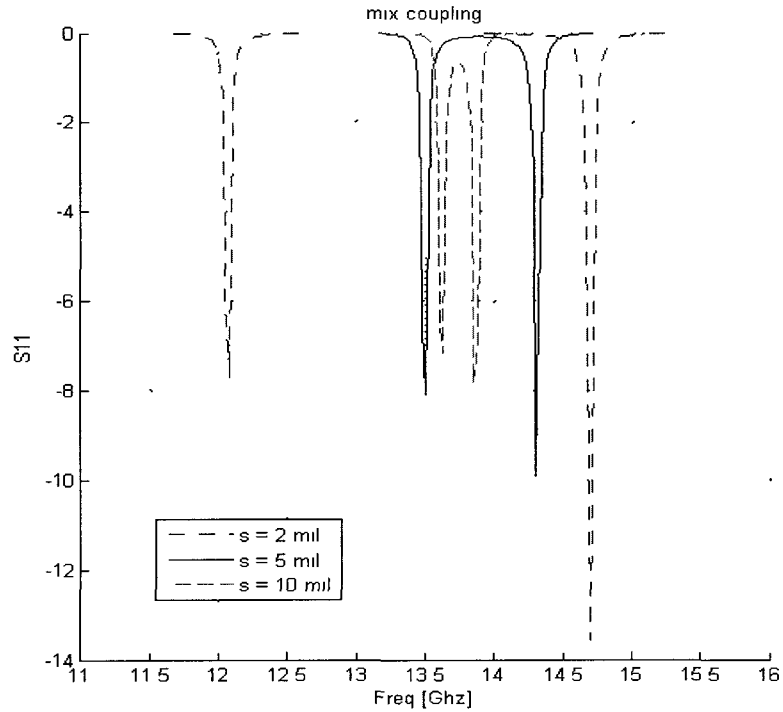
Figure 3-28 Mix coupling responses

With equation (3.8) the corresponding coupling coefficient versus spacings is summarized with the following figure.

69

MixCouplingCoefficient VS spacing
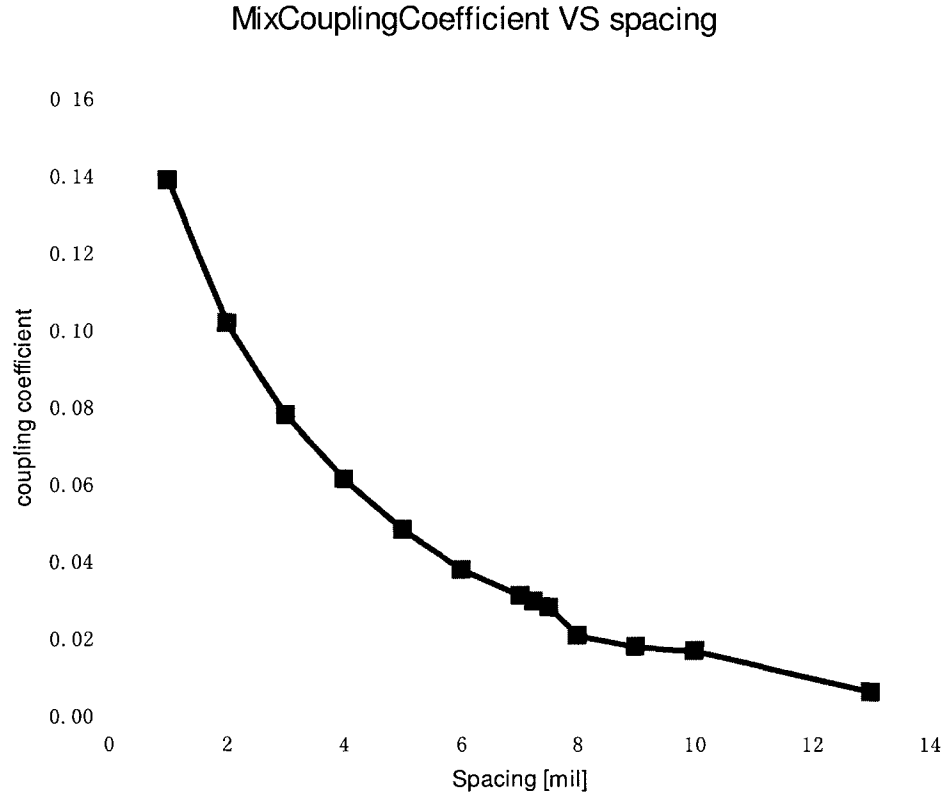
Figure 3-29 Extracted mixed coupling coefficients versus spacing between resonators

The magnetic coupling between the 2nd and 3rd resonators can be found in a similar way. Based on full wave simulators, the resonant mode frequencies for the magnetically coupled structure shown in Fig. 3.22(b) for different spacing s (with zero offset) are obtained. The simulation results are shown in Fig. 3.30 for three different spacings $S=2,5,10$ mil. Using Eqn. (3.9) the calculated variation in the magnetic coupling coefficient k_M as a function of the spacing s is presented in Fig. 3.31. One can see that for spacing less than 10 mils magnetic coupling is larger than mixed coupling. For larger spacing the relationship is less clear due to having insufficient data points. From this Figure the required coupling $k_M = M_{2,3} = 0.0241$ can be realized using a 11.5 mil spacing between 2nd and 3rd resonators as shown in Fig. 3.27

.

70
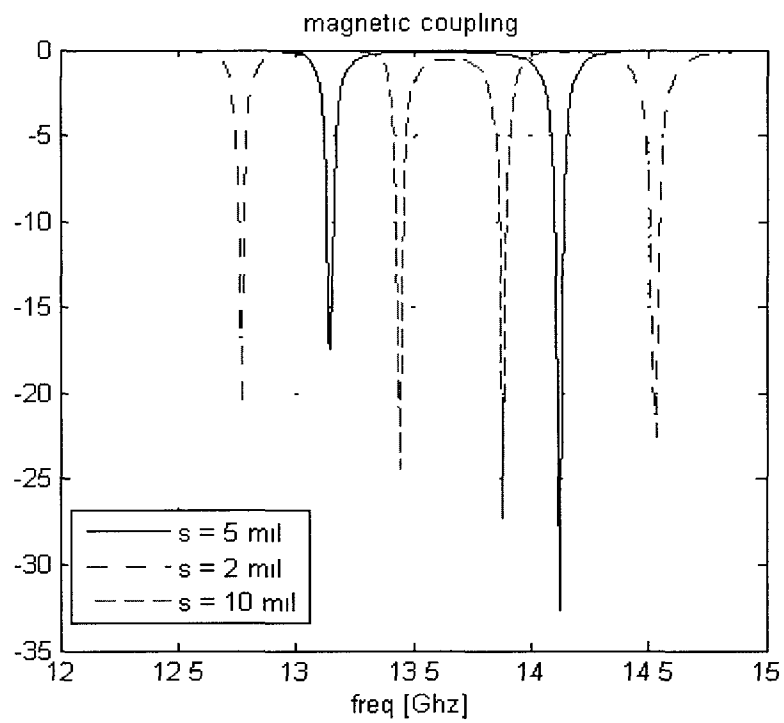
Figure 3-30 Magnetic coupling responses

With equation (3.6) the corresponding coupling coefficient versus spacings is summarized with Fig.3-31.
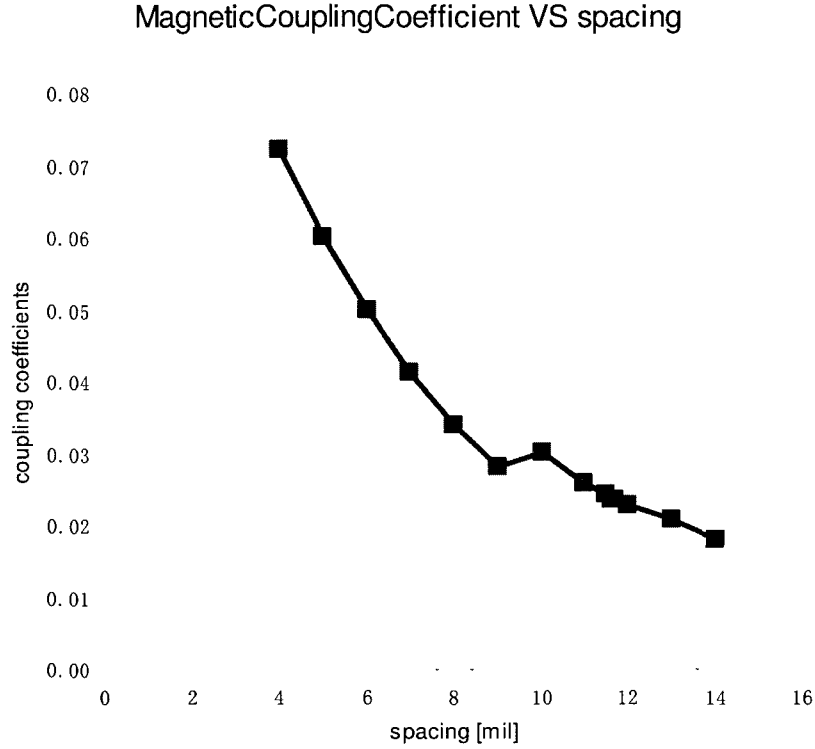
Figure 3-31 Extracted magnetic coupling coefficients versus spacing between resonators

Based on Fig.3-31 the required coupling $\vec{M}_{2,3}$ can be realized with 11.5 mil spacing between second and third resonators as shown in Fig.3-27. The electrical coupling between the first and last resonators is the most critical coupling, since the design transmission zero located very close to the centre frequency resulting a very weak electrical coupling providing a alternative signal path from input to output. This weak coupling can be realized by bigger separation, i.e. having a larger $S_{1,4}$ as shown in Fig.3-27.

Again, full wave simulator is used to obtain mode frequencies with different spacings. Some results are shown in the following figure.
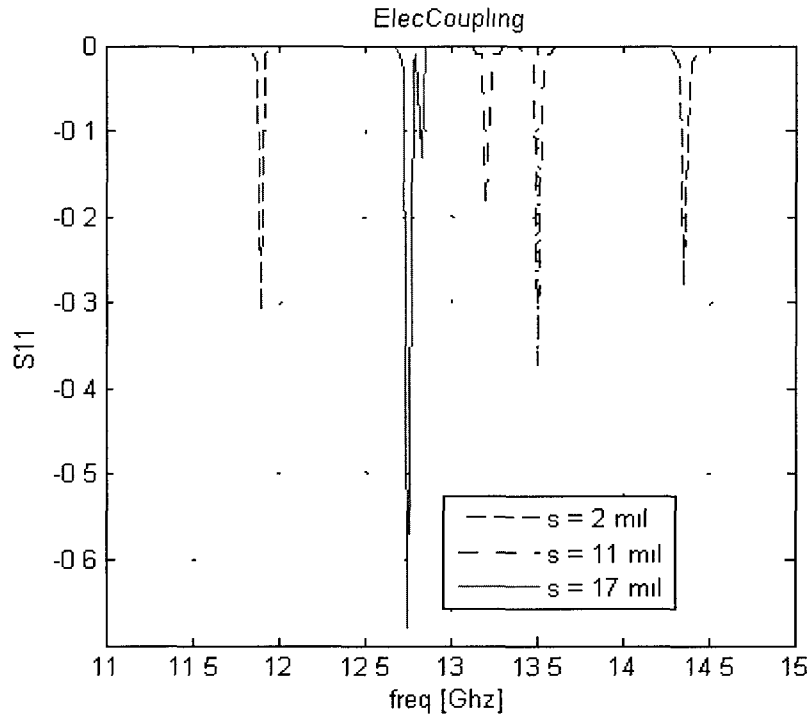
Figure 3-32 Electrical coupling responses

The designed filter was simulated and its response is shown in Fig. 3.34(a). The initial response was reasonable for the first effort showing return loss match about 3 dB worse than the required -16 dB at 13.9 GHz.

The BPF response was improved by tuning a few design parameters. Full wave simulation was performed on the BPF while changing the values of some of the gaps and spacings slightly. Adjusting gap sizes improved the pass band match as shown in Fig. 3.34(b). The width of the resonators W was also reduced slightly and a small feed offset was added to introduce another degree of design freedom to control the shape and FBW of the response. The final values for the design parameters are also given in Table. 10. The simulated broadband response is shown in Fig. 3.34(c). The in-band ripple is kept under 0.1 dB and the passband insertion loss is around 1 dB. The stop-band rejection at 500 MHz away on both high and low side of the BPF is about 40 dB.

ElectricCouplingCoefficients VS Spacing
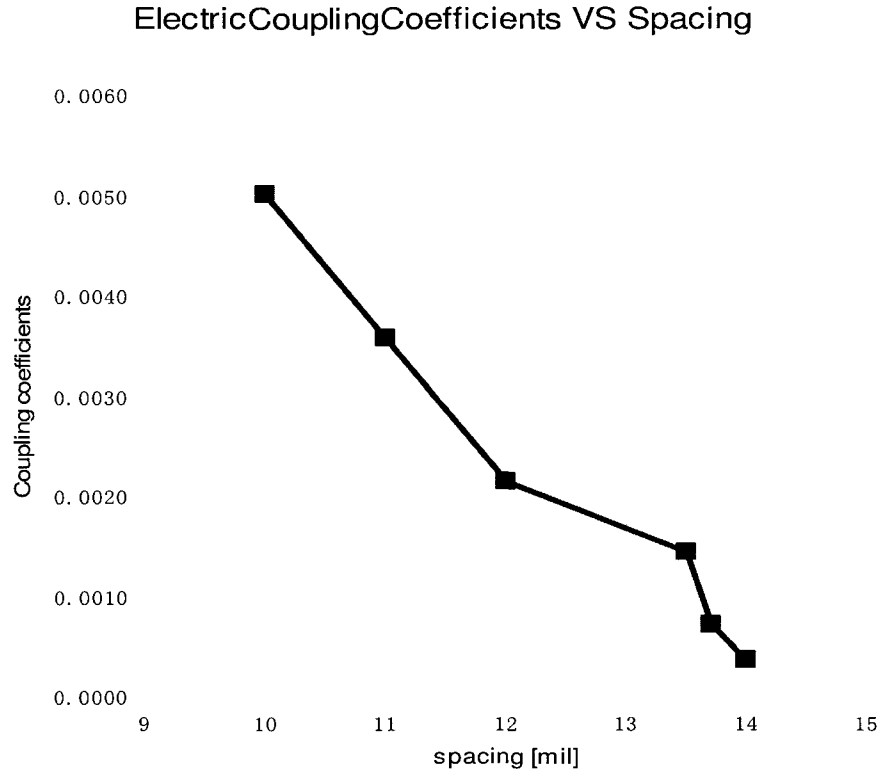
Figure 3-33 Extracted electrical coupling coefficients versus spacing between resonators

From Fig.3-33. the required coupling $\vec{M}_{3,4}$ can be realized with 14 mil spacing between first and last resonators as shown in Fig.27.

The design dimensions shown in Fig. 3-27. are summarized in Table.11.

Table 11: Design dimensions of the BPF

$S_{1,2} = S_{3,4}$	7.5 mil
$S_{1,4}$	14 mil
$S_{2,3}$	11.5 mil
$g_1 = g_2 = g_3 = g_4$	16.77 mil
L	40 mil
W	4.71 mil
X	5.0 mil
D	6.67 mil
Feed offset	0 mil

After optimization of the spacings between the resonators to control the FBW, minor adjustments of the length L of the resonators was required to shift the centre frequency of the BPF. The response is shown as follow:
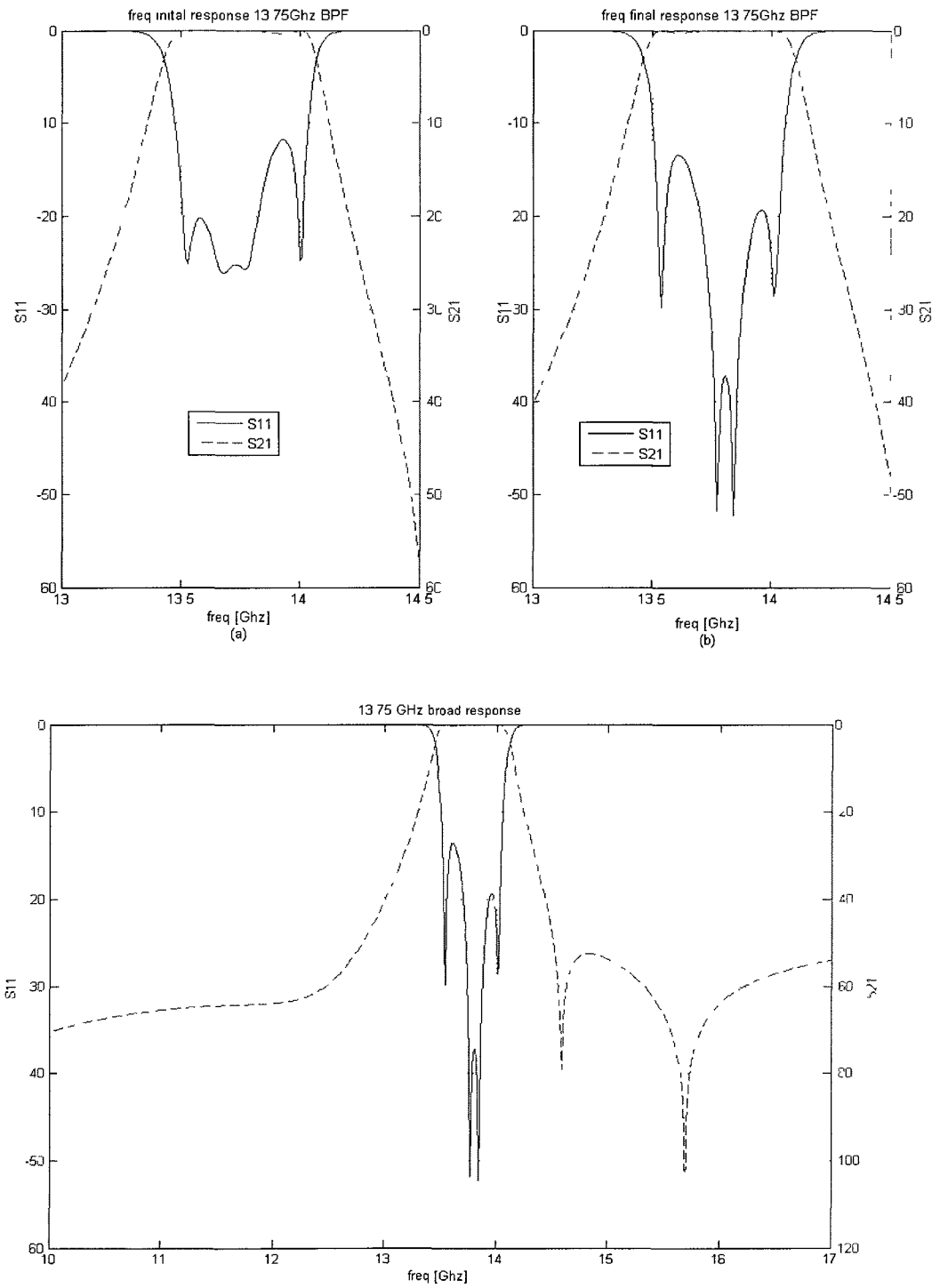
Figure 3-34 13.75 GHz BPF response. (a) Initial design (b) Final Design (c) Broad
frequency BPF response.

The return loss falls short of the-16 dB requirement at approximate 13.9 GHz corresponding to a small notch in the pass band. Shown in Fig.3-33.(a).

Fine tuning is performed with different resonator gap sizes g is shown in Fig.3-27. This tuning balances the matching responses at pass band (Fig.3-33 (b)). As a result, the pass band ripple is smaller and the notch at 13.9 GHz disappears. Further changes are required to improve filter performance: the width of the resonators W is varied from 50Ω line width and a feed offset is added. These introduce another degree of design freedom to control the shape of the S11 and FBW.

The in band ripple is kept under 0.1 dB, insertion loss is around 1 dB. The stop-band rejections 500 MHz away on both high and low side of the BPF are around 40 dB.

An interesting point about this filter response is that the attenuation pole at the lower side of the filter is missing or shifted to a higher frequency. This may be because the attenuation pole frequencies are too close to the BPF edge frequencies, or the admittance transformer value J is not correct. Since an alternative path is introduced, iterative calculation is need to modify the value for J as discussed in Section 2.2.2 and Eqns. (2.38-2.40)

The two stop-band attenuation poles are located at 14.6 GHz and 15.7 GHz respectively with attenuation levels of more than 70 dB, resulting in a steeper roll off on the high side of the BPF. Out of band rejection at high side of the BPF is still better than 50 dB increasing the attractiveness of this filter for LO filter applications in radio transceivers. The final design dimensions are shown in the following table.

Table 12:   Final design dimensions of the BPF

$S_{1,2} = S_{3,4}$	7.22 mil
$S_{1,4}$	14 mil
$S_{2,3}$	11.5 mil
g_1	16.77 mil
g_2	16.65 mil
g_3	16.37 mil
g_4	16.45 mil
L	40 mil
W	4.73 mil
X	5.0 mil
D	6.67 mil
Feed offset	3.02 mil

3.3   Case Example: V-band BPF Design with Duroid 5880

In this section, a similar open-loop-resonator type BPF is designed using Rogers Duroid 5880 [10] but now at V-band frequencies so as to serve as the diplexer BPF connecting to the antenna port (as shown in Chapter 2). To meet the diplexer BPF specifications discussed in Section 2.1.7, the 5880/5880LZ series of Duroid substrates is used. This Rogers substrate exhibits the lowest loss in the Duroid family. The main difference between the Duroid and alumina substrate used in the previous section is that Duroid, being Teflon based, is very soft.

To recall, Rogers 5880 offers a dielectric constant ε_r of 2.3 and a loss tangent of 0.0009. The height of the substrate used is 5 mil, with 0.5 oz copper metallization to minimize metal loss. Effective dielectric constant depends on the conductor width W and the effective dielectric constant ε_{eff} is approximate 1.9. The required width of the 50Ω microstrip transmission line is 0.373 mm, and the half-wave length is approximately 1.812 mm (Eqn.2.54-56).

Since the 50   microstrip width of the open-loop-resonator are about one quarter of the required total length ($\lambda_g/2$), it will be very difficult to layout because the length of resonator is also about one quarter of the required resonator length. To overcome this problem, a high impedance resonator is designed to achieve a thinner width W with respect to length of the resonator.

In order to increase the out of band rejection of these filters to meet the diplexers specifications shown in Table.6, a sixth order BPF with pseudo-elliptic response was designed. Recall that the fourth order filter designed in the previous section was only able to achieve around 35 dB ~ 40 dB of out of band rejection (at 2 GHz offset).

3.3.1 Specifications and calculations

A fourth-order filter has 35 dB ~40 dB rejection 2 GHz away from the passband. The centre frequency of the filter is 56 GHz, and the bandwidth is 1 GHz resulting in $FBW = \dfrac{1\,GHz}{56\,GHz} = 1.78\%$. The transmission zeros are located 1 GHz away from the centre frequency. The passband ripple is set to be 0.1 dB which corresponds to 16dB return loss. Using Equations (2.38) – (2.40). The following pseudo-elliptic low pass prototypes are determined and shown in the following table:

Table 13: Pseudo-elliptic low pass prototype parameters 6th order

g_0	1.00
g_1	1.17
g_2	1.40
g_3	2.06
J_2	-0.24
J_3	1.29

As shown in Sections 2.2 and 3.1, for the design of the 4th order BPF, and using the frequency transformation equations of Eq. (3.12), the following coupling matrix is calculated as follow.

$$\vec{M} = \begin{bmatrix} 0 & 0.01394 & 0 & 0 & 0 & 0 \\ 0.01394 & 0 & 0.01051 & 0 & -0.01054 & 0 \\ 0 & 0.01051 & 0 & 0.01119 & 0 & 0 \\ 0 & 0 & 0.01119 & 0 & 0.01051 & 0 \\ 0 & -0.01054 & 0 & 0.01051 & 0 & 0.01394 \\ 0 & 0 & 0 & 0 & 0.01394 & 0 \end{bmatrix} \quad (3.16)$$

3.3.2 Open-loop-resonator BPF design at V-band with Duroid
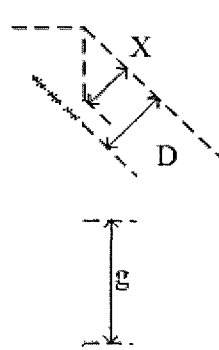
The following table summarizes the Duroid properties required for the implementation of a V-band BPF.

Table 14: Properties and tolerances of Duroid 5880 substrate

ε_r	2.3
$\tan \delta$	0.0009
Substrate thickness, h	5 mil
Metalization, Gold	17.5 μm
Surface roughness	5 μinch
Track tolerance	$\pm \dfrac{1}{5}$ mil
Pull back	2 mil

The length of each side of the open-loop-resonator was first set at about one quarter of $\lambda_g/2$, or 0.453mm (17.8 mil), which is about the same as the width of a 50Ω line. A smaller width of line for the resonator must be used to accommodate the square geometry. A width of 0.084 mm (3.31 mil) was used, corresponding to a 100Ω characteristic impedance, and impedance matching networks were designed at the input and output of the filter to match to 50Ω. The corners were optimally mitered based on Eqns. (3.14-15) to reduce losses due to the 90° bends. The resonator was then tuned to operate at 56 GHz. The final dimensions for this resonator are shown in Fig. 3.35. The resonance at 56GHz can be seen clearly in the simulated frequency response of this structure shown in Fig. 3.36.

Table 15: Final dimensions of the resonator after optimization

L	20 mil
W	3.31 mil
X	4.27 mil
D	7.35 mil
g	6.52 mil
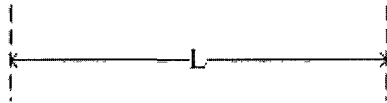
Figure 3-35 100Ω resonator with optimal mitered bend

The following plot shows the frequency response of the resonator clearly showing that resonate at 56 GHz.
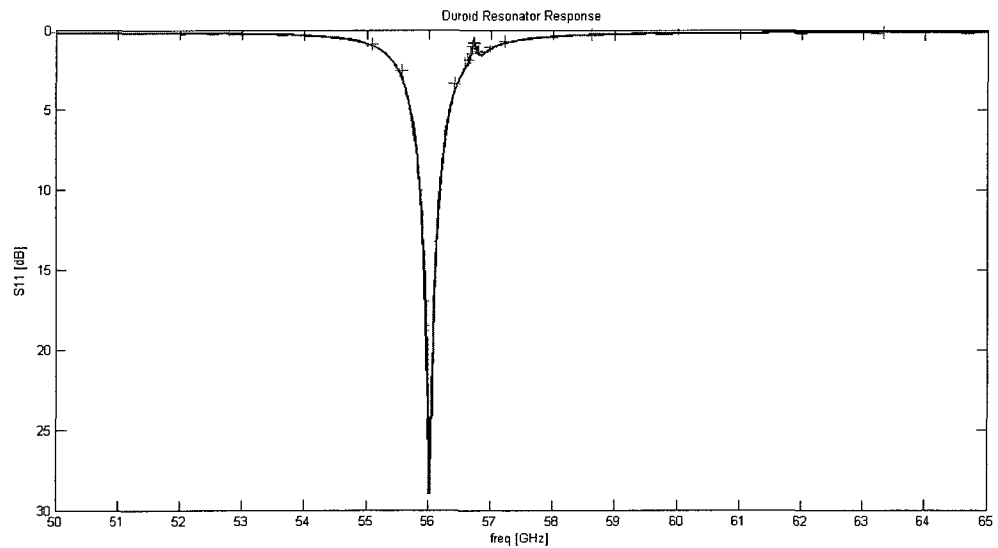
Figure 3-36 Frequency response of 100Ω resonator with optimal mitered bend

In addition to the four resonator configuration shown in the previous section, two additional resonators were introduced at the input output and with coupling coefficients of $\vec{M}_{1,2} = \vec{M}_{5,6} = 0.01394$ Eq. (3.16). The rest of the circuit was similar to the previously shown 4th pole BPF design but with an alternative coupling path between 2nd and 5th resonators, as shown in the coupling matrix $\vec{M}$ in equation (3.16). A tap feed mechanism was used with a single stage matching to transform high filter impedance to 50Ω [30], and shown in the Fig. 3-37.
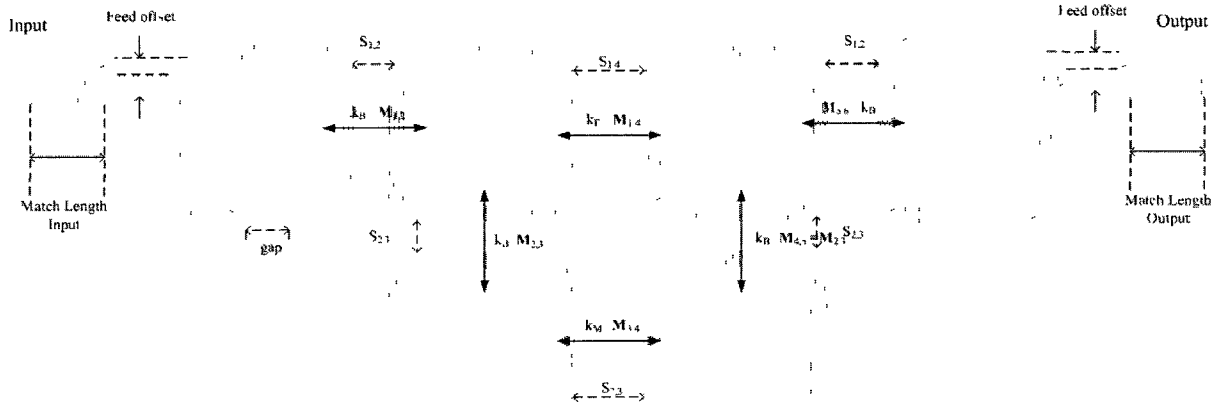
Figure 3-37 Schematics of the sixth order BPF
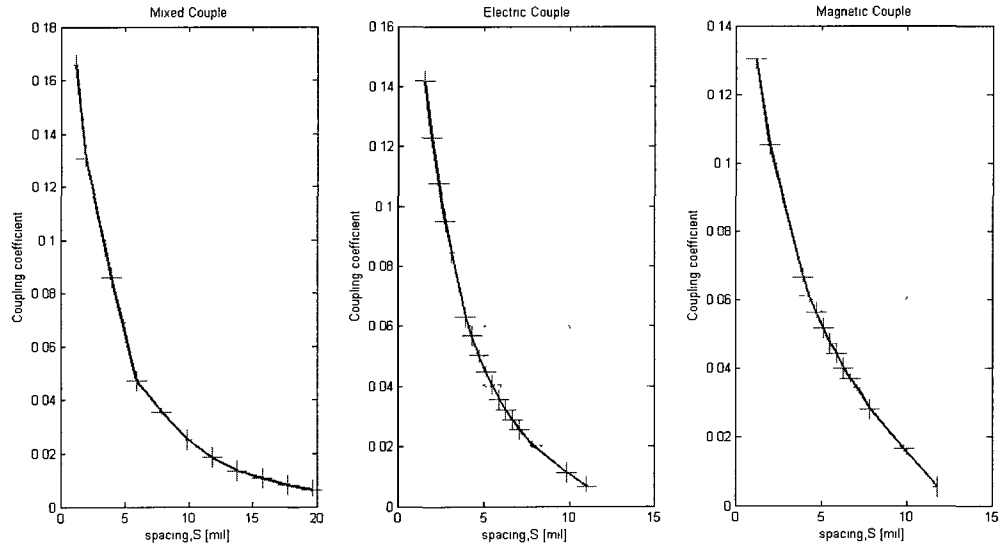
Figure 3-38 Coupling coefficients of Mixed, Electrical and Magnetic coupling
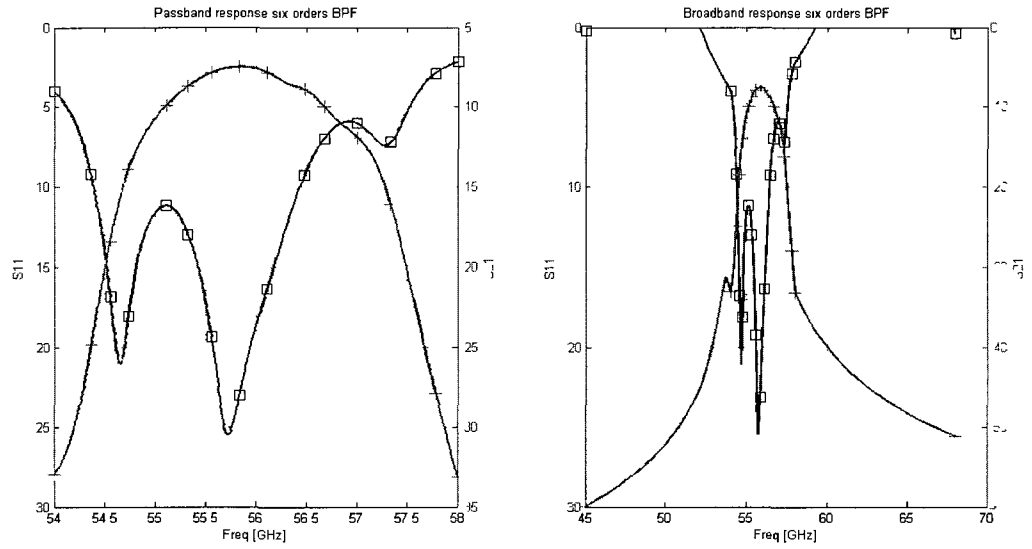
Figure 3-39 Passband and broadband frequency response of the 6th order BPF

As previously shown with the alumina filter design, the next step was to simulate the various coupling configurations shown in Fig. 3-22 between the resonators on Duroid substrate at 56GHz. Results are presented in Fig. 3-37.

Table 16: Final dimensions of the resonator after optimization

$S_{1,2} = S_{5,6}$	13.4 mil
$S_{2,5}$	10.6 mil
$S_{2,3} = S_{4,5}$	10.2 mil
$S_{3,4}$	9.45 mil
L	20 mil
W	3.31 mil
X	4.27 mil
D	7.35 mil
g	6.52 mil
Feed offset	0 mil

Matching Length	24 mil
Matching Width	26.1 mil

The results of the sixth-order pseudo-elliptic filter exhibit issues with the open-loop-resonator BPF designs in the V-band frequencies. The insertion loss is around 7 dB at the design centre frequency, which does not meet the targeted specifications. The insertion loss of the filter is high due to two effects. Firstly, the required coupling coefficients in the coupling matrix Eqn. (3.16) are quite small, less than 0.014, due to the very small FBW of the filter. From Fig. 3.38, it can be seen that once the coupling coefficients are about 0.01, the gaps between the resonators are about 12 ~ 15 *mil*, depending on the type of coupling and corresponding to almost the length of the resonator. These large gaps significantly increase the insertion loss of the filter. Secondly, conductor loss due to the additional matching networks required to transform the100 narrower microstrip feed to 50   at 56GHz, increases the insertion loss. Also the simple matching network used in this design does not perform very well since the input return loss is not below the 15dB specification. However, use of a higher-order matching network would further increase the insertion loss.

Secondly, the passband width is 50% wider than the targeted specification of 1 GHz . This is likely due to the small Q factor of the resonators. Six of them closely coupled together will actually form a pass-bandwidth wider than the 1.78% specification. The attenuation poles in this design are very close to the passband. This makes the negative coupling difficult to be realized. From Fig. 3.39, the attenuation pole at the lower side of the pass-band appears at around 54.5 GHz while the pole on the upper side of the passband does not appear. This is due to the inaccurate value achieved for the negative coupling required between the two electrical coupled resonators in the design.

In conclusion, the K band filter design was successful. It has good rejection to attenuate harmonics and sub-harmonics from entering the V-band mixer and generate even more spurious as discussed in Chapter 2, and having good matching the passband

ripple is kept to minimum. However, the design of a six pole BPF using open-loop resonators presented major difficulties at V-band frequencies. The implementation of frequency diplexers for narrow channel links is hindered by their high loss and the difficulty to achieve accurate coupling between the resonators. In order to overcome the constrains of open-loop-resonators as well as other printed circuit filters, a three-dimensional cavity-based BPF circuit will be presented in the next chapter.

Chapter 4   Substrate Integrated Waveguide (SIW) BPF Design with LTCC

In pursuit of the third thesis objective, this chapter presents novel V band bandpass filters designed using substrate integrated waveguide resonators in a multi-layer low-temperature co-fired ceramic process. These designs will constitute an alternative implementation of the diplexer placed between the TX, RX and COM ports of the system described in Chapter 2. This diplexer is compact and easy to integrate when compared to traditional waveguide solutions.

4.1 LTCC Process

LTCC is an excellent packaging candidate for building microwave and RF modules. Up to 25 layers may be stacked and various LTCC tape materials are available for different applications. Some of the properties of LTCC substrates are shown in Table 17.

Table 17: Some properties of LTCC tape materials

	Dupont951	Dupont943	FerroA6-S	Heraeus CT2000	$SiO_2 - B_2O_3$ glass
ε_r	7.80	7.80	5.90	9.10	5.60
$\tan \delta$	0.0015	0.0010	0.0020	0.0010	0.0015
Shrinkage% in Z-axis, XY axis	15,12.7	13,10	27,15.5	14,11.5	N/A

Besides LTCC's multilayer capability, it is possible to have inter-layers connection with via holes and striplines. It is also possible to have pockets and bondable gold or silver with gold plated metallization. In addition, vias in LTCC processes are filled with

metal and able to sink heat much better than regular hollow via in other substrate technologies .With all these 3-D circuit features the size of the LTCC transceiver module can be reduced considerably. In addition, the LTCC design variables available in commercial processes makes it an ideal candidate for developing high performance passive components such as multilayer broadband capacitors, multilayer high Q stacked inductors, resistors at microwave frequencies and frequency selective components. Fig 4-42 shows a representative LTCC module.
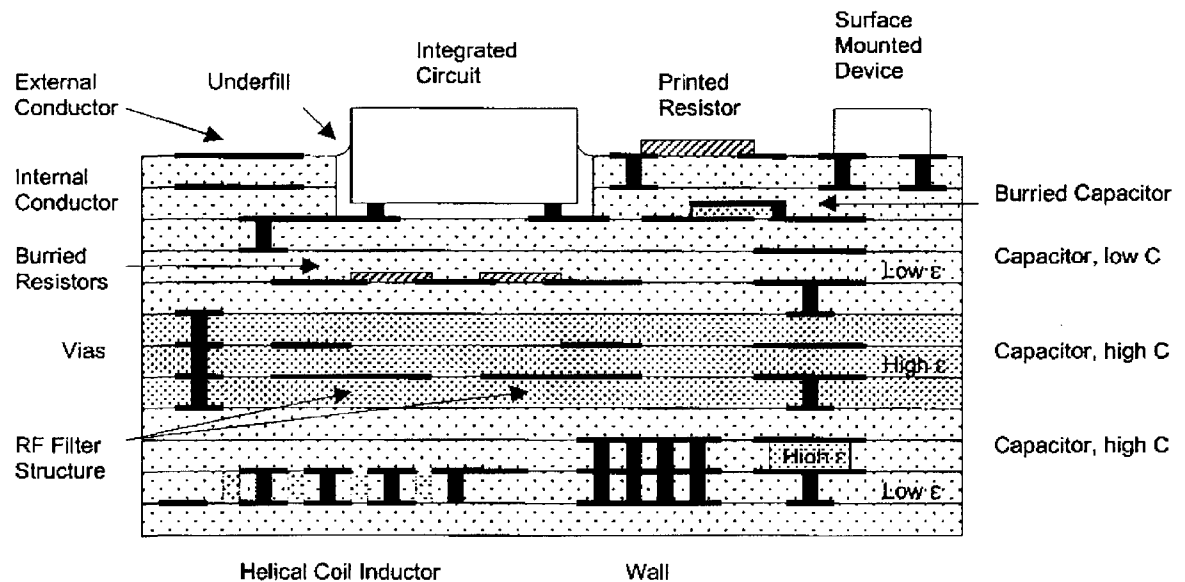
Figure 4-40 A 3-D LTCC circuit

4.2 SIW Cavity Structure

The implementation of a 3-D cavity structure using commercial packaging technologies such as LTCC is difficult due to process limitations. The lack of vertical walls required to form the cavity resonator have inspired researchers to make some approximations and modifications to the classical cavity resonator structure (Fig. 4-40). Here, the top and bottom faces of the cavity are realized using metallization sheets while the vertical walls are implemented using a fence of vias. One must however keep in mind that via fences are not perfect conductor walls and the radius R and pitch P of via posts will affect the effective size of the designed cavity. Fig.4.41 shows the SIW type of cavity used here.
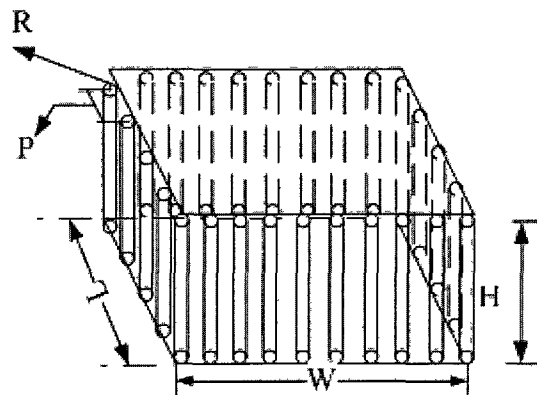
Figure 4-41 A SIW cavity

The design of an air filled rectangular cavity was described in section 2.3.3. Recall that the resonance frequencies of a SIW cavity for a given microwave mode, can be estimated with equations (2.65-2.68) as follows: [20] [21]

$$f_{TE,nmp} = \frac{C}{2 \cdot \sqrt{\varepsilon_r}} \cdot \sqrt{\left(\frac{m}{W_{eff}}\right)^2 + \left(\frac{n}{H}\right)^2 + \left(\frac{p}{L_{eff}}\right)^2}$$

$$L_{eff} = L - \frac{(2 \times R)^2}{0.95 \times P} \qquad (4.1)$$

$$W_{eff} = W - \frac{(2 \times R)^2}{0.95 \times P}$$

where c corresponds to the speed of light, ε_r represents the dielectric constant of the LTCC tap. W and L are the physical width and length of the cavity, W_{eff} and L_{eff} are the equivalent length and width of the rectangular cavity respectively.

Two SIW cavities were designed to excite the TE_{101} resonant frequency of the SIW at 56 GHz and 58 GHz respectively and using Ferro A6-S LTCC tapes. Initial design dimensions are calculated using Eqn. 4.1. The radius of via R is set to the thickness of the tape layer, 100 μm. The pitch of the via fencing is set to be four times of via radius, while the height of the cavities is 200 μm or the equivalent to two tape layers. Results are summarized in Table.18:

Table 18: Dimensions of SIW cavity

	56 GHz		58 GHz	
	Calculated	Simulated	Calculated	Simulated
$f_{TE,101}$	56 GHz	55.9 GHz	58 GHz	57.9 GHz
L_{eff}	1.61 mm	N/A	1.54 mm	N/A
W_{eff}	1.51 mm	N/A	1.47 mm	N/A
L	1.71 mm	1.67 mm	1.64 mm	1.62 mm
W	1.61 mm	1.61 mm	1.54 mm	1.55 mm
H	200 μm	200 μm	200 μm	200 μm

The unloaded Q factor of this SIW cavity was calculated using HFSS and found to be 677. The height of the cavities does not directly affect the Q of the resonator and increasing the number of via fence rows does not improve the Q either, even though more via fence rows is expected to reduce leakage from adjacent via poles. Additionally, the shape of the resonator should ideally be square by keeping dimensions W and L as close to each other as possible in order to move the higher mode frequencies further away from the frequency band of interest.
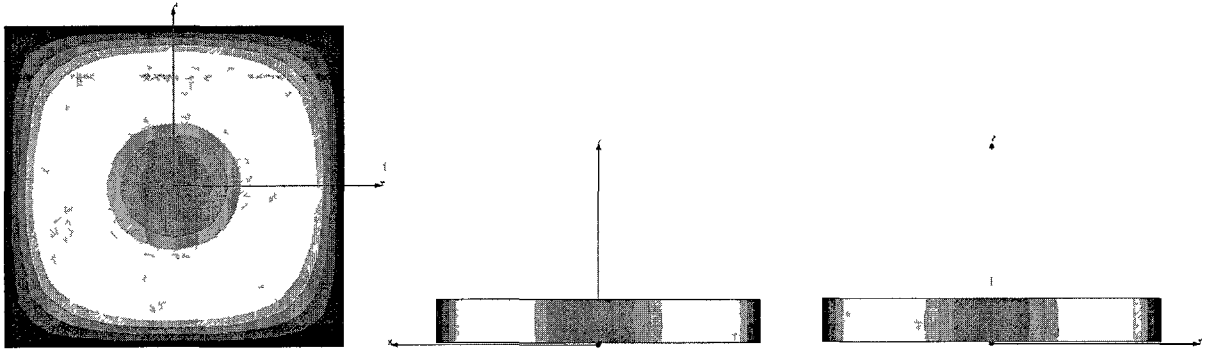
Figure 4-42 E field plot of the SIW cavity showing TE_{101} mode of operation

Simulated E field plots in x-y, x-z and y-z plane clearly showing the changes of E field in x, y and z axis.

4.3 Open Stub Coupling Mechanisms Design

An aperture coupling making use of an open circuit stub is selected to feed the signal into the resonator. This structure is relatively easy to build as it requires only one additional metal layer above the cavity. The open circuit stub shares its ground plane with the top layer for the rectangular SIW and a the signal is fed into the resonator via a slot opening (Fig. 4.43).The width of the open stub is tapered to transition the required impedances. The input feed is built on a single layer tape substrate, the width required to implement a 50Ω width microstrip (*feedWidth*) is calculated based on 100 µm tape. However when the feed line approaches the slot opening on the top metal of the cavity, the equivalent substrate height changes, e.g. the ground reference is now the bottom metal of the cavity.

As a result, after the feed line approaches the cavity edges, a wider feed line is required (*feedInWidth*) to compensate the slot opening effect. The position (*slotPosition*) and the length (*slotLength*) of the slot are also two design parameters used to tune the impedance and evaluate the coupling mechanisms into the resonator. The following figure shows the design variables used to design the feed to resonator.

SW	Slot Width
FW	Feed Width
SP	Slot Position
FIW	Feed In Width
FIL	Feed In Length
SL	Slot Length

(a)

(b)
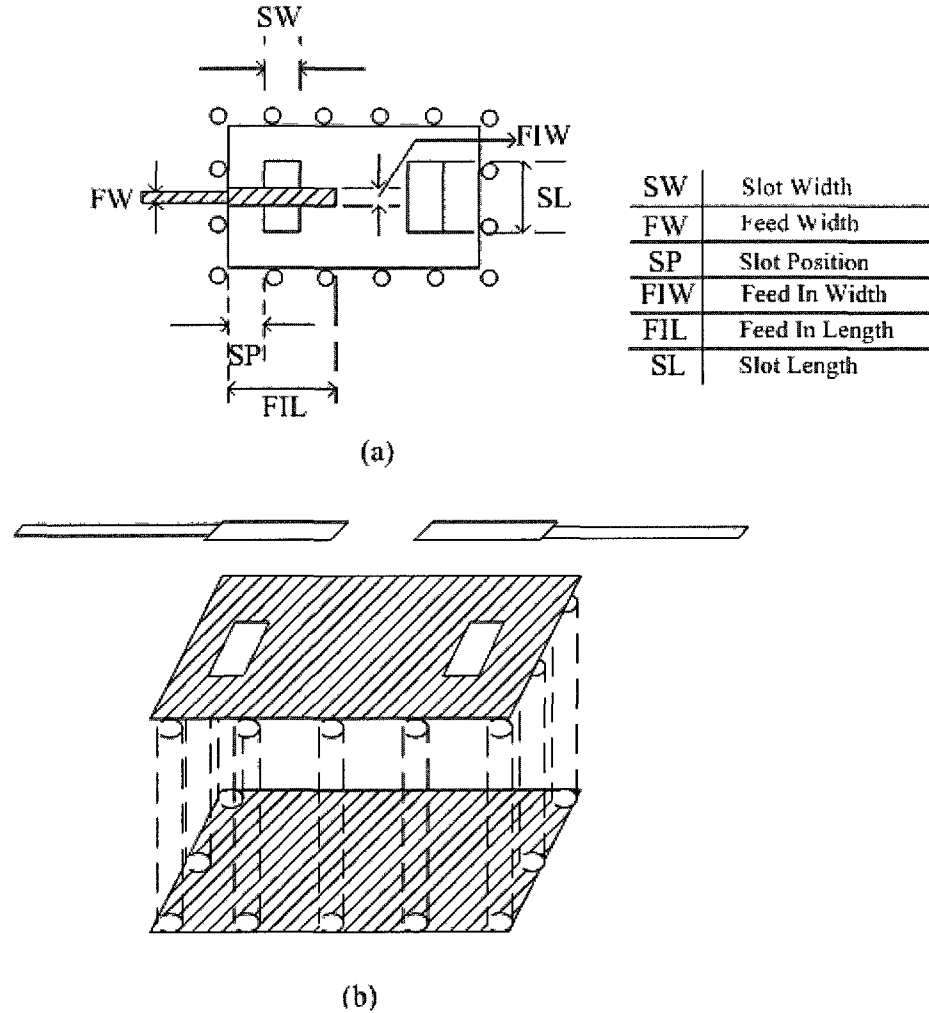
Figure 4-43 Open stub feed structure coupling to SIW cavity via open slots. (a) top view, (b) 3-D view

Initially, the position of the coupling slots are equally spaced with respect to the edges of the cavity shown and *SP* (*slotPosition*) in Fig.4-43, set equal to $\frac{\lambda_g}{4}$. The width

of the slot *SW* (*slotWidth*) in Fig.4-43 is initially set to $\frac{\lambda_g}{8}$. The length microstrip feed

above the SIW resonator *FIL* in Fig.4-43 (*feedInLength*) is set to be $\frac{\lambda_g}{2}$, as an open

circuit microstrip resonator. The width of the feed shown as *FIW* in Fig.4-43 is initially

set to be the same as the width of input feed shown as *FW* in Fig.4-43, since the size of

the slot opening is relatively smaller than the length of the feed, and the effect of thicker

substrate is assumed to be negligible. The width of the input feed, corresponding to

$Z_0 = 50\Omega$ when using one tape layer which is 100 μm can be calculated with Eqn. 3.10.

Lastly, the input and output feed are actually quite close and there are fringe fields that

make the size of the microstrip feed appears electronically smaller, these fringe fields can

be modeled as discussed in Section 2.3.2 Eqn. (2.54) and (2.55). The calculated Δd is

approximately $\frac{\lambda_g}{25}$. After fine tuning in order to obtain best matching at the respective

design frequency, the design parameters dimensions and responses are shown with Fig.4-

44 and Table 19.

The sizes of the SIW resonators are optimized by using EM software. Special

attention needs to be paid to the two aperture openings at the top metal surfaces of the

cavity as they disrupt the boundary explained in Section 2.3.3. Since the cavity is no

longer metallically enclosed, these apertures are also the places where the power at input

and output are magnetically coupled. Due to imperfect metallic enclosure, E fields around

this opening are disrupted. This is shown in Fig.4-45, where the incident E fields are no

longer uniform inside the cavity. As a result, the size of the cavity appears to be

electrically smaller. The filter response is highly sensitive to the physical dimensions of

the cavity. In later sections, the sensitivity of the BPF design parameters will be studied.
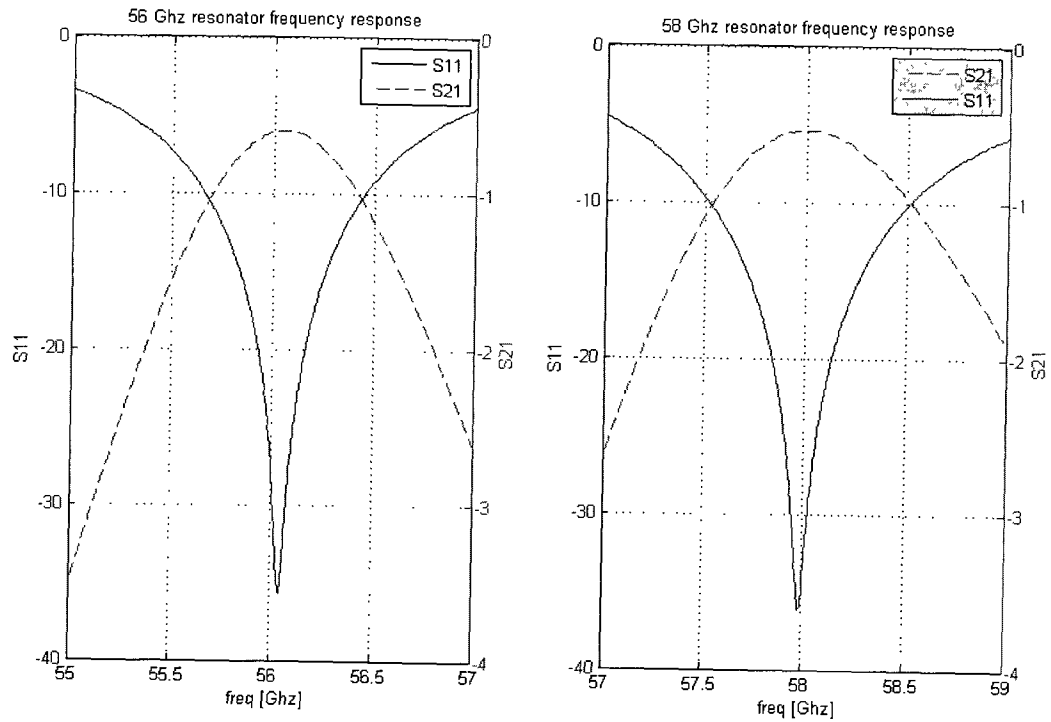
Figure 4-44 56 GHz and 58 GHz resonators responses with open stub feeds
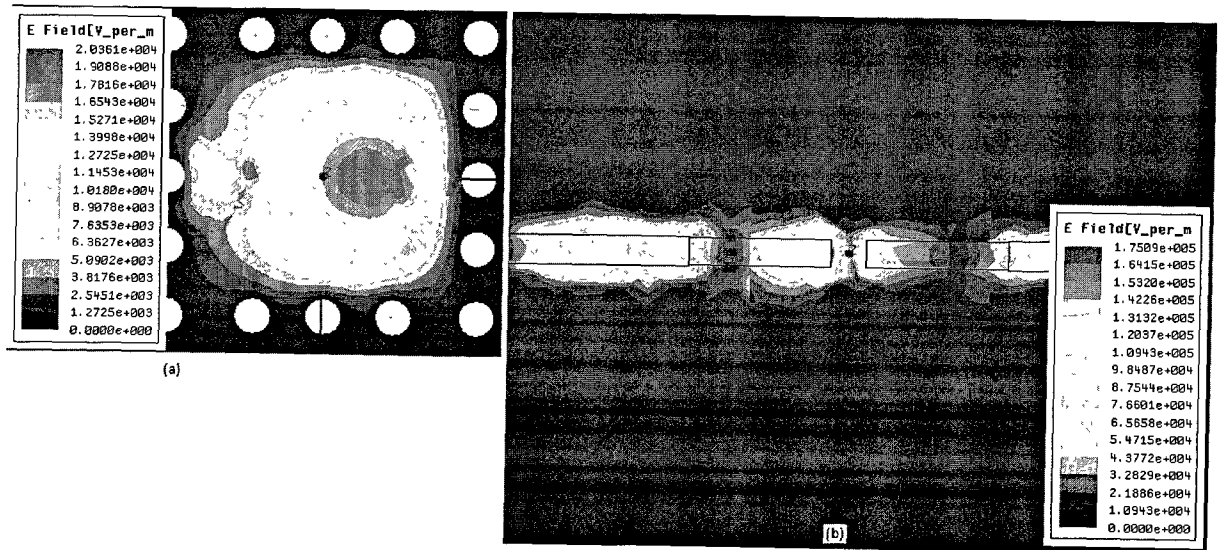
Figure 4-45 E field plots.(a) cavity E-field. (b) Feed E-field

With Fig. 4-45. The E-field plots indicate a disturbance of the E-field inside the cavity due to the discontinuity at the cavity openings especially just above the input and output apertures. The TE_{101} mode still remains the only excited mode at this frequency.

For the feed structure, the strongest E-field appears at the open circuited ends as expected, around the $\frac{\lambda_g}{4}$ back off (*FIL - SP*) as shown Fig.4-43 (a). Also, the E-field at the slot openings is very weak, confirming that the power is being magnetically coupled into the resonator.

The insertion loss of a single resonator is about 0.5 dB. The loaded Q can be estimated to be the ratio of resonating frequencies and the -3 dB bandwidth, or the resonating frequencies over -10 dB S11 bandwidth.

$$Q_{\text{load}} = \frac{f_{\text{resonant}}}{\Delta f} \quad (4.2)$$

The loaded Q for the coupled resonators is around 60. Table 19 summarizes the design parameters:

Table 19: Final cavity design parameters

W 56, 58 GHz	1.41, 1.34 mm
L 56, 58 GHz	1.57, 1.37 mm
H 56, 58 GHz	200 μm,200 μm
Feed width	0.15 mm
Feed in width	0.16 mm
Feed in length	0.7 mm
Slot position	0.2 mm
Slot width	0.21 mm
Slot length	0.538 mm

4.4 Coupling between SIW Resonators

The coupling mechanism between two or more SIW resonators is achieved electrically. Power is propagating in the TE_{101} mode, which has only one resonating point where electrical coupling can be realized between adjacent resonators. There are two ways of achieving this coupling:

- By removing one or more vias from the via fencing that separating the two adjacent resonators just as the coupling iris in traditional waveguide filters as shown in Fig.4-46 (a). The amount of coupling can be controlled by the number of vias removed [22]. The main advantage of this technique is its ease of implementation. In addition, this method does not require additional metal layers, making it suitable for packaging technologies that have no multilayer capability, e.g. Rogers Duroid family. The disadvantages of using this coupling technique include the difficulty to control and realize small coupling coefficients, required at high frequencies. Since the physical size of the cavity is small, the via fencing may consist of just a few vias.

- By making a small opening on the shared metal boundary between two adjacent cavities, shown in Fig.4-46 (b). The amount of coupling can be controlled by adjusting the size / position of the internal slots [23]. The advantages of the method include the ability of realizing small coupling coefficient, and increased degree of freedom to fine tune the amount of E fields coupling from one cavity to the next one. This coupling technique is ideal for the diplexers required in this work and which require a small FBW at V-band frequencies. The disadvantages of this method is that it requires additional metal layers, but since the LTCC process selected can have up to 25 metal layers, this issue will not represent a problem for this design.

96
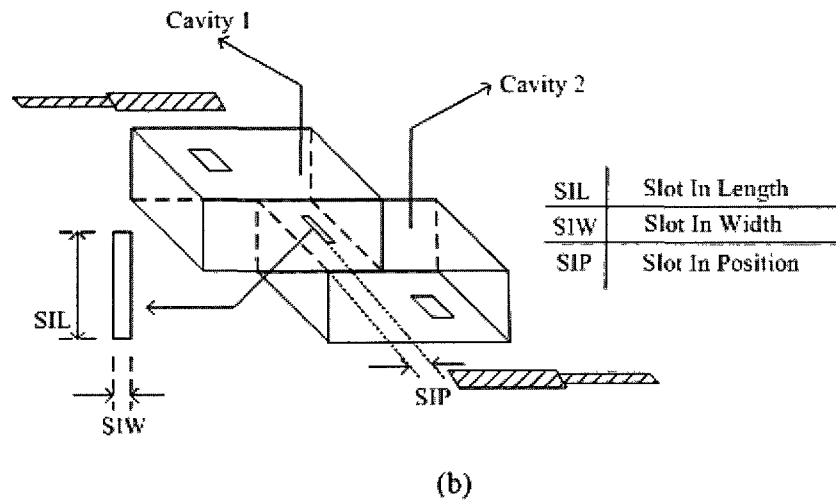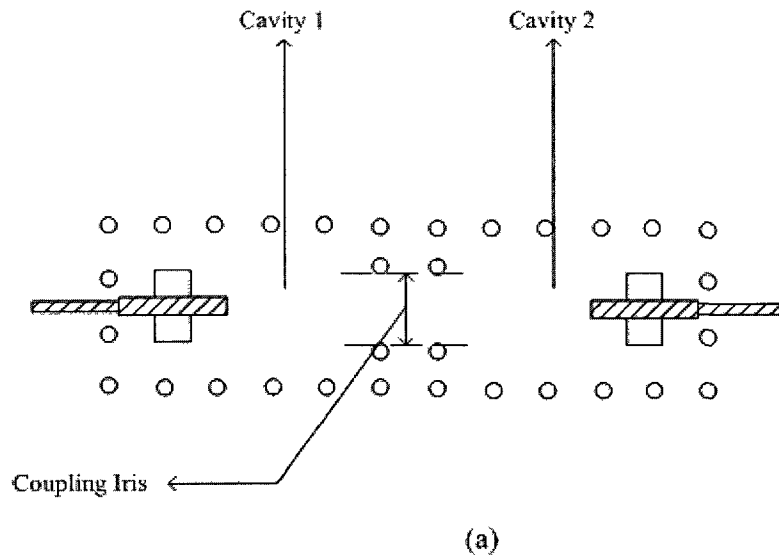
Figure 4-46 Coupling methods.(a) coupling iris, (b) coupling slots in between cavities

As previously described, the coupling slot method is used to obtain the desired coupling coefficients for BPF designs. By adjusting the width of the internal slots, SIW, the mode frequencies of the two adjacent resonators will experience a frequency shift as described in Section 3.1. Simulation plots are shown in Fig.4.47. Small coupling coefficients are calculated with Eqn.3.4 in Section 3.1.The amount of couplings versus coupling slot dimensions is summarized in Fig.4.48.
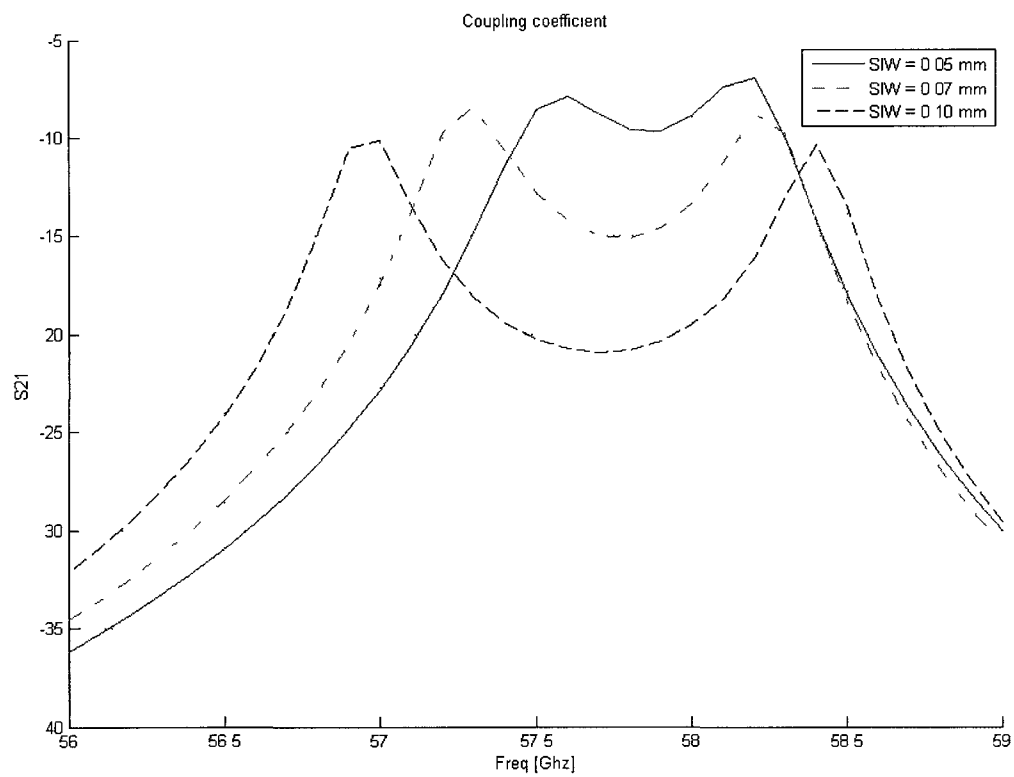
Figure 4-47 Coupling responses, mode frequencies
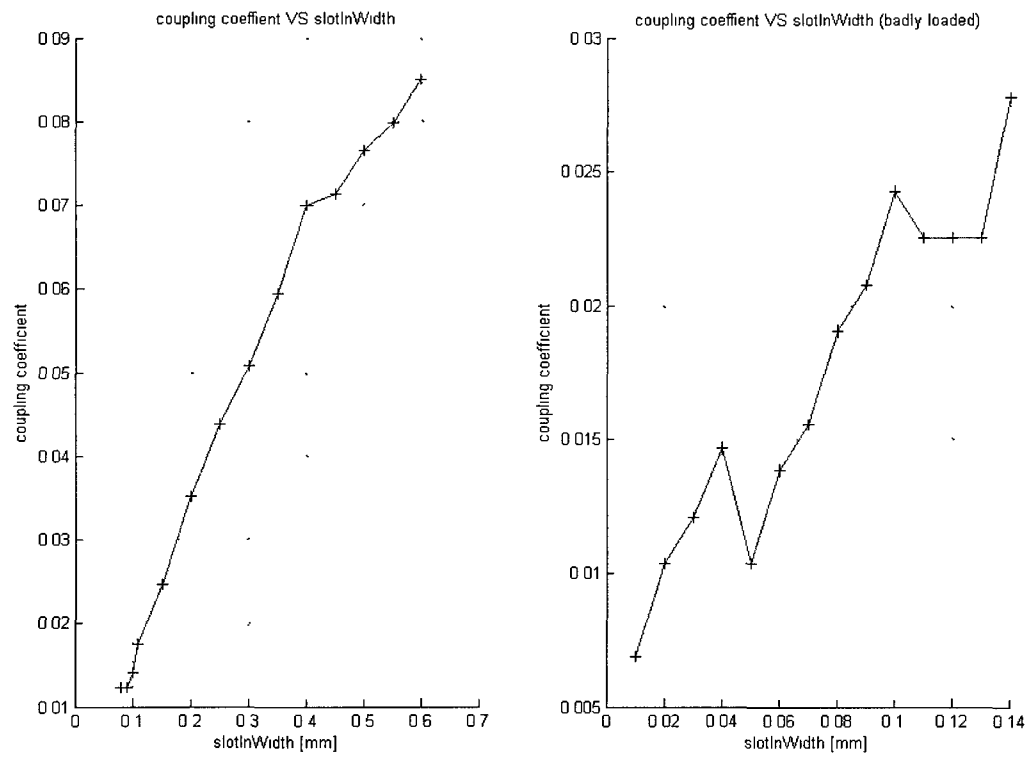
Figure 4-48 Electrical coupling coefficients vs. internal slot widths

4.5 Three-Pole Cavity BPF Design

In this section, several BPFs are designed to meet the diplexer specifications discussed in section 2.1.7 and in Table.6. The number of poles for the BPFs is chosen to be three. The required pass bandwidth of the filter is 1 GHz centered at 56 GHz and 58 GHz, respectively. This corresponds to FBW of only 1.8 % and 1.7 % respectively. The most difficult specification of the diplexers is the required spurious rejection for LO leakage power. As previously shown in Table 6, more than 41.7 dB of rejection would be required 2 GHz away from the centre frequencies, while exhibiting insertion loss of 2 dB or better in order to achieve an overall insertion loss for the diplexer of 3.5 dB or better (accounting for loss of approximately 1.5 dB in the microwave transition from microstrip at module level to waveguide interface). In this section, a Chebyshev response BPF is designed to meet the target diplexers specification. Table 20 summarizes the BPF specifications

Table 20: Target specifications of BPFs

	Target
Number of cavities	3
Centre frequencies	56, 58 GHz
FBW	1.8%, 1.7%
Input match S11	$\leq 16\,dB$
Insertion loss, IL	$\leq 2.5\,dB$
Passband flatness within 225 MHz	$\leq 0.2\,dB$
Rejections 2 GHz offset from pass band	$\geq 42\,dB$
Group delay	5 ns average

The Chebyshev low pass prototype is discussed in Section 2.2.2. This filter's design parameters can be calculated using equation (2.36). After the initial low pass prototype is designed, the desired band pass response is produced using the frequency transformation and as shown in equations (2.44) – (2.47).

Table 21: Chebyshev low pass prototype parameters

g_0	1
$g_1 \cdot g_2$	1.417
$g_2 \cdot g_3$	1.417
g_4	1

A symmetrical BPF is produced by choosing an odd order. As a result, the coupling coefficient between the first and second cavity is the same as the coupling coefficient between the second to third cavity, (Table 20). As discussed in section 2.2.3 and the required coupling coefficients of the BPF can be calculated as follows [23]:

$$\vec{M}_{1,2} = \vec{M}_{2,3} = \frac{\text{FBW}}{\sqrt{g_1 \cdot g_2}} = \frac{\text{FBW}}{\sqrt{g_2 \cdot g_3}} \quad (4.3)$$

The resulting coupling matrix is:

$$\vec{M} = \begin{bmatrix} 0 & 0.015 & 0 \\ 0.015 & 0 & 0.015 \\ 0 & 0.015 & 0 \end{bmatrix} (4.4)$$

And the required external quality factor can be calculated as:

$$Q_{e,i} = Q_{e,o} = \frac{g_1 \cdot g_2}{\text{FBW}} \quad (4.5)$$

Lastly the coupling coefficient can be calculated using EM analysis as shown in Fig.4-47 and in reference to Section3.1. Results were presented in Section 4.4. As seen in Fig.4-48, from the extrapolated plot, the required $\vec{M} = 0.015$ can be obtained by sizing the internal slot width to approximately 0.04 mm. The open stub input and output coupling structure discussed in previous section is used here.. The sizes of the resonators are kept

101

the same for the initial design and without considering the effects of the slot openings in the I/O cavities. The following figure shows the schematics of the three poles/cavities BPF.

SW	Slot Width
FW	Feed Width
SP	Slot Position
FIW	Feed In Width
FIL	Feed In Length
SL	Slot Length
SIL	Slot In Length
SIW	Slot In Width
SIP	Slot In Position
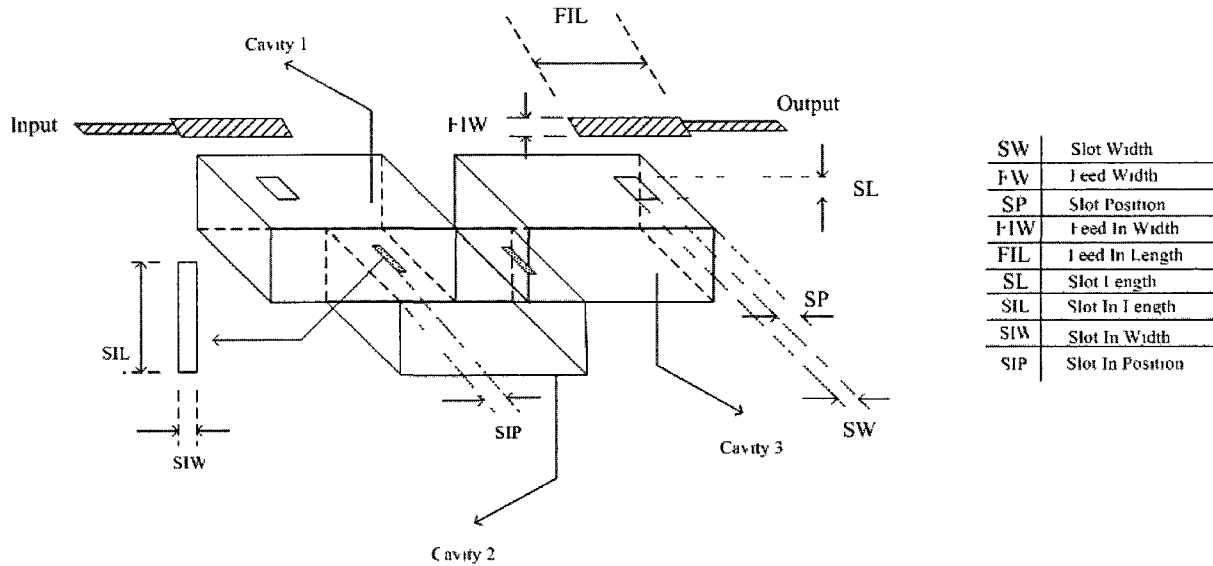
Figure 4-49 Schematics of three cavities BPF

Initial design parameters are shown in Table 20 and Table 21. The initial design, using identical dimensions for all cavities, fails to meet the required specifications as shown in Fig.4-50; the matching is not adequate especially in the middle of the passband, also, there is a transmission notch at around 57 GHz and the return loss around 57 GHz degraded by 3dB. In addition, the FBW is larger than expected , because the middle cavity (*cavity2* in Fig.4-49.) has a different electrical size than cavity 1 and 3. The sizes of the I/O coupling slots are too significant to ignore;
$0.21\,\text{mm} \times 0.538\,\text{mm}$ compared to the 58 GHz cavity size of $1.34\,\text{mm} \times 1.37\,\text{mm}$. Due to the differences in the cavity sizes, the required coupling coefficients were also changed to $1.34\,\text{mm} \times 1.37\,\text{mm}$.
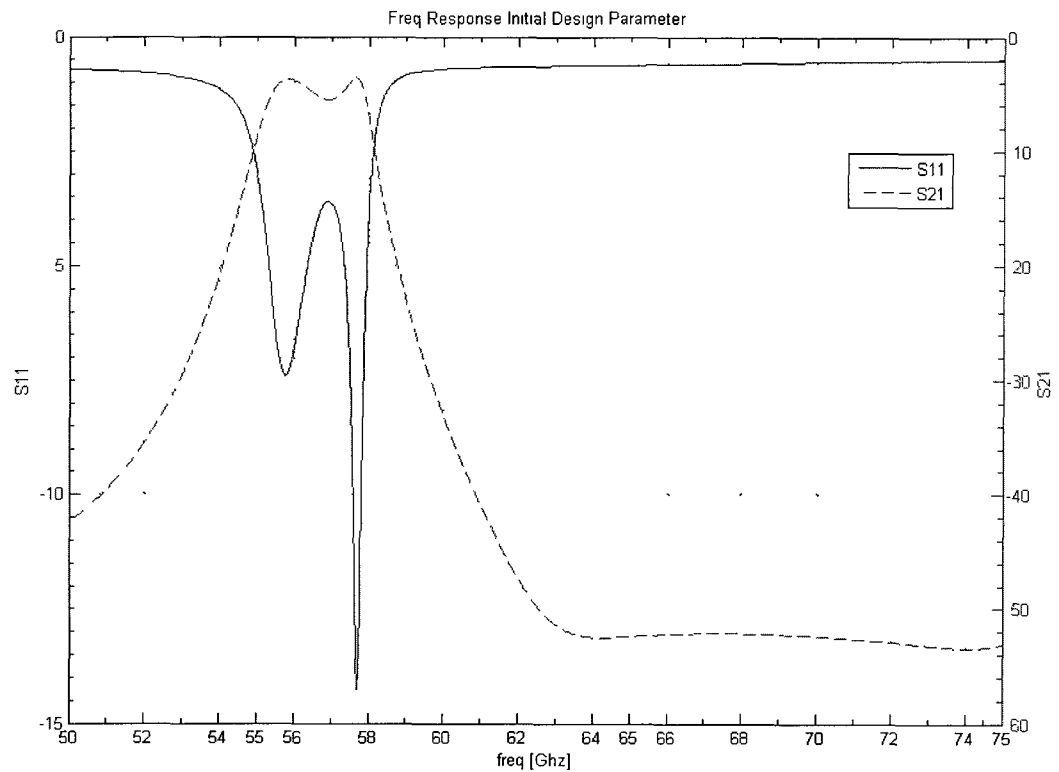
Figure 4-50 Frequency responses with initial design parameters

As seen in Fig.4-50, two peaks are visible in the insertion loss response for this filter; this is caused by using a middle cavity with a different electrical size (Cavity2 from Fig.49.) The size of the middle cavity is further optimized to compensate for this undesirable effect. The final filter design parameters are summarized in Table.21 and its frequency response shown in Fig. 4-51and Fig.4-52. In addition, the group delay responses are given in Fig. 4-53.
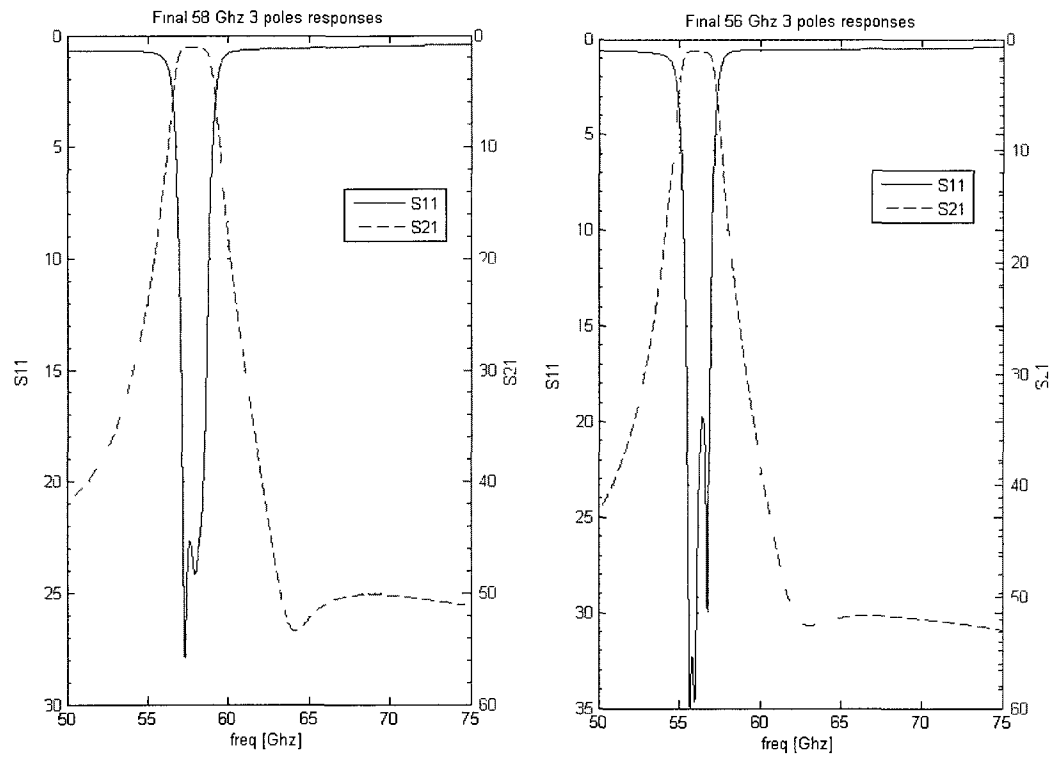
Figure 4-51 Broad frequency responses Of final 3-pole BPFs
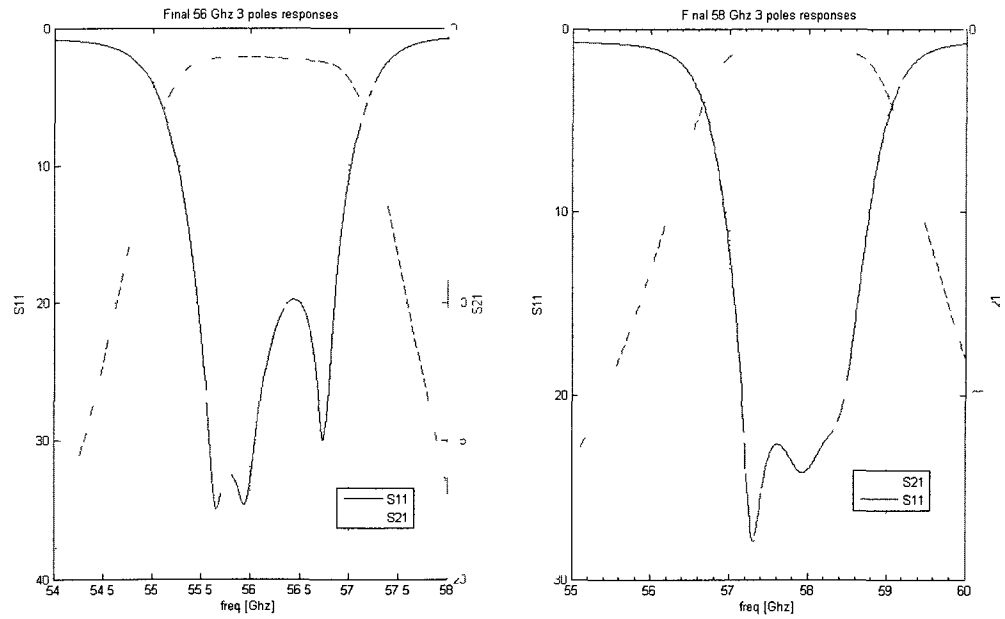
Figure 4-52 Narrow frequency responses of final 3-pole BPFs
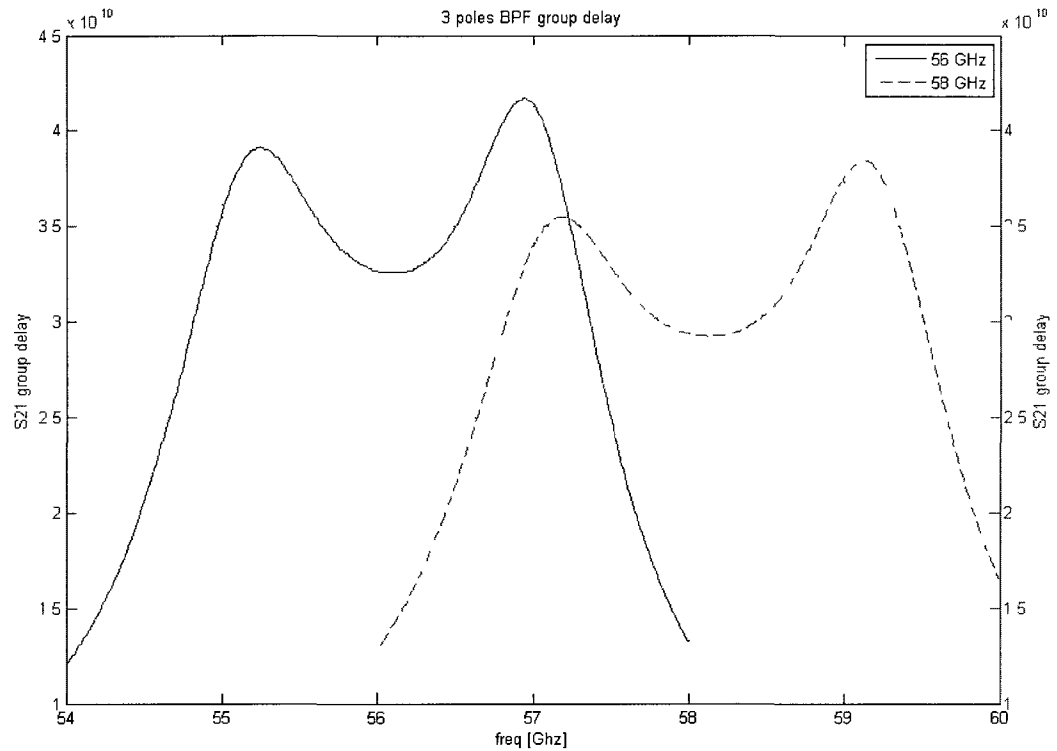
Figure 4-53 Group delay responses of final 3-pole BPFs

The cavity sizes are not identical. The middle one (cavity2) is about 5% physically larger than the other two cavities. In addition, the width of the internal slot of the 58 GHz BPF is slightly smaller than the slot for the 56 GHz BPF (0.04 mm compared to 0.05 mm) since its center frequency and FBW are different.

Both BPFs designed here exhibit a low insertion loss of approximately 1.2 dB and passband ripple better than ≤ 0.1 dB over the desired 1 GHz of bandwidth at each center frequency. Average group delay is around 400 psec in the pass band. Both filters meet the design specifications of Table 20 but the rejection specification of ≥ 42 dB at 2 GHz away from centre frequencies is not met. The BPFs have approximately -30 dB rejection at this 2 GHz offset. Higher filter orders or number of cavities would be required to achieve this stopband rejection specification.

Table 22: Final 3 poles/cavities BPF design parameters

	56 GHz	58 GHz
Cavity height	200 µm	200 µm
Cavity1 Width/Length	1.373 mm/1.47 mm	1.34 mm /1.37 mm
Cavity2 Width/Length	1.524 mm/1.38 mm	1.43 mm /1.36 mm
Cavity3 Width/Length	1.373 mm/1.47 mm	1.34 mm /1.37 mm
Feed width (*FW*) See Fig.4-49	0.146 mm	0.146 mm
Feed in width (*FIW*)	0.181 mm	0.18 mm
Feed in length (*FIL*)	0.7 mm	0.746 mm
Slot position (*SP*)	0.396 mm	0.416 mm
Slot width (*SW*)	0.248 mm	0.234 mm
Slot length (*SL*)	0.571 mm	0.576 mm
Internal slot width (*SIW*)	0.05 mm	0.04 mm
Internal slot length (*SIL*)	0.6 mm	0.63 mm
Internal slot position (*SIP*)	0.231 mm	0.288 mm

106

4.6 Five pole cavity BPF design

A similar design effort was carried out to implement five cavity/pole Chebyshev BPFs. The increased BPF order would improve LO rejection in comparison to the previous three cavities/poles filter design. Also insertion loss must be kept as low as possible. One of the biggest challenges of this design is to achieve sufficient return loss while meeting all the previously stated design requirements as most design parameters are very sensitive to small geometry variations. By keeping symmetry among the required resonators in this design, sufficient return loss is not guaranteed and resonators will require to be individually optimized.

The Chebyshev low pass prototype, discussed in Section 2.2.2 is used. All required circuit parameters can be calculated using Eqn. (2.36) and shown in Table 23. After the low pass prototype is designed, then it is frequency transformed into the desired band pass response with Eqn. (2.46) – (2.47) in Section 2.2.3. The specifications of the BPF are summarized in Table.20.

Table 23: Chebyshev low pass prototype parameters

g_0	1
$g_1 \cdot g_2$	1.7919
$g_2 \cdot g_3$	2.8978
$g_3 \cdot g_4$	2.8978
$g_4 \cdot g_5$	1.7919
g_6	1

Using equation (4.3) the coupling matrix of the 5 poles/cavities BPF can be calculated as follow:

$$\vec{M} = \begin{bmatrix} 0 & 0.01334 & 0 & 0 & 0 \\ 0.01334 & 0 & 0.1049 & 0 & 0 \\ 0 & 0.01049 & 0 & 0.01049 & 0 \\ 0 & 0 & 0.01049 & 0 & 0.01334 \\ 0 & 0 & 0 & 0.01334 & 0 \end{bmatrix} \quad (4.6)$$

Where:

$$\vec{M}_{1,2} = \vec{M}_{4,5} = \frac{FBW}{\sqrt{g_1 \cdot g_2}} = \frac{FBW}{\sqrt{g_4 \cdot g_5}}$$

$$\vec{M}_{2,3} = \vec{M}_{3,4} = \frac{FBW}{\sqrt{g_2 \cdot g_3}} = \frac{FBW}{\sqrt{g_3 \cdot g_4}} \quad (4.7)$$
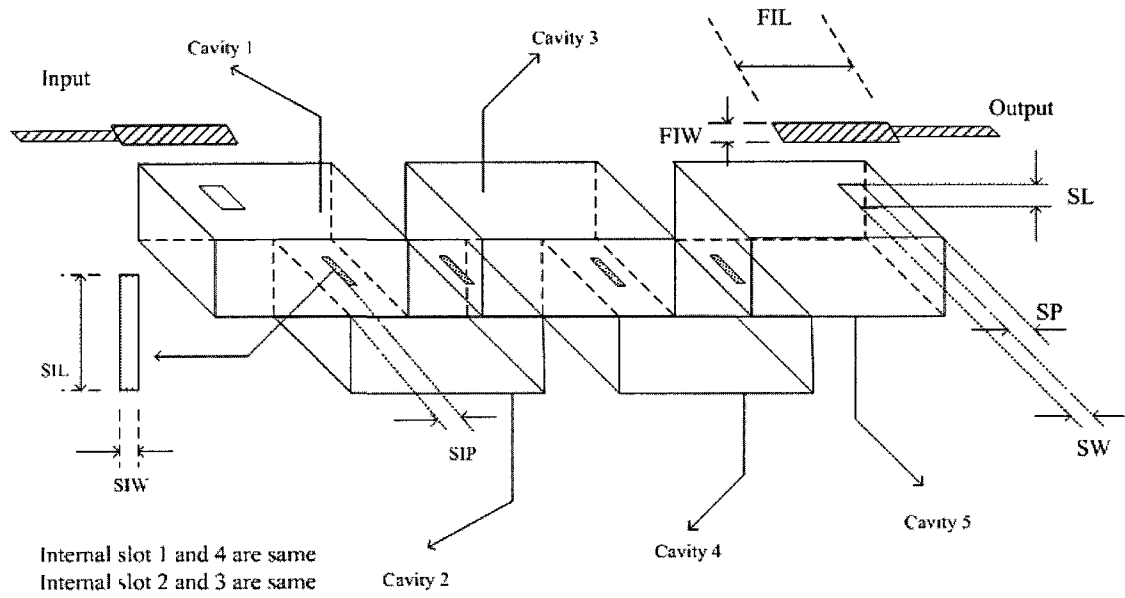
Internal slot 1 and 4 are same
Internal slot 2 and 3 are same

SW	Slot Width
FW	Feed Width
SP	Slot Position
FIW	Feed In Width
FIL	Feed In Length
SL	Slot Length
SIL	Slot In Length
SIW	Slot In Width
SIP	Slot In Position

Figure 4-54 Schematics of 5-pole/cavity BPF with design parameters

Coupling coefficients can be extrapolated from Fig.4-48, similarly to the procedure used in the implementation of the 3 pole BPF design. As expected, filter coefficients suggest a symmetrical structure is required: the internal slots 1 and 4 are identical and internal slots 2 and 3 are identical. They are initially set to be 0.07 mm and 0.05 mm respectively. Cavities 2, 3 and 4 are set slightly larger than the I/O cavities 1 and 2. Initially, the cavities were sized as shown in Table 18, i.e. cavities 1 and 5 are set to the same size as the I/O cavities of three poles BPF design and cavities 2, 3 and 4 are set to have the same size as the middle cavity as the three poles BPF design, shown in Table 22. Further optimization is carried out with full wave simulator.
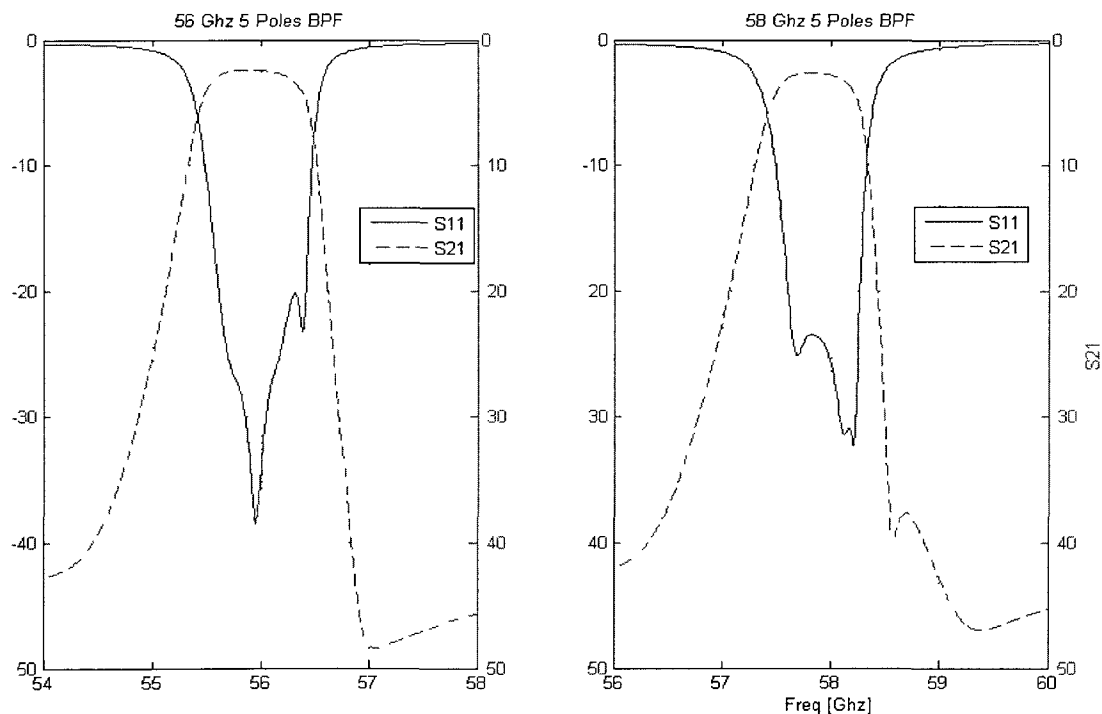
Figure 4-55 Frequency responses of 5-pole/cavity BPFs at 56 GHz and 58 GHz respectively

The optimized insertion loss of the BPFs is about 2.1 dB with a return loss better than $\leq -20\,\mathrm{dB}$. The average group delay is around 1nsec. Most importantly a 42 dB

rejection is achieved at a 2 GHz offset using the 5 poles/cavities design. Table 24 shows the achieved BPF performances compared to initial specifications.
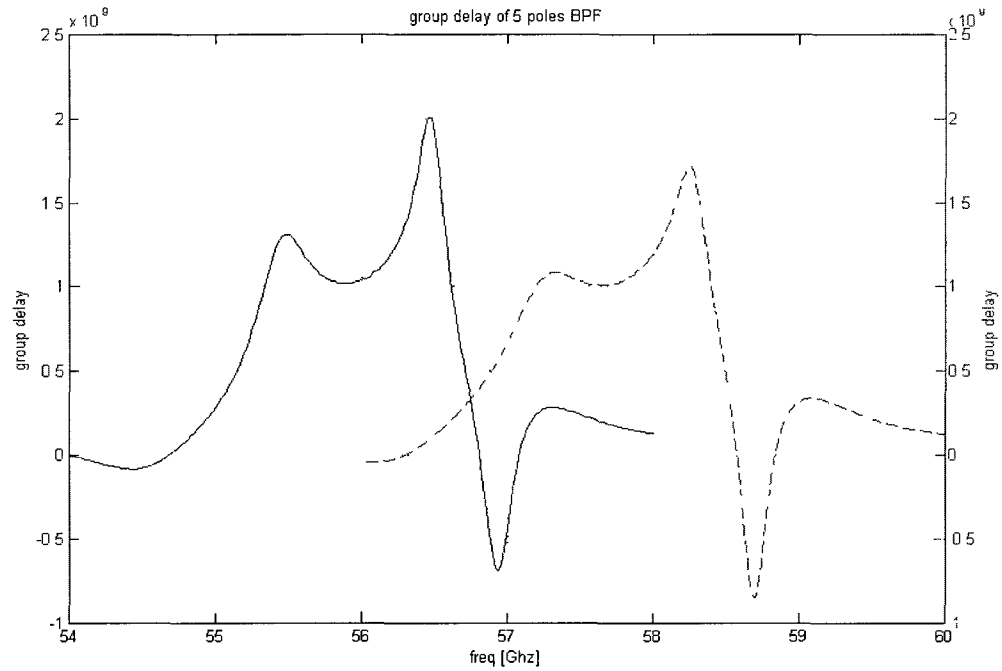
Figure 4-56 Group delay 5 poles BPFs centred at 56 GHz and 58 GHz respectively.

Table 24: Target specifications and performances of BPFs

	EM simulation	Specification
Input match S11	$\leq -20\,\mathrm{dB}$	$\leq -16\,\mathrm{dB}$
Insertion loss, IL	$\leq -2.2\,\mathrm{dB}$	$\leq -3.5\,\mathrm{dB}$
Passband flatness within 225 MHz	$\leq -0.1\,\mathrm{dB}$	$\leq -0.2\,\mathrm{dB}$
Rejections 2 GHz offset from pass band	$\leq 42\,\mathrm{dB}$	$\leq 42\,\mathrm{dB}$
Group delay	$\leq -2\,\eta\mathrm{sec}$	5 ηsec average

110

Table 25: Final 5-pole/cavity BPF design parameters

	56 GHz	58 GHz
H 56, 58 GHz	200 µm	200 µm
Cavity1 Width/Length	1.38 mm/1.477 mm	1.383 mm /1.415 mm
Cavity2 Width/Length	1.524 mm/1.391 mm	1.389 mm /1.446 mm
Cavity3 Width/Length	1.518 mm/1.391 mm	1.38 mm /1.447 mm
Cavity4 Width/Length	1.527 mm/1.392mm	1.391 mm /1.451 mm
Cavity5 Width/Length	1.477 mm/1.379mm	1.378 mm /1.419 mm
Feed width	0.146 mm	0.146 mm
Feed in width	0.181 mm	0.189 mm
Feed in length	0.724 mm	0.553 mm
Slot position	0.396 mm	0.129 mm
Slot width	0.248 mm	0.247 mm
Slot length	0.571 mm	0.571 mm
Internal slot 1 width	0.05 mm	0.08 mm
Internal slot 1 length	0.604 mm	0.532 mm
Internal slot 1 position	1.255 mm	1.202 mm
Internal slot 2 width	0.035 mm	0.03 mm
Internal slot 2 length	0.55 mm	0.514 mm
Internal slot 2 position	1.269 mm	1.179 mm
Internal slot 3 width	0.035 mm	0.028 mm
Internal slot 3 length	0.55 mm	0.511 mm
Internal slot 3 position	1.282 mm	1.179 mm
Internal slot 4 width	0.08 mm	0.07 mm
Internal slot 4 length	0.55 mm	0.525 mm
Internal slot 4 position	1.255 mm	1.212 mm

The filter's response is very sensitive to many of the design parameters used here and hence a sensitivity analysis is required. This sensitivity study is also applicable to the 3-pole BPF designs. Results are shown in Fig.4-57:
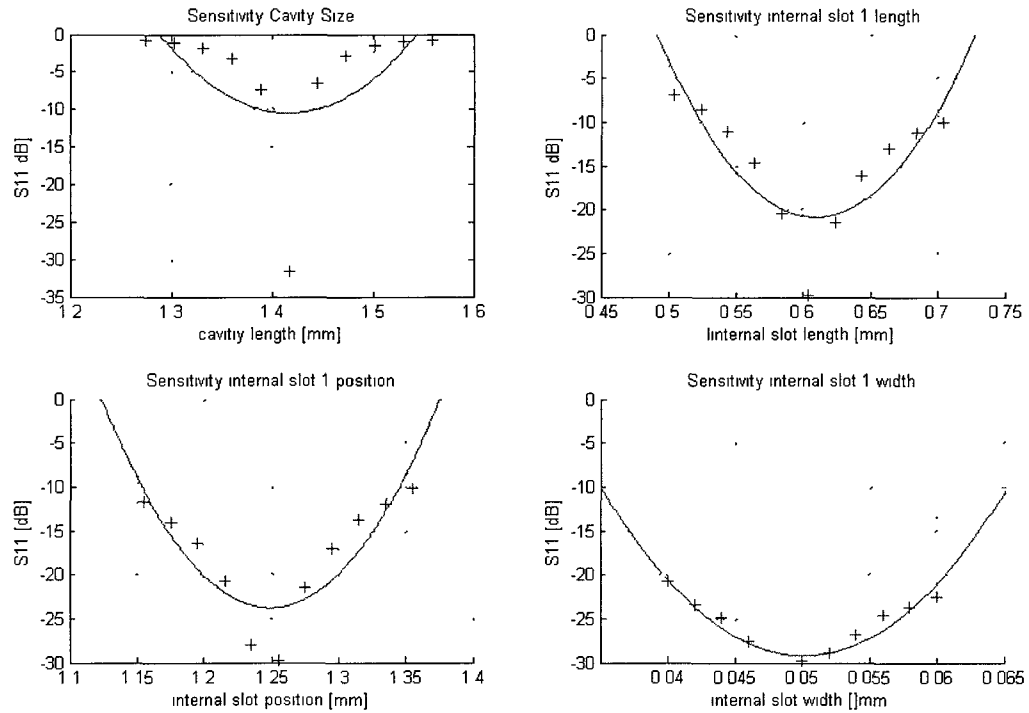
Figure 4-57 Sensitivity studies of some more important parameters.

Sensitivity studies show that the size of the cavities is the most sensitive parameter of the BPF design, followed by the length of the internal slot. Besides making the BPF very sensitive to its physical dimensions, the internal coupling slots are also too small (less than 80 μm) to be fabricated in a regular thick film process [31] and [32]. In order to separate the small internal slots from the rest of the circuit, a dummy metallization layer is included. First, a 150 μm metallization is printed from the edges of the small slot to form a 150 μm frame. Second, a reference metallization plane is fabricated to overlap the first print by 75 μm as shown in Fig. 4-58.
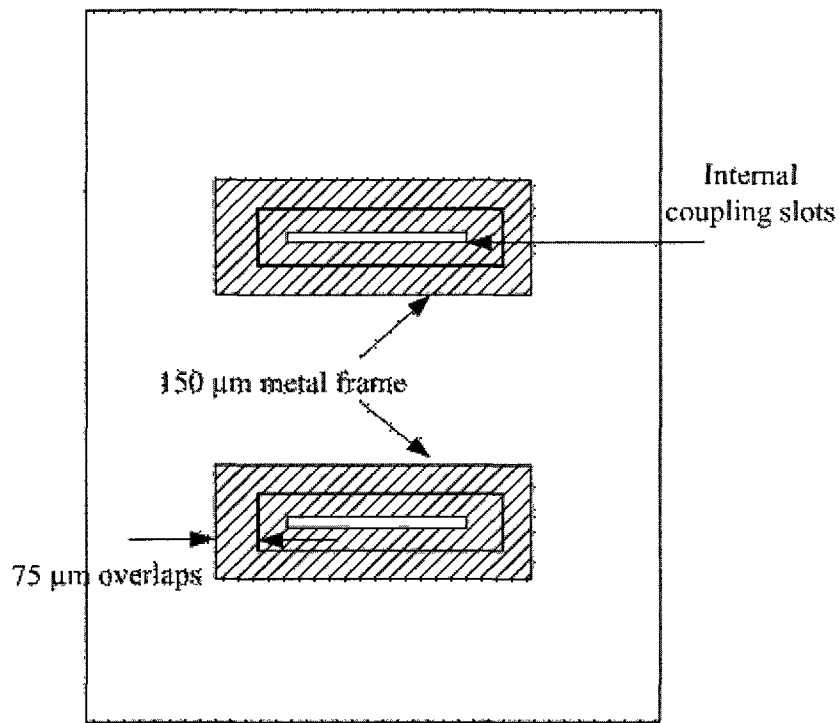
Figure 4-58 Dummy metalization layers for physically small structures such as internal coupling slots

SIW BPFs realized with LTCC have advantages over the printed BPFs with open-loop resonator structures, especially in V band frequency range. The LTCC BPF designs are three-dimensional, having more parameters to tune and optimize and allowing better matching and passband flatness to be achieved. With more poles the challenging rejection specs can be met as shown with the 5-pole design, however the trade off is insertion loss.

Table 24. indicates that all the diplexers requirements are met. However, LO rejection specification is met with zero margin, with 42 dB insertion loss at 2 GHz away from the passband. This could pose risks if the filters are operating in extreme temperatures or the BPFs experience any process variances. As mentioned in section 2.1.8, "LO nulling" techniques achieved by applying different DC bias onto the quadrature IF inputs into the image reject mixer can effectively reduce the amount of LO leakage.[8]

113

Chapter 5   Microstrip Transmission Line to

Waveguide Launcher

A diplexer is a passive device composed of three ports: a high-band BPF port, a low-band BPF port and an antenna port. The design of the BPFs for the high and low band have been discussed in detail in the previous chapters. In this chapter a microstrip to waveguide launcher is designed for the common port as a transition to the antenna. Two different implementations of the launcher will be presented, corresponding to the different configuration developed in Chapter 3 and Chapter 4.

5.1 Design Concepts and Specifications

The main objective of the microstrip to waveguide transition (launcher) at the common port of the diplexer is to transit the signal from a microstrip line into the waveguide fed antenna, which is normally mounted onto the chassis of the transceiver module. The design proposed here is a simple quarter wavelength $\frac{\lambda_g}{4}$ microstrip probe extension from the main circuit. The ground reference of this probe is removed and it is suspended above a metallic backshort. The backshort has dimensions of the appropriate waveguide, e.g. WR15 in this case [33]. The depth of the backshort is also designed to be quarter wavelength $\frac{\lambda_g}{4}$ at the centre design frequency. The principle of this launcher is quite simple. The extended probe is working as an antenna, however since its ground reference beneath the substrate is removed, the guided quasi-TEM field of the microstrip line is disturbed, and the field tends to go down towards to the back of the backshort. Since the backshort is terminated as a short and has quarter wavelength length, the quasi-TEM field from the suspended microstrip line will bounce back upwards into the waveguide which is placed directly above the suspended microstrip line.

One of the most challenging parts of the design is to accomplish a broadband launcher with a broadband match, since the simple microstrip line probe at quarter wavelength is very narrow band in nature, and definitely not enough to cover the entire 10 GHz required around the unlicensed V band frequency spectrum. Fig. 5-59 shows the general structures of the chosen microstrip to waveguide launcher. As can be seen, the input microstrip port is on the left and the output waveguide port is on the top right, with a patch launcher suspended above a backshort on the bottom right. Three main techniques are used in order to increase the operating bandwidth. The first is to adjust the dimensions of the extended microstrip length (length E). The second is to adjust the length and width of the patch launcher. The third technique is to introduce a discontinuity with a section of metallic housing (called a 'mousehole') inserted between the input and the patch launcher.

The implementation given in Fig. 5-59 (a) consists of an alumina microstrip substrate inserted into a conventional WR15 rectangular waveguide assembly. This is to allow connection with the alumina BPF/diplexer developed in Section 3.3.

The implementation illustrated in Fig. 5-59 (b) consists of a LTCC module containing a microstrip launcher and SIW waveguide backshort, assembled with the WR15 rectangular waveguide output (aligned on top of the backshort). This is to allow connection with the LTCC BPF/diplexer developed in Section 4.6.
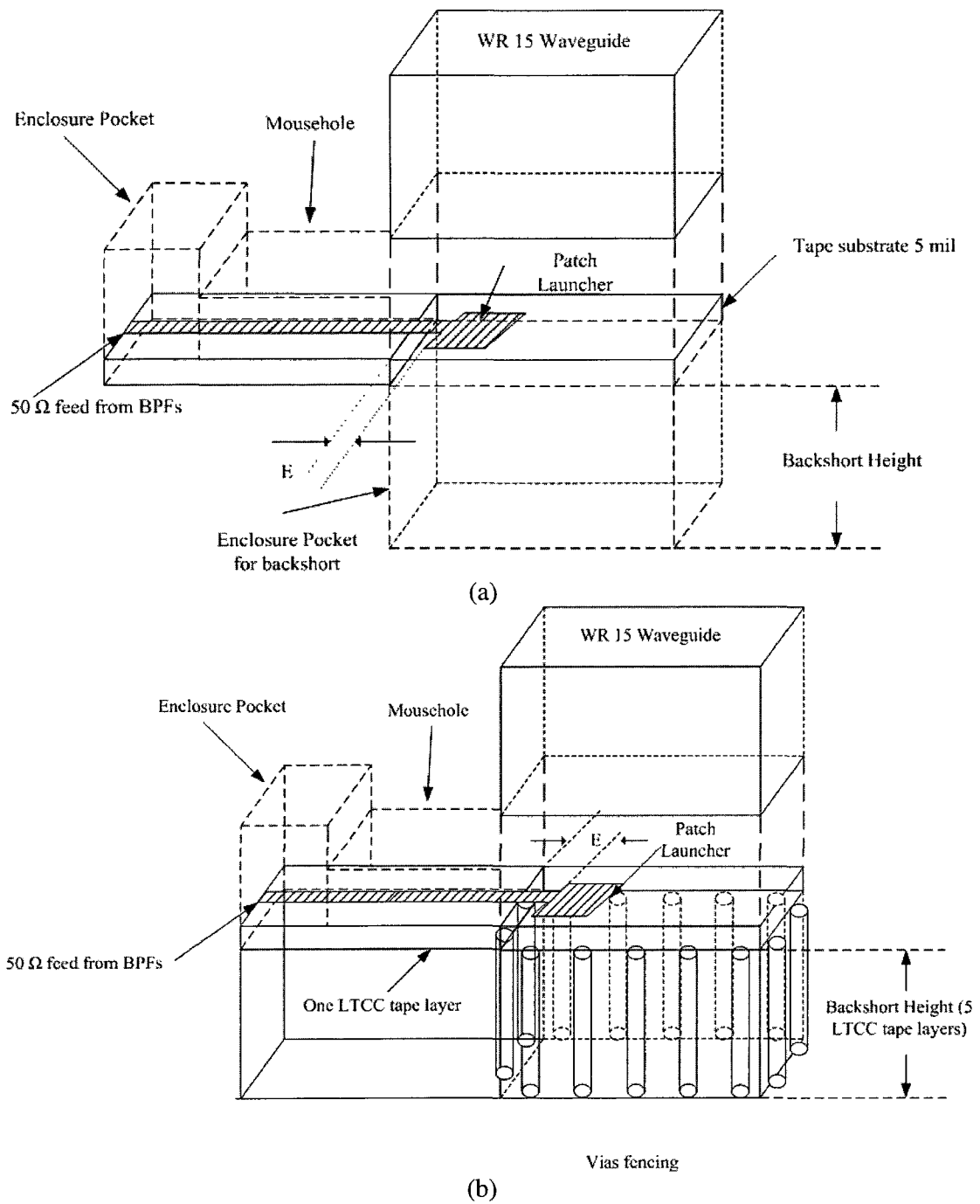
Figure 5-59 Microstrip line to Waveguide Launch with (a) Conventional alumina
substrate and (b) LTCC.

5.2   Design of the Microstrip Transmission Line Launcher

Two microstrip line to waveguide transition launcher designs are presented here. One using 99.6% alumina and the other one using Ferro A6-S LTCC. The following tables summarize the design specifications, and the dielectric properties.

Table 26: Target specifications of launchers

	Specifications
Insertion loss	$\leq 1.3\,dB$
Operation BW	$55 \sim 59\,GHz$
RL over operation BW	$\leq 14\,dB$

Table 27: Substrates properties

	Alumina	FerroA6-S
Substrate thickness, h	5 mil	100 μm
Metalization, Gold	0.1 mil	0.1 μm
Surface roughness	2 μ inch	N.A.
Pull back	2 mil	50 μm
ε_r	9.90	5.90
$\tan \delta$	0.0002	0.0020
Track tolerance	$\pm \dfrac{1}{5}\,mil$	$\pm 2\,\mu m$

As explained in the previous section, most of the design parameters require a quarter wavelength, corresponding to about 19 mil with alumina, and 590 μm with LTCC with Ferro A6 tape. The differences in material properties between the alumina and

117

LTCC design are accounted for in the backshort as well the space between the probe and the WR-15 waveguides differs in both design implementations The backshort of the alumina design launcher is air-filled, while the wall of the backshort is gold plated. Since this is part of the metal enclosure of the module, it can be considered as a perfect conductor. On the other hand, in the LTCC design, the backshort can be either dielectric filled or air-filled depending on whether a pocket or a cavity has been drilled from the dielectric tape layers. In this design, the backshort is dielectric filled and its backshort wall is formed by row of via fencing.

- In the alumina design, the length and width of the patch extension is initially set to 30 mil since the extended substrate is suspended and its ground reference is no longer 5 mil below the signal but at bottom of the backshort. Therefore, a value 30 mil is chosen between the $\frac{\lambda_0}{4} = 49$ mil and $\frac{\lambda_g}{4} = 19$ mil .The height of backshort is set to be 49 mil. As explained before, a mousehole is used to achieve a broader match [35] and its height is initially set to match the cavity height of 30 mil . Both the length and extended line length are initially set to 100 mil and 0 mil respectively.

- In the LTCC design, the length and the width of the patch extension is set to be 900 μm. Recall that the above the backshort, the ground reference is about 600 μm below the signal and the corresponding MS line with $Z_0 = 50 \, \Omega$ line (return ground is 600 μm below) is set to 1 mm. The height of backshort is set to be 500 μm or the equivalent of a 5 tape layers height since the $\frac{\lambda_g}{4} \approx 544 \, \mu m$. The 'mousehole' height is set same to the cavity height 1.27 mm in the beginning and its length is set to be 1 mm. Finally, the extended line length is set to be 0 mil.

After EM optimization was completed, the final dimension of both design are summarized in Table.28.

Table 28: Final design parameters of the launchers

	Alumina	LTCC
Waveguide A length	148 mil	3.77 mm
Waveguide B length	74 mil	1.88 mm
Microstrip line extended length, E	6 mil	0.209 mm
Microstrip line extended width	4.7 mil	56 μm
50 Ω line width	4.7 mil	0.146 mm
Patch width	27.5 mil	0.717 mm
Patch length	30 mil	1.916 mm
Backshort length	43 mil	500 μm
Mousehole height	20 mil	1.85 mm
Mousehole length	72 mil	0.7 mm
Cavity pocket height	30 mil	1.27 mm

The alumina launcher design achieves a broader match compared to the LTCC design. The main reason is that the backshort of the alumina launcher can be precisely controlled by adjusting the dimension of the module enclosure, however, in the LTCC design the size of the backshort is controlled by the number of tape layers it occupies (a multiple of 100   m). In this particular design the backshort is set to be 5 tape layers or 500 μm. Also, the metallic wall formed by via fencing is not perfect, making it easy for E and H fields to leak and this inhomogeneous structure would resemble a discontinuity between the regular microstrip transmission line and the reference removed microstrip line extension and hence increasing the difficulties of matching more difficult than with the alumina design.

(a)

(b)

120

(c)
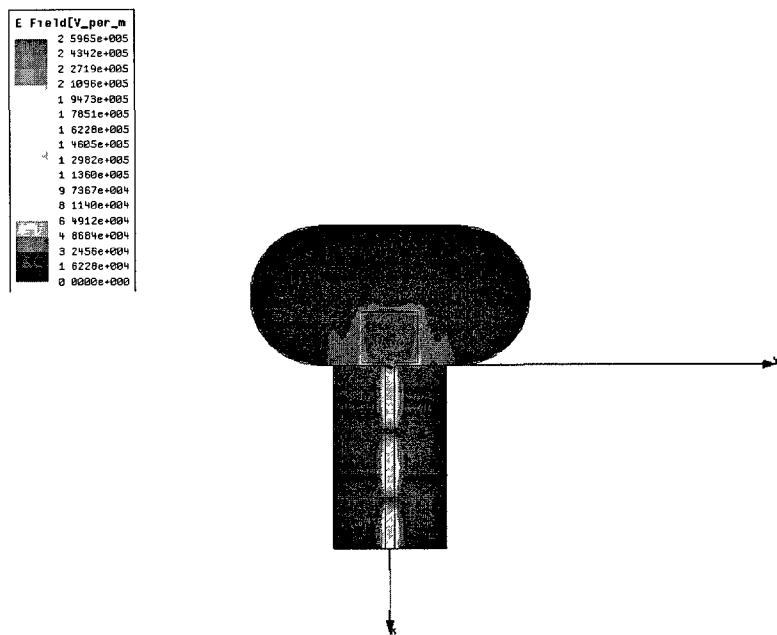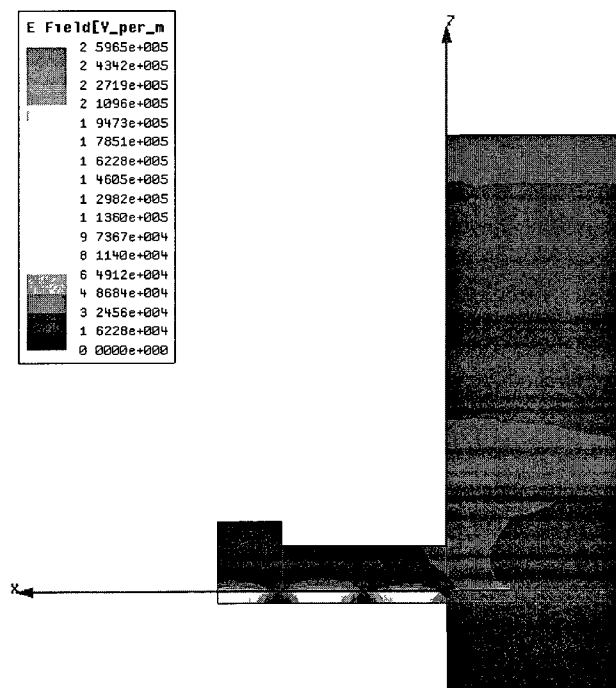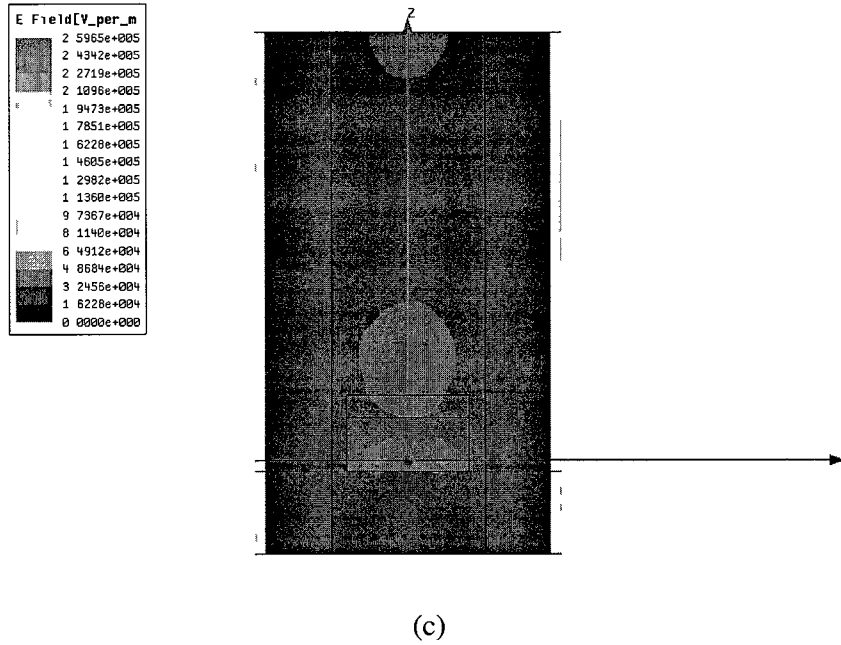
Figure 5-60 E fields of the LTCC launcher (a) X-Y plane (b) X-Z plane and (c) Y-Z plane

The simulated E-fields show the concept of signal transit topology. Energy is being built up and radiated by the patch around the waveguide as shown in Fig.5-60 (a). The field disturbances at the discontinuity are clearly shown at one particular frequency, from the X-Y plot, the standing-wave is formed along the transmission line. Once the TL enters the backshort and waveguide, E fields being building up at edges, while still maintaining a relatively good match. The X-Z and Y-Z plots of the E fields clearly show that the electrical energy being launched upwards Fig.5-60 (b) (c).

Both deigns had achieve acceptable matching over the required design frequency 55 ~ 59 GHz. Furthermore, the alumina design achieves a return loss better than ≈ -14 dB over the entire unlicensed V band (56 GHz to 66 GHz) . Finally, the expected insertion loss of the launchers is approximate 0.4 dB and 0.7 dB for the alumina and LTCC designs respectively. All design specifications shown in Table.25. were met.

A sensitivity study of the launcher designs was also performed. The dimensions of the patch are the most sensitive parameters in the design. The length of the patch and the

amount of extension are the two most sensitive design parameters. Both of these parameters are along the direction of the microstrip transmission line. In addition, from Fig.5-62. the S11 response as a function of variations in the height of mouse hole has an opposite response (different gradient) as the rest of design parameter at the particular simulation frequency, This is a handy parameter for achieving a broader match [35].

Launcher AIO

S11 **S21**

Freq [Ghz]

(a)
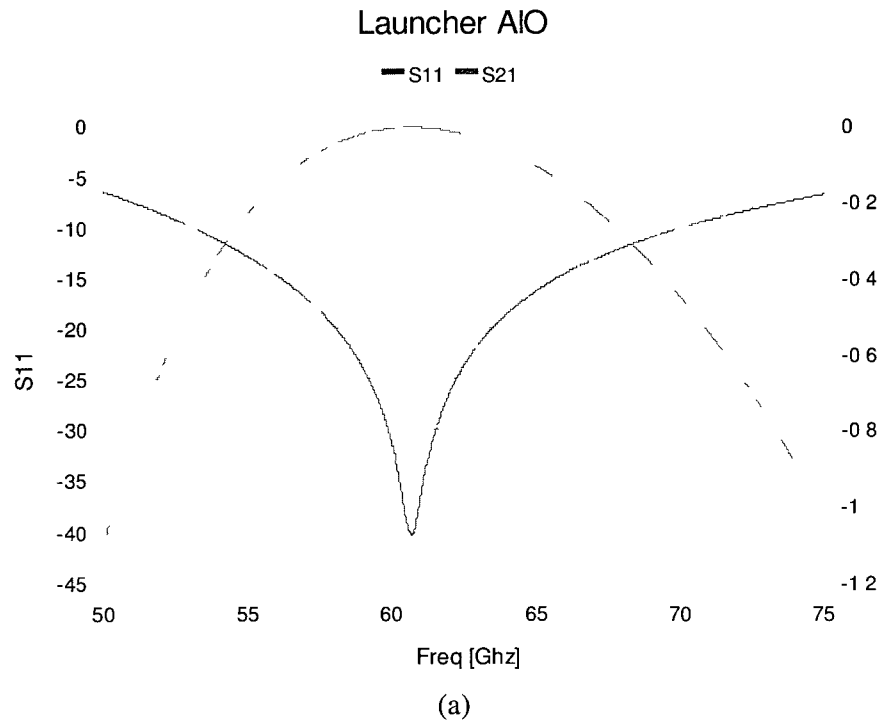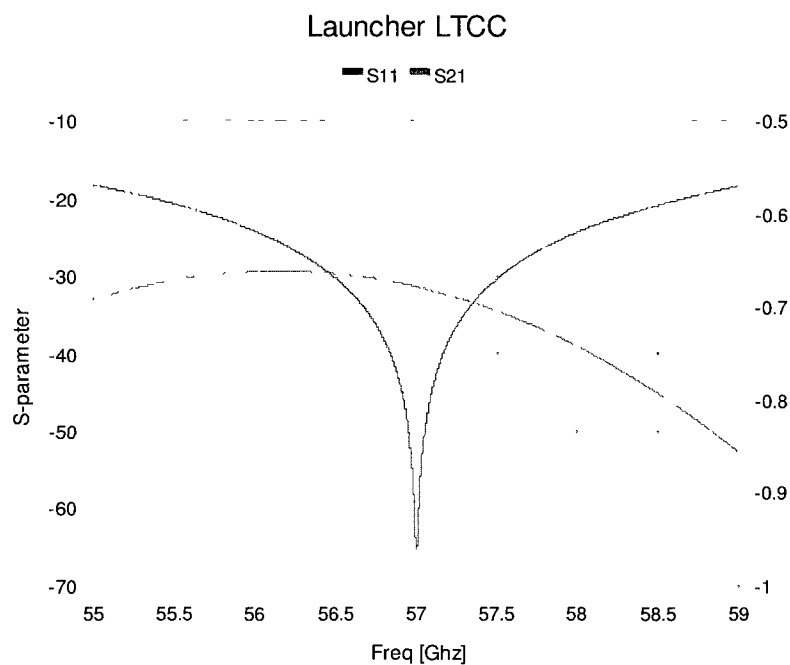
(b)

Figure 5-61 S parameters (a) Launcher design with Alumina (b) with LTCC
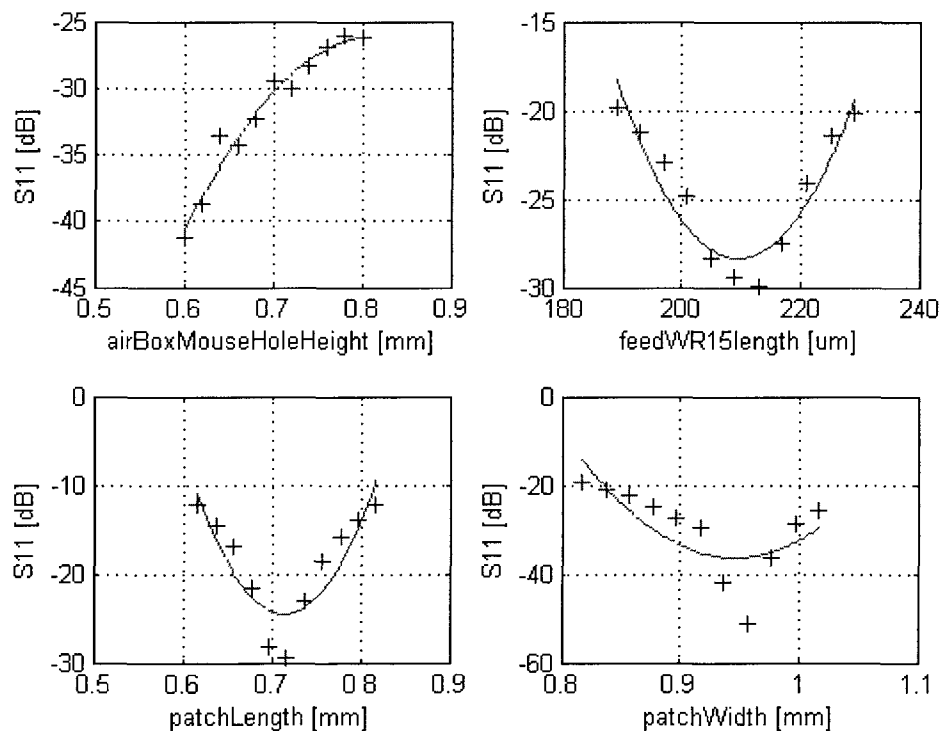
Figure 5-62 Sensitivity study of the launcher design parameters

5.2.1 Measurements of alumina microstrip transmission line to waveguide launcher

The alumina launcher designed in the previous section was built onto a metal enclosure with pocket cavities to accommodate a WR15 waveguide on the top cover above the launcher. The backshort is realized onto the carrier enclosure where the launcher is placed.

Due to limitations of the measurement completed at V band frequency, only one port S parameter is measured, with the input of the launch terminated with 50 Ω load, and also using two 10 dB attenuation pads. From the measurements, the insertion loss and return loss of the launcher can be calculated. Figure Fig.5-63 illustrates the test setup used.

The calibration of the system is carried out by setting a reference point where all incident power is reflected by a short connection at the through port of the directional coupler. The maximum reflected power is picked up by the coupled port of the directional coupler to the scalar analyzer. This set of measurement is stored and set as nominal (maximum) reflected power. Then the DUT is connected and the ratio of the DUT reflected power to the nominal reflected power is the return loss of the launcher.
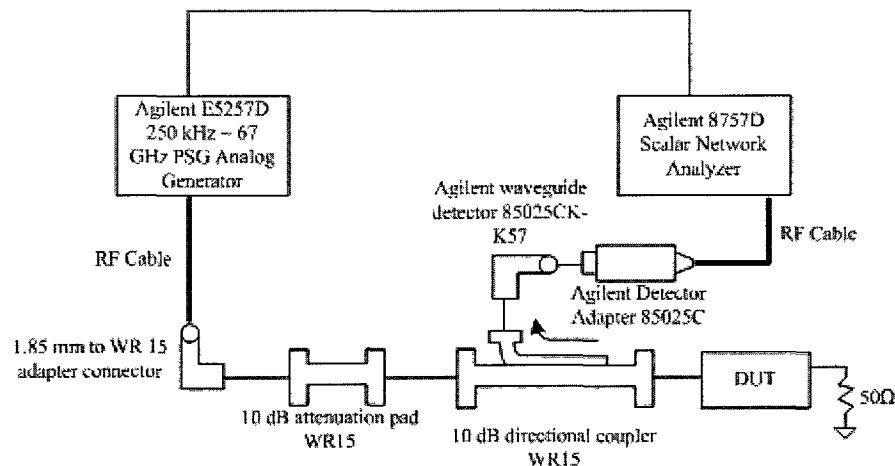
Figure 5-63 Launcher measurement setup

The measured frequency band is set to 47 GHz to 67 GHz due to the source limitations of the sweep generator. The insertion loss is calculated based on measured return loss using Eqnation (5.1): assuming other losses are negligible.

$$\text{Insertion Loss}^{\text{approximate}} \approx 10 \cdot \log\left(1 - 10^{\frac{\text{Return Loss}}{10}}\right) (5.1)$$
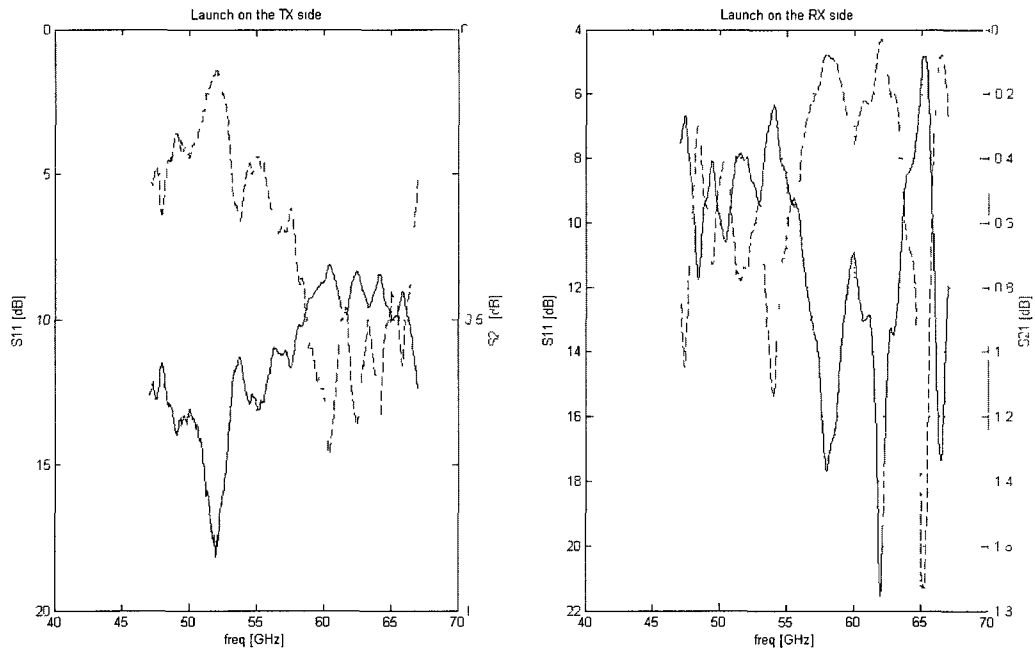
Figure 5-64 Alumina launcher measurement

Overall, the measured performance of the microstrip to waveguide launcher is acceptable, considering all the process and built variances and the measurement setup constraints / difficulties experienced during manufacturing and assembly.

The measurements achieve a acceptable match over 47 GHz to 67 GHz frequency range with a return loss better than 8 dB , looking into the waveguide port. Discrepancies between simulations and measurements are caused by frequency limitations in the 50 termination at V band frequency. A single layer 50Ω microwave resistor chip attached using a double bond-wired at the microstrip line input adds parasitic inductance, degrading the accuracy of the 50 . termination, especially over a broader frequency

125

range. Also, the design requires precise mechanical placement as suggested by the sensitivity studies, particularly the required amount of extension of the microstrip transmission line into backshort is only 6 mil, exceeding the accuracy that could be achieved by using hand placement. This misalignment will contribute to mismatch.

The importance of the mechanical placement is shown with the two measurements in Fig.64. Both the TX and RX launchers have used an identical design, but due to the inconsistencies during assembly and manual placement, their frequency responses are quite different. On the TX side, the return loss minima happens at around 52.5 GHz which is off centered from the 60 GHz simulated centre frequency. This discrepancy is most likely due to bad mechanical placement and bad terminations at high frequencies, but it maybe also due to the increase of dielectric constant at high frequencies. On the RX side, the minima happens at around 60 GHz, which is consistence with simulations, however the response exhibits multiple frequency notches and the return loss is poor over the 65 GHz range. Again, these degradations are due to poor mechanical alignment and in this particular case, there is a bad epoxy over flow problem, this over flow will cause the extension to become longer than designed for as the conductive epoxy will prolong the ground reference close to the opening of the backshort, disturbing this critical and sensitive design parameter.
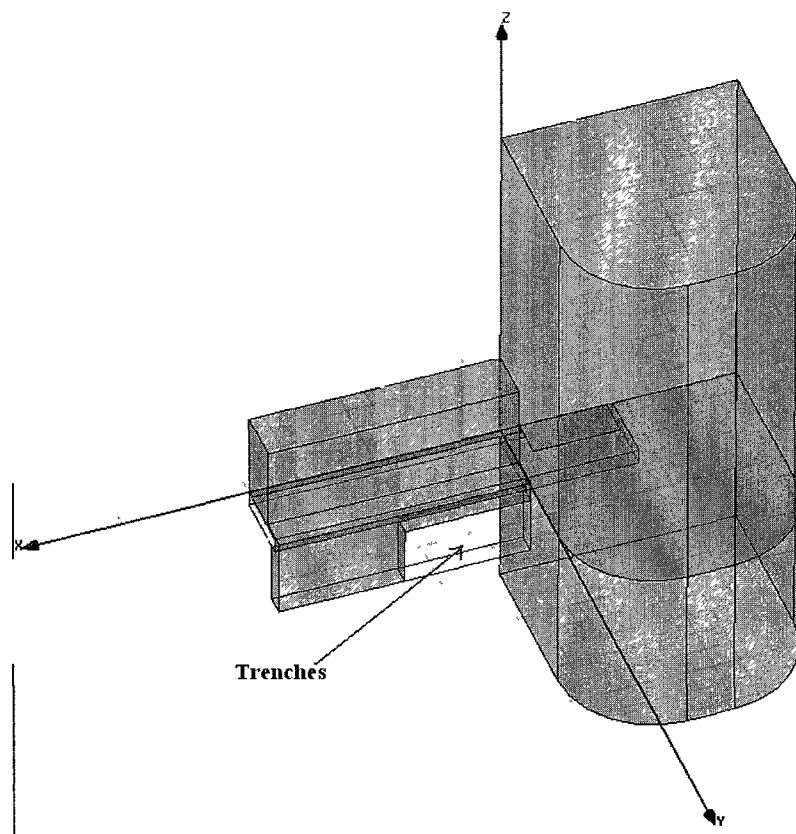
Figure 5-65 HFSS model with mechanical invariance, pedestal and trenches

In addition to the placement problem, there are two gaps or trenches created due to the fact that the microwave section is built onto a pedestal used to bring the microwave sub-carriers (MMICs in dotted boxes shown in Fig.2-7) level to the other 'lower frequency' circuits multi-layer PCB. Even through these trenches are very small, 23 mil depth and around 4 mil widths, they support higher modes. In this case, the trenches and other dimensions of the launcher (shown in Fig5.65) create resonances at around 63 GHz. Since the TX line-up has moderate gain at 63 GHz [17] [18] the module will actually oscillate at 63 GHz because of this mechanical problem. The launcher design in HFSS was modified and re-simulated to verify the effects of the mechanical invariances.
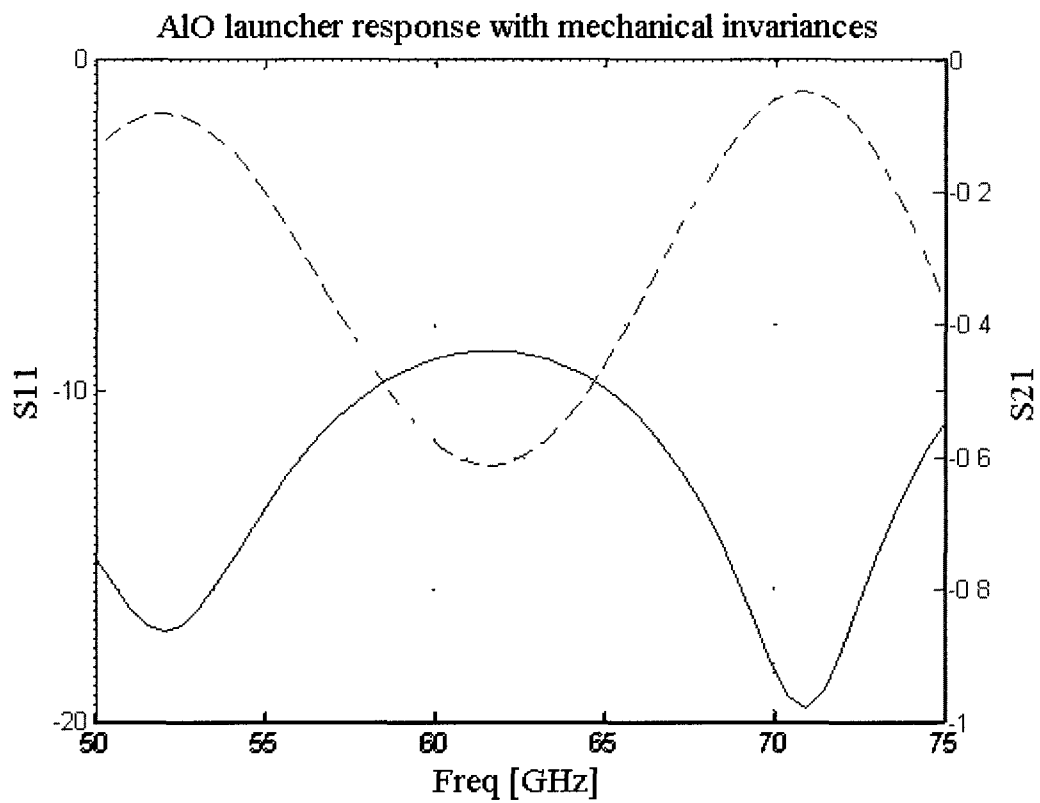
Figure 5-66 Responses of Al$_2$O$_3$ launcher with mechanical problems

Overall, the measured performance of the microstrip line to waveguide launcher is acceptable, considering all the process and built variances and measurement setup constraints / difficulties experienced during manufacturing/assembly. Lastly, the notch in the passband was corrected by filling it with silver epoxy adhesive. This effectively removed any resonance at the 65 GHz range.

Chapter 6   Summary, Conclusions and Future work

6.1 Summary

The development of diplexers in a microwave transceiver for high data rate wireless communication link has been investigated in this thesis. A point-to-point communication link operating at V-band frequencies and which breaks the Gb/s barrier was studied based on the latest ETSI regulations. These regulations were later developed into radio / transceiver specifications. A simple single LO full-duplex architecture was proposed to achieve the required specifications. This simple transceiver architecture consists of only seven active COTS components. The transceiver was later built and TX and RX modules tested separately. Requirements for the TX and RX line-ups were met and measurements were discussed. Based on the TX and RX measured performance, a set of diplexers specifications were calculated to achieve the target communication link performances.

Due to the narrow-band (225 MHz channel BW) communication link and full-duplex operation, the diplexers need to have very selective BPFs to separate the TX and RX channels as well as the spurious rejections. There were two types of BPFs proposed and developed in this thesis. Firstly, the printed version of BPF was studied. The advantages of printed BPF are: easy to build, easy to tune, easy to implement when compared to the rest of the circuit and also inexpensive to fabricate. Open-loop-resonator structures were used to realize the BPFs described here. There are two advantages of using open-loop-resonator structure; 1) their compact size compared to the regular $\frac{\lambda_g}{2}$ microstrip line resonators and 2) open-loop-resonator can realize both electrical and magnetic couplings by solid sides and opening sides of the resonators in direct proximity. Traditional microstrip line resonators with edge coupling can only achieve electrical coupling. The ability to achieve both electrical and magnetic coupling in cross-coupled resonators, allows for the implementation of pseudo-elliptic BPF, which offers higher rejections at stop-bands compares to Chebyshev BPFs.

There were two types microwave substrate considered. Firstly, 99.6% alumina substrate is considered. Its main advantage is due to its low loss at microwave frequencies. However, alumina substrates are very hard and brittle, so via hole and multilayer designs are not possible to achieve. The second substrate is Duroid 5880. This substrate also has low substrate loss at microwave frequencies, but Duroid 5880 has non-uniform z-direction thermal extensions. Multilayer circuitry is not possible.

Due to high dielectric constant of alumina, the resulting width for a microstrip with 50 Ω is wide in comparison to the side of the open-loop-resonator at V band frequencies. As a result, a 4th order open-loop-resonators BBF centred at 13.75 GHz was designed to use in the LO line-up as shown in Fig.5. Its purpose is to block any unwanted signals from entering the mixer. Firstly, an open-loop-resonator ,with optimally mitered and chamfered with tape coupling, was designed to have high Q and desired resonate frequency, a 4th order pseudoelliptic response filter was designed and realized based on its low-pass prototypes. The final alumina LO filter has low insertion loss around 1 dB at passband, the maximum passband ripple is around the 0.2 dB and the input return loss is better than -15 dB. The rejection out of band is more than 30 dB.

A similar design topology was used to design a 6 order BPF at V band frequency using Duroid substrates. The insertion loss is very high at 7 dB and the stop-band rejection at 2 GHz offset was around -40 dB and low and high side. The insertion loss and stop-band rejection specifications were not successfully met due to weak couplings required to realize narrow pass band, which also contributed to high insertion loss. The small FBW centered at V band frequencies also made the open-loop-resonator structures difficult to meet the targeted specifications. Small FBW requires high Q resonators and the position of the attenuated poles had to be placed very close to the passband. Very precise tunings were required to be able to control the pole location.

In addition to the printed BPFs, two SIW BPFs were developed in a LTCC process. SIW with Ferro tape layers were designed to resonate at TE_{101} mode at 56 GHz and 58 GHz respectively. The unloaded Q of these SIW was around 670. A quarter wave, opened circuit slot coupling structure was designed, requiring an additional tape layer

above the SIWs. The amount of coupling can be fine-tuned by adjusting the size and position of the coupling slots between adjacent SIW resonators. Two 3rd order Chebyshev responses BPF were designed and centered at 56 GHz and 58 GHz based on direct coupling. The insertion loss of both filters was 1.2 dB while the passband ripple was kept under 0.1 dB. The input return loss for both designs is better than ≤ 20 dB across the passband. The stop-band rejection of the 3rd order BPFs was well balanced over both lower and upper sides, 30 dB at 2 GHz away from the passband edges. It did not however meet the diplexers design specification of 41.7 dB for LO rejection. Additional LO rejection can be achieved by controlling the DC offset of the input I Q IF signals at mixer input effectively reducing LO leakage. The insertion loss of the microstrip transmission line to waveguide transition was not considered (it will add about 1 dB at the LO frequencies) . A second design based on a 5th order BPFs was designed to meet all specifications. A Similar set of Chebyshev direct coupled BPFs implemented using five SIW cavities were designed and optimized. The insertion loss of the 5th order SIW filters was less than 3 dB at across the band, with a minimum insertion loss at 2.1 dB and nominal at 2.5 dB. The return loss was well matched and better than ≤ 20 dB . The stop-band rejections 2 GHz away at both lower and higher sides of the passband were more than 45 dB. All spurious rejection requirements and the isolation specification were met. Since the two BPFs achieved 2.5 dB insertion loss, the microstrip transmission line from the outputs of the BPFs to waveguide transition launch would need to have less than 1 dB insertion loss to achieve the diplexers specification.

Two microstrip line to waveguide transition launchers were designed based on alumina substrate and LTCC. Both designs were based on the re-bounce of the wave from the quarter-wave-length open-circuit transmission line to the quarter-wave-depth backshort beneath the transmission line. The realizations of the launchers were very similar with the exception that the alumina backshort was manufactured on a solid aluminum carrier while the backshort of the LTCC launcher was built by having via fences as walls enclosed into 5 dielectric LTCC layers. A few techniques were used to extend the bandwidth of the launchers. One such technique introduces a "mousehole" with a probe at the end of the transmission line. The bandwidths of the alumina and LTCC launchers were 55 GHz to 69 GHz and 55 GHz to 59 GHz respectively (for a

Return Loss of 14 dB or better). The main reason of achieving a broader design with alumina was the ability to tune the depth of backshort, where in the LTCC design the size of backshort was limited to an integer multiple of the dielectric layers height (e.g. 100 μm). Lastly, the insertion loss of the launchers was kept under 0.8 dB across the entire bandwidth.

All the diplexers specifications for a multi-Gbps point-to-point communication link were achieved by the aforementioned BPFs and launchers designs.

6.2 Conclusions and Contributions

1) A multi- Gb/s, V-band link was studied based on the latest ETSI regulations, leading to precise required radio / diplexer specifications.

2) A diplexer implemented on LTCC substrate can be an excellent replacement for its bulky and expensive waveguide counterpart. Such a design has been presented in this thesis.

3) Planar open-loop resonator BPFs have been designed and have shown limitations at V-band frequencies.

4) The planar open-loop resonator BPFs are more suitable for lower microwave frequencies (Ku band).

5) Two microstrip line to waveguide (WR 15) launchers have been proposed in this work. A planar design has shown better bandwidth and insertion loss performance compared to a LTCC based design. However it is vulnerable to any mechanical variances/tolerances.

6) Transceiver module measurements have shown promising results. More importantly they meet the proposed system specification.

6.3 Future Work

Future work should include building and measuring the designed BPFs and integrating the design diplexer within the microwave module. With the front end modules and

modems, a 60 GHz link could be set up and various system modulation modes can be tested.

It is also desired to develop a single LTCC multi-chip module (MCM) with the entire active and passive components developed and integrated within it. The advantages of an MCM are its compactness, low cost and potential integration which will avoid mechanical errors. Since the thin film process of LTCC can achieve accuracy of 80 μm or 3 mils, it is very difficult to have machines that can place components/parts with 3 mils tolerance.

Finally it would be advantageous to develop a pseudoelliptic response LTCC BPF to increase the attenuation by introducing transmitting zeros around the passband. However, the current LTCC SIW coupling mechanism needs to be adjusted to support cross coupling between cavities/resonators.

Appendix A

Table. A.1. Element values for a Butterworth low pass prototype filter

Value for n											
1	2 0000	1 0000									
2	1 4140	1 4140	1 0000								
3	1 0000	2 0000	1 0000	1 0000							
4	0 7654	1 8480	1 8480	0 7654	1 0000						
5	0 6180	1 6180	2 0000	1 6180	0 6180	1 0000					
6	0 5176	1 4140	1 9320	1 9320	1 4140	0 5176	1 0000				
7	0 4450	1 2470	1 8020	2 0000	1 8020	1 2470	0 4450	1 0000			
8	0 3902	1 1110	1 6630	1 9620	1 9620	1 663	1 1110	0 3902	1 0000		
9	0 3473	1 0000	1 5320	1 8790	2 0000	1 8790	1 5320	1 0000	0 3473	1 0000	
10	0 3129	0 9080	1 4140	1 7820	1 9750	1 9750	1 7820	1 4140	0 9080	0 3129	1 0000

Table. A.2. Element values for a Chebyshev low pass prototype filter

Value for n										
0 01 dB ripple										
1	0 0960	1 0000								
2	0 4488	0 4077	1 1007							
3	0 6291	0 9702	0 6291	1 0000						
4	0 7128	1 2003	1 3212	0 6476	1 1007					
5	0 7563	1 3049	1 5773	1 3049	0 7563	1 0000				
6	0 7813	1 3600	1 6896	1 5350	1 4970	0 7098	1 1007			
7	0 7969	1 3924	1 7481	1 6331	1 7481	1 3924	0 7969	1 0000		
8	0 8072	1 4130	1 7824	1 6833	1 8529	1 6193	1 5554	0 7333	1 1007	
9	0 8144	1 4270	1 8043	1 7125	1 9057	1 7125	1 8043	1 4270	0 8144	1 0000
10	0 8196	1 4369	1 8192	1 7311	1 9362	1 759	1 9055	1 6527	1 5817	0 7446	1 1007
0 1 dB ripple										
1	0 3052	1 0000								
2	0 8430	0 6220	1 3554							
3	1 0315	1 1474	1 0315	1 0000						
4	1 1088	1 3061	1 7703	0 8180	1 3554					
5	1 1468	1 3712	1 9750	1 3712	1 1468	1 0000				
6	1 1681	1 4039	2 0562	1 5170	1 9029	0 8618	1 3554			
7	1 1811	1 4228	2 0966	1 5733	2 0966	1 4228	1 1811	1 0000		
8	1 1897	1 4346	2 1199	1 6010	2 1699	1 5640	1 9444	0 8778	1 3554	
9	1 1956	1 4425	2 1345	1 6167	2 2053	1 6167	2 1345	1 4425	1 1956	1 0000
10	1 1999	1 4481	2 1444	1 6265	2 2253	1 6418	2 2046	1 5821	1 9328	0 8853	1 3554
0 2 dB ripple										
1	0 4342	1 0000								

|											
2	1 0378	0 6745	1 5386								
3	1 2275	1 1525	1 2275	1 0000							
4	1 3028	1 2844	1 9761	0 8468	1 5386						
5	1 3394	1 3370	2 1660	1 3370	1 3394	1 0000					
6	1 3598	1 3632	2 2394	1 4555	2 0974	0 8838	1 5386				
7	1 3722	1 3781	2 2756	1 5001	2 2756	1 3781	1 3722	1 0000			
8	1 3804	1 3875	2 2963	1 5217	2 3413	1 4925	2 1349	0 8972	1 5386		
9	1 3860	1 3938	2 3093	1 5340	2 3728	1 5340	2 3093	1 3938	1 3860	1 0000	
10	1 3901	1 3983	2 3181	1 5417	2 3904	1 5536	2 3720	1 5066	2 1514	0 9034	1 5386
5 dB ripple											
1	0 6986	1 0000									
2	1 4029	0 7071	1 9841								
3	1 5963	1 0967	1 5963	1 0000							
4	1 6703	1 1926	2 3661	0 8419	1 9841						
5	1 7058	1 2296	2 5408	1 2296	1 8058	1 0000					
6	1 7254	1 2479	2 6064	1 3137	2 4758	0 8696	1 9841				
7	1 7372	1 2583	2 6381	1 3444	2 6381	1 2583	1 7372	1 0000			
8	1 7451	1 2647	2 6564	1 3590	2 6964	1 3389	2 5093	0 8796	1 9841		
9	1 7504	1 2690	2 6678	1 3673	2 7239	1 3673	2 6678	1 2690	1 7504	1 0000	
10	1 7543	1 2721	2 6754	1 3728	2 7392	1 3806	2 7231	1 3485	2 5239	0 8842	1 9841

Appendix B
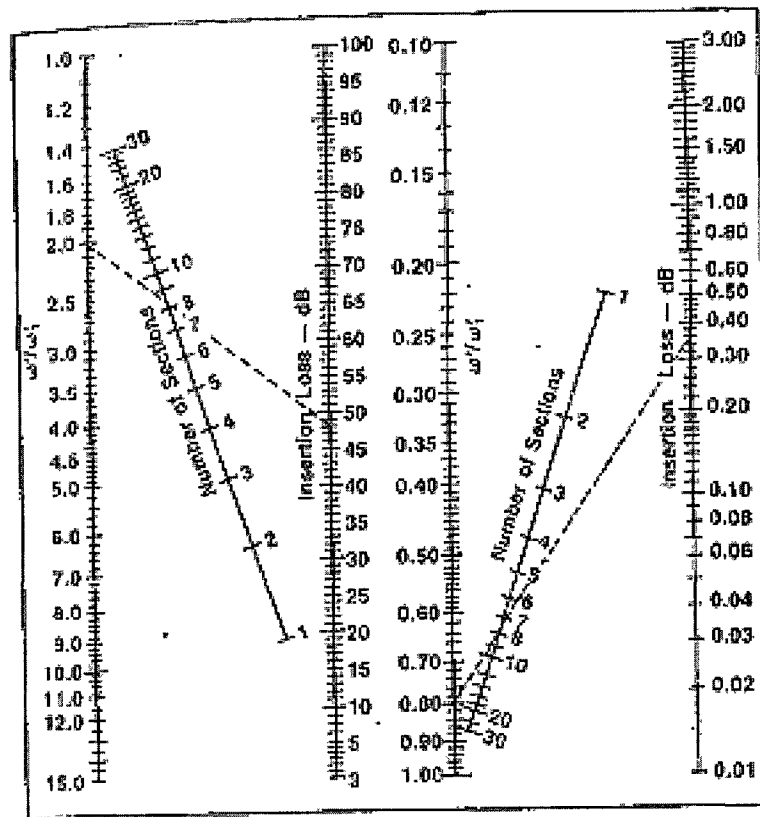
Fig.67. Nomograph for selecting number of sections of Butterworth filter for given insertion loss in the stopband. This chart is separated into stopband (left-hand side) and passband regions (right-hand side). From T Milligan, *"Nomographs Aid the Filter Designer"* Microwave and RF, Vol. 24, October 1985 [6]
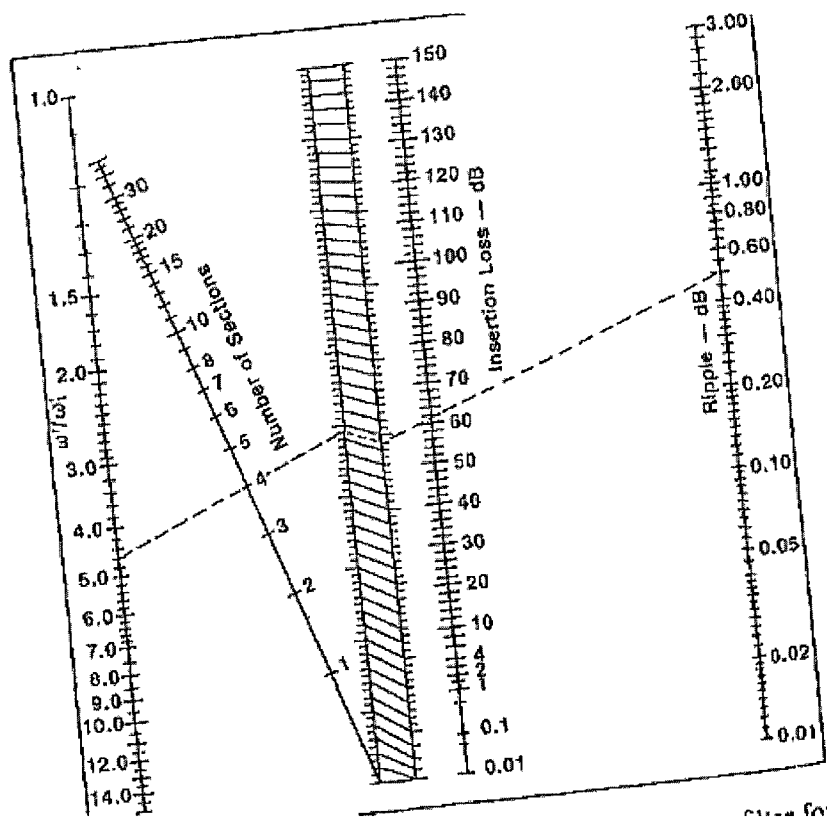
Fig.68. Nomograph for selecting number of sections of Chebyshev filter for given insertion loss in the stopband. This chart is separated into stopband (left-hand side) and passband regions (right-hand side). From T Milligan, "*Nomographs Aid the Filter Designer*" Microwave and RF, Vol. 24, October 1985. [6]

References

[1]: ETSI EN 302 217-1 v1.3.1 (2009-09) Fixed Radio System; Characteristics and requirements for point-to-point equipments and antennas; Part 1: Overview and system-independent common characteristics.

[2]: FCC CER47 part 15: Radio Frequency Devices. Federal Communications Commision

[3]: ECC/REC(09)01: Use of the 57 – 64 GHz Frequency Band for Point-to-point Fixed wireless systems.

[4]: CEPT/ERC/REC 74-01: Unwanted Emissions in the Spurious Domain

[5]: John S. Seybold *"Output back-off requirements for root-raised cosine filtered digital"*online document available: *http://rfdesign.com/mag/radio_output_backoff_requirements/*

[6]: Kai Chang *"Handbook of Microwave and Optical Components"* Volume 1, Wiley Interscience Publication, John Wiley & Sons, INC.

[7]: Ralph Levy, *"Filters with Single Transmission Zeros at Real or Imaginary Frequencies"* IEEE Transactions on Microwave Theory and Techniques, Apr. 1976. Volume: 24 Issue: 4. pp. 172-181

[8]: Jesse G Baldwin and Dale F. Dubber. *"Quadrature Mixer LO leakage Suppression Through Quadrature DC Bias"* Sandia National Laboratories

[9]: T.S.Saad, *"Ed Microwave Engineer's handbook"*, Artech House, Dedham, MA, 1971

[10]: RT/duroid 5870/5880 series datasheet, Rogers corp. online document available: *http://www.rogerscorp.com/acm/products/10/RT-duroid-5870-5880-5880LZ-High-Frequency-Laminates.aspx*

[11]: Woode,R.A. Ivanoc,E.N. Tobar,M.E. Blair,D.G *"Measurement of dielectric loss tangent of alumina at microwave frequencies at room temperature."* Electronics letters. Issue date: 8 Dec 1994. Volume: 30. Issue: 25, pp. 2120-2122.

[12]: Jia-Sheng Hong, Michael J. Lancaster *"Couplings of Microstrip Square Open-loop Resonators for Cross-coupled Planar Microwave Filters"* IEEE Transactions on Microwave Theory and Techniques. Nov. 1996. Volume: 44. Issue: 11. pp. 2099-2109.

[13]: Christen Rauscher, *"Two-Branch Microwave Channelized Active Bandpass Filter"* IEEE Transactions on Microwave Theory and Techniques. Mar. 2000. Volume: 48. Issue: 3, pp. 437-444.

[14]: Advance Design System 2009 documentation on MBEND3

[15]: Ramanan Bairavasubramanian, Stephane Pinel, Joy Laskar and John Papapolymerou

"Compact 60-GHz Bandpass Filters and Fuplexers on Liquid Crystal Polymer Technology" IEEE Microwave and Wireless Components. July 2009. Volume: 19. Issue: 7, pp. 455-458.

[16]: United Monolithic Semiconductor PO9828 datasheet [online] available :
http://ns21647.ovh.net/~csums/telechargement/10-5-1.pdf

[17]: Hittite Microwave medium power amplifier driver: ABH209 datasheet [online] available:
http://www.hittite.com/content/documents/data_sheet/hmc-abh209.pdf

[18]: Hittite Microwave medium power amplifier: ABH241 datasheet, [online] available:
http://www.hittite.com/content/documents/data_sheet/hmc-abh241.pdf

[19]: United Monolithic Semiconductor, LNA CHA2159 datasheet, [online] available:
http://ns21647.ovh.net/~csums/telechargement/9-26-1.pdf

[20]: F.Xu Y.L.Zhang, W.Hong,K.Wu and T.J.Cui,*"Dinite-difference frequency-domain algorithm for modeling guided-wave properties of substrate integrated waveguide,"* IEEE Trans. Microwave Theory and Techniques, vol.51, no.11, pp. 2221-2227, Nov. 2003

[21]: H.Li, W.Hong,T.J.Cui, and K.Wu,*"Propagation characteristics of substrate integrated waveguide based on LTCC,"*IEEE MTT-S Tech Dig., vol.3, Jun.2003, pp. 2045-2048

[22]:P.Ferrand, D.Baillargeat, S.Ve, J.Puecerdeymh, M.Lahti and T.Jaakola
"LTCC reduced-size bandpass filters based on capacitively loaded cavities for Q band application" IEEE MTT-S International Microwave Symposium Digest. 12-17 Jun. 2005, p. 4.

[22]: Jong-Hoon Lee, Stephane Pinel, John Papapolymerou, Joy Laskar and Manos M. Tentzeris. *"Low-loss LTCC Cavity Filters Using System-on-Package Technology at 60 GHz"*, IEEE Trans. Microwave Theory and Techniques. Vol.53, NO.12 Dec 2005, pp. 3817-3824.

[23]: J.S.Hong and M.J. Lancaster, *"Microstrip Filters for RF/Microwave Applications"*. New York: Wiley 2001,

[24]: Ian A. Glover and Peter M. Grant *"Digital Communications 2nd Edition"* Pearson Education Limited

[25]: ITU-R Handbook of Radiometeorology, 1996

[26]: John W.M. Rogers and Calvin Plett *"Radio Frequency Integrated Circuit Design"* Artech House 2003

[27]: RadioWave Inc catalog 2003, available online: www.radiowaveinc.com

[28]: Kai Chang and Lung-Hwa Hsieh*"Microwave Ring Circuits and Related Structure"* Wiley-Interscience, A John Wiley & Sons, Inc., Publication

[29]: UltraSource, custom thin film circuits and interconnects. www.sultrasource.com

[30]: G.Matthaei, L. Young and E.M.T Jones '*Microwave Filters, Impedance-Matching Networks and Coupling Structures*' Artech House

[31]: Ferro Electronic Materials, '*LTCC A6 system for wireless solutions, Materials, specifications and guidelines*'

[32]: VTT Electronics '*Design Guildlines Low Temperature Co-Fired Ceramic Modules*'

[33]: Flann Microwave "*Waveguide and Flange Data*" available at: www.flann.com

[34]: Ansoft HFSS 3D full-wave electromagnetic field simulator. Software details available at: http://www.ansoft.com/products/hf/hfss/

[35]: Hideo Iizuka, Toshiaki Watanabe, Kazuo Sato and Kunitoshi Nishikawa "*Millimeter-Wave Microstrip Line to Waveguide Transition Fabricated on a Single Layer Dielectric Substrate*" Research report on special Issue Millimeter-Wave Radar for Automotive Applications, p. 13.